DEVELOPMENT OF CONTROL SETUP FOR A MATERIAL TESTING MACHINE AND EXPERIMENTAL ANALYSIS OF THE EFFECT OF VOID VOLUME FRACTION ON THE STRENGTH OF RECYCLED HIGH-DENSITY POLYETHYLENE MATERIAL

A Thesis

by

OSMAN ERENER

Submitted to the Graduate and Professional School of
Texas A&M University
in partial fulfillment of the requirements for the degree of

MASTER OF SCIENCE

Chair of Committee,	David H. Allen
Committee Members,	Jens Figlus
	Theofanis Strouboulis
Head of Department,	Sharath Girimaji

December 2021

Major Subject: Ocean Engineering

ABSTRACT

This study is part of a larger research effort to investigate the mechanical response of composite beams to cyclic loading caused by waves striking beams imbedded in a low-cost sea wall. In the course of the research, it has been determined that material characterization of the beams is needed, and toward this end an MTS (Materials Test Systems) testing machine has been purchased by the TAMU Ocean Engineering Department. The testing machine was used for the purpose of testing recycled high-density polyethylene glass fiber composite specimens in order to characterize the stress-strain response and to measure the effect of void volume fraction (V_{VF}) within the high-density polyethylene beams. Samples taken from different areas of the beams with varying V_{VF} were tested and the effect of these voids was investigated for the purpose of determining the efficacy of deploying these structural components within low-cost sea walls. The study includes developing testing protocols, calibrating, and proof testing the machine in order to perform the experiments. Since the lab's testing machine does not have a controller, a control setup is developed herein to control the MTS Testing Machine with signal processing via a National Instrument USB-6346 Data Acquisition Device and LabVIEW software.

Results display the decrease in the stiffness as the V_{VF} increases as well as decreases in the ultimate stress and ultimate strain. Increasing strain rates displayed higher stiffness, ultimate stress (σ_{ult}), and ultimate strain (ϵ_{ult}) values. The results are discussed and invalid tests are described in detail wherein large voids locally misrepresent the general behavior and are incongruent with the valid tests.

DEDICATION

This thesis is dedicated to my family, Serdar, Gulseren, Yasin Emre Erener and Esra Erener Baglama. Without their love, patience, guidance, encouragement, and constant support my graduate study would not be possible.

ACKNOWLEDGEMENTS

I would like to express my sincere appreciation to my committee chair and advisor Dr. David Allen for his unlimited knowledge and patience. It has always made me feel lucky to know that he supports me. I am grateful to him for every new thing I have learned through him.

I would like to thank to my committee members, Dr. Jens Figlus and Dr. Theofanis Strouboulis for their guidance and support throughout the course of this research.

I would like to thank to Prof. Laurrie Cordes for her huge support and sympathy. I have no doubt that she is the kindest person in the Texas A&M University.

I would like to thank to my family for providing endless love and support. I believe that feeling this love and support is the most precious thing in the world for a person.

Thanks to my first and best friend Ugur Erener. We have shared great memories and believe will have great future together.

Thanks to my dear friend Ali Can Bekar. He has not been only a good friend of mine, but also my confidant and even my mentor.

Thanks also go to my friends and colleagues and the department faculty and staff for making my time at Texas A&M University a great experience. I will always remember Ben McKeig's support and friendship. I am sure he will have a great future and he deserves everything.

And lastly, I would like to thank Dr. Roger Cordes. I can't explain how much support, encouragement and time he has freely given to me. I know his wisdom will shape my personality and future life. I feel truly blessed to have had him as a mentor and friend, and any student should be so lucky to have a teacher like him.

CONTRIBUTORS AND FUNDING SOURCES

Contributors

This work was supervised by a thesis committee consisting of Dr. David Allen and Dr. Jens Figlus of the Department of Ocean Engineering and Dr. Theofanis Strouboulis of the Department of Aerospace Engineering.

Funding Sources

This work was supported by Texas A&M University Department of Ocean Engineering.

NOMENCLATURE

DAQ	Data acquisition device
HDPE	High-density polyethylene
NHDES	New Hampshire Department of Environmental Sciences
PET	Polyethylene Terephthalate
VI	Virtual instruments are the common name for applications created in LabVIEW

Abbreviations

$A_{Gage\ length}$	Area of extensometer gauge
E	Elastic or Young's modulus
$F_{load\ cell}$	Force on load cell
m	Mass
m_{ideal}	Idealized mass, expected mass without voids
$m_{missing}$	Missing mass, the loss of mass due to the presence of voids
V_{VF}	Void Volume Fraction
V_{void}	Void Volume
V_{total}	Total Volume of the sample
$V_{missing}$	The missing volume, the equivalent void volume of the entire sample
ϵ_{ult}	Ultimate strain
$\dot{\epsilon}$	Strain rate
ρ_{hdpe}	Density of HDPE glass fiber material
ρ_{sample}	Densities of each sample
σ_{ult}	Ultimate strength
σ_y	Yield strength

TABLE OF CONTENTS

Page

LIST OF FIGURES

Page

LIST OF TABLES

Page

1. INTRODUCTION

1.1. High-Density Polyethylene (HDPE) Use and Manufacturing

In recent decades, the use of plastics has rapidly increased. With the increase in plastic production, the resulting waste has become a problem for the world. In 2018, annual plastic production of the world reached 359 million tons (Limami et al., 2020). Plastics are one of the fastest growing segments of municipal solid waste (EPA, n.d.). Notably, packaging and container wastes accounted for the largest portion of plastic tonnage at over 14.5 million tons in 2018. Most of these products are produced from polyethylene terephthalate (PET) and high-density polyethylene (HDPE).

HDPE is widely used in home applications due to its good mechanical properties and low cost (Enderle, 2001). Considering the usage rate of the material in the market, it can be expected that most of the household waste is HDPE. According to Limami et al. (2020), 13% of plastic waste in the world was HDPE in 2017.

Thermoplastics are a type of polymer that can be softened and melted by heat and can be produced in either a heat-softened or a liquid state. Heat is used to process thermoplastic polymers over and over again, and they can be recycled directly into new products (Mallick, 2021). The advantages of thermoplastic composites, include relatively light weight, high fatigue strength, corrosion resistance, and electrical insulation (Campbell et al., 2006). Thermoplastics have been around for a long time and are a vital part of modern life and are critical in a number of industries. To increase modulus and/or strength, increase heat deflection temperature, limit thermal expansion, and reduce mold shrinkage, they are frequently combined with either mineral fillers or short fibers. They may also contain a number of additives, such as heat stabilizers, antioxidants,

fire retardants, plasticizers, impact modifiers, and colorants, which are used to improve processing, change physical or thermal properties, and improve one or more mechanical properties (Mallick, 2021).

HDPE is also a thermoplastic with a low tensile modulus, low density, and suitable for a number of applications as a composite due to its lighter weight. The production of HDPE is relatively easy and well researched and developed compared with other composite matrices. Furthermore, because HDPE can be made from recycled plastic, it has a long shelf life and has a low environmental impact (Sadik et al., 2021). Injection molding, blow molding, and thermoforming are three popular production procedures for thermoplastic products. For the great majority of thermoplastic products, injection molding is the primary processing method. Because of its high production rates, economic effectiveness, and capacity to make complicated objects with great precision, injection molding plays a major role for both intricate parts and, as will be shown in the current study, for large cross sections (Yang et al., 2016).

In a standard injection molding machine, a spinning screw in a heated barrel melts and homogenizes short fiber reinforced thermoplastic. The melt is then injected at high pressure into a set of matched tooling, where the material cools. The fiber alignment is partly determined by the material's flow direction; for short fibers in a relatively large mold, it is typical for the flow to be irregular and turbulent prior to cooling and thus the fibers have a random alignment (Middleton, 2016). An injection molding machine can be seen in Figure 1.

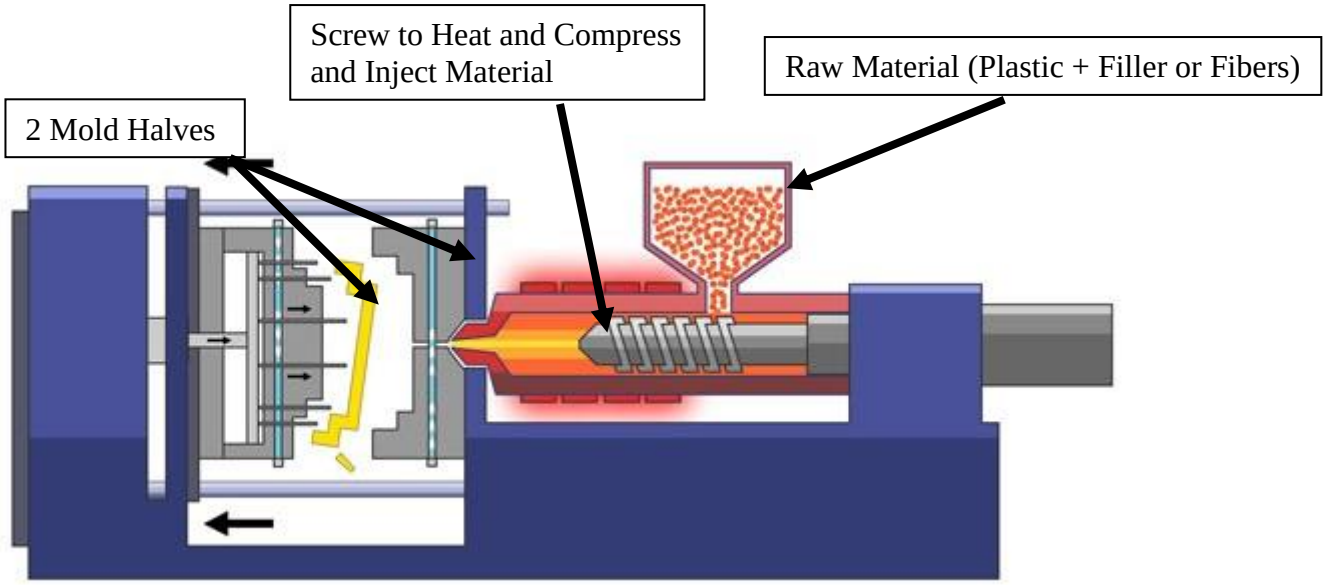

Figure 1. Injection Molding Machine Schematic Showing Open Mold After Part (Yellow) has Formed

1.2. The Formation of Voids and their Effect

In molding, voids can occur in thick materials. The molten plastic fills the mold cavity under pressure from the screw and quickly starts to cool because the mold is chilled to accelerate setting and increase production rates. When the product is thick, the outside surface of the part cools faster than the inner core. As a result, as the melt in the inner section cools, it contracts away from the surface while shrinking, potentially resulting in insufficient pressure to keep the parts' center from creating voids as continued cooling and contraction occur.

Because of their impact on mechanical characteristics, voids are generally undesirable. Studies have examined the mechanical effect of voids in composite materials, solder connections, concrete, and other materials. Werner et al. (2014) reports that with increasing volume fraction, Young's modulus (E) is considerably decreased for carbon-bonded alumina material. Zhang et al. (2014) shows that Young's modulus (E) of carbide (Cr_3C_2) decreases significantly when porosity increases. Olivier et al. (1995) indicated that increasing the void volume fraction from 0% to 10%

caused the tensile strength of unidirectional carbon/epoxy composite to decrease by 30%. With an increase in void content from 0% to 10%, he also noted a moderate decrease in longitudinal tensile strength, which is 10%. According to Broucke et al. (2007), a 1% increase in void volume fraction results in a 5% decrease in in-plane tensile modulus and a 7% decrease in out-of-plane tensile modulus in a carbon/epoxy woven composite.

1.3. HDPE Composite Crossties

The material to be studied herein is a thermoplastic composite material made from recycled HDPE with glass fibers embedded (hereafter, HDPE composite). The final form is a crosstie, with a cross section of approximately 7x9 inches and a length of approximately 8.5 feet. Figure 2 shows a photo of a column produced from melted recycled HDPE. The melted/recycled HDPE and glass fiber are injected into a mold containing a blowing agent and form a structure where the glass fibers are randomly distributed. Figure 3 shows the cross-sectional area of an HDPE composite crosstie. The void volume fraction tends to increase from the outside to the center. While the core of the crosstie contains many small voids, large voids are randomly located between the inner and outside sections.

Figure 2. Recycled HDPE Composite Crosstie

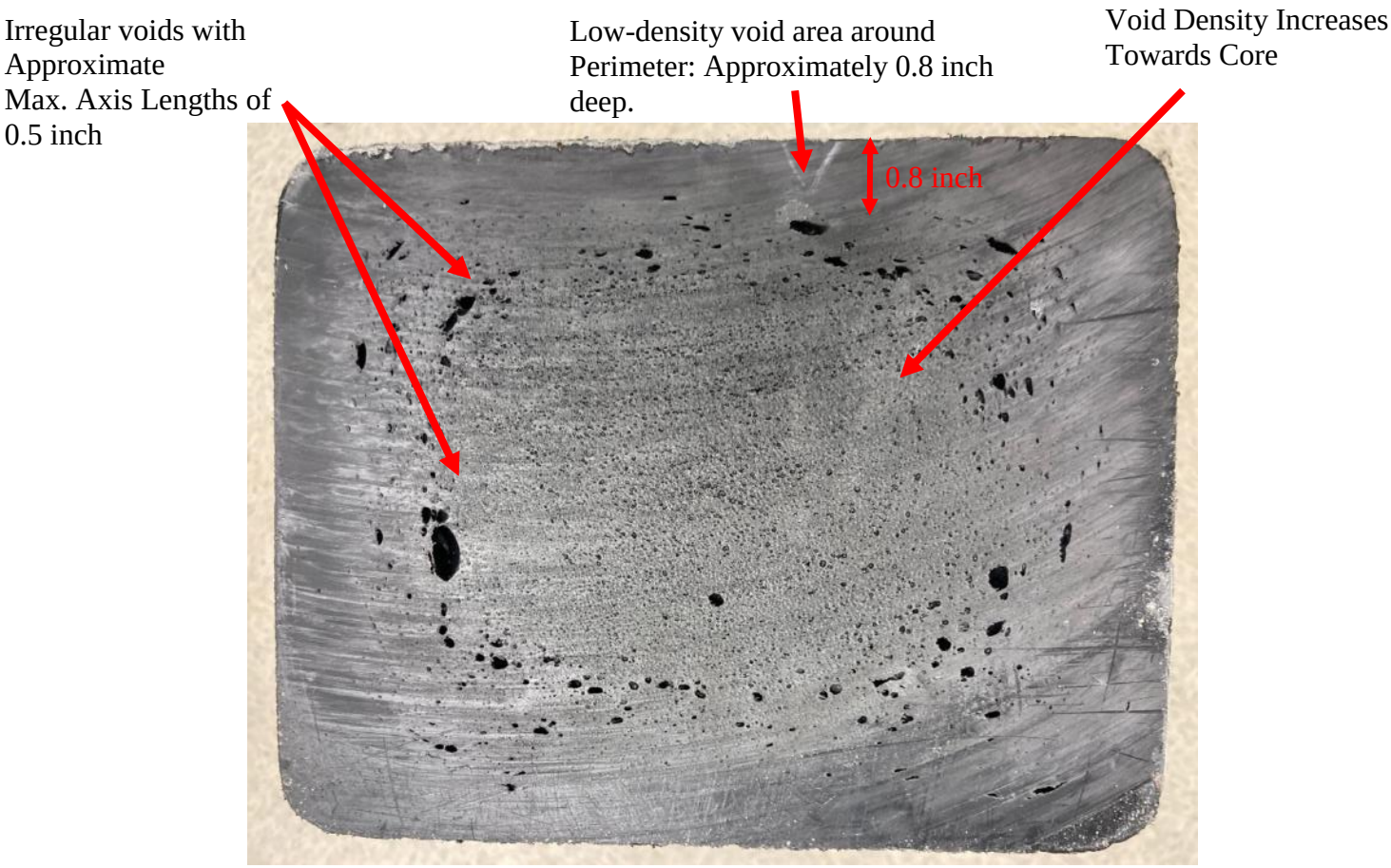

Figure 3. Section View of Recycled HDPE Composite Crosstie

1.4. Testing Machine Configuration and Calibration

Since the lab's testing machine does not have a controller, a control setup is developed herein to control the MTS Testing Machine with signal processing via a National Instrument USB-6346 Data Acquisition device (DAQ) and LabVIEW software which is also purchased by the TAMU Ocean Engineering Department.

1.5. Research Goals

The current research is focused on the development of a control setup for the MTS testing machine. Utilizing this successful system enabled the research on characterizing the HDPE

composite beam's material properties. It also enabled an experimental analysis of the effect of void volume fraction on the strength of the HDPE composite. Also, the effect of the strain rate ($\dot{\epsilon}$) on material properties was investigated. Strain rate is the change in strain of a material with respect to time.

$$\dot{\epsilon} = \frac{d\epsilon}{dt} \qquad (1)$$

Lower strain rates are associated with longer periods, while higher strain rates are associated with shorter times and relatively more rapid loading. Typically, in HDPE and similar plastics, the yield strength and modulus increase as the strain rate increases (Sepe, 2011).

2. POSSIBLE OCEAN ENGINEERING APPLICATIONS FOR HDPE COMPOSITE

Composite structures enable engineers to obtain customizable material properties specifically suited for their application or project. For example, historically composites have been made with a focus on saving weight while retaining strength and crashworthiness and crash energy management. A wide variety of industries have used composites, with deep inroads in the automotive and aerospace industries (Mamalis et al., 1997). The major benefits of fiber reinforced composite materials over more traditional materials are the extremely high specific strengths and stiffnesses that may be produced. In addition, using composites, the designer may change the kind of fiber, matrix, and fiber orientation to create composites with tailored material characteristics that may not be found in traditional materials. Aside from the obvious benefits of decreased weight, design flexibility, and low manufacturing costs, composite materials hold a lot of promise for lightweight, relatively strong structures with good corrosion resistance.

In coastal and marine engineering, structural designs are used for a variety of functions including breakwater reinforcement and piers. HDPE composite can be used for these ocean structures, with the advantages of relatively low weight, high design flexibility, low production costs, high energy absorption and long life due to corrosion resistance.

2.1. Piers

Wood is the most common material used in piers (Figure 4). It may not be the best choice for all piers, given the lifetime cost including manufacture, maintenance, durability, and energy management. Pressure-treated woods have been used in ocean structures to resist corrosion and extend the life, however, regular inspections and repairs are still required. Further, environmental

concerns exist because of the chemical preservatives used in pressure treatment that are needed for the lumber to become resistant to insects, moisture and decay.

Figure 4. Pier Made of Timber

The New Hampshire Department of Environmental Sciences (2019) reports that creosote has been prohibited for a long time because it has been determined that high quantities of this wood preservative can cause birth abnormalities, tumors, and cancer. In addition, woodworking solutions can cause harmful effects to fishes, as inorganic arsenic and pentachlorophenol can accumulate in the tissues of animals.

HDPE composite's potential use in piers avoids many of these negatives in that HDPE composites are not harmful to nature, can be recycled, and have relatively good material properties (esp. strength and fatigue performance).

2.2. Sea Walls

Traditional materials such as concrete, steel and wood have been frequently used in seawalls. In particular, most of the sea walls built in the past are made of stone, concrete and concrete panels (Figure 5). Although they are known for their longevity, their maintenance, repair and replacement costs are very high. Generally, for concrete sea walls reinforced with low-alloy steel rebar, surface rust, corrosion and fracturing are the concerning problems. When this happens, the wall's strength decreases rapidly especially in harsh saltwater environments.

Studies reporting the success of plastics as a structural component in sea walls are not common, however, Ashpiz et al. (2010) studied fiberglass plastic materials in sea walls. He found they are not affected by decay and corrosion. He indicates that because of the panels' ability to absorb energy and resist low-stress cyclic fatigue, fiber glass panels increase the sea wall's overall life. Also, when designed and implemented appropriately, the construction time needed can be reduced approximately five times compared with traditional methods.

Figure 5. Concrete Sea Wall

HDPE crossties can be applied in sea walls as seen in Figure 6 because of their high energy absorption, low maintenance costs, and long life due to corrosion and decay resistance. Because of the physical properties of HDPE composites, weights of sea walls will be reduced and, consequently, their delivery and installation could be cheaper and easier.

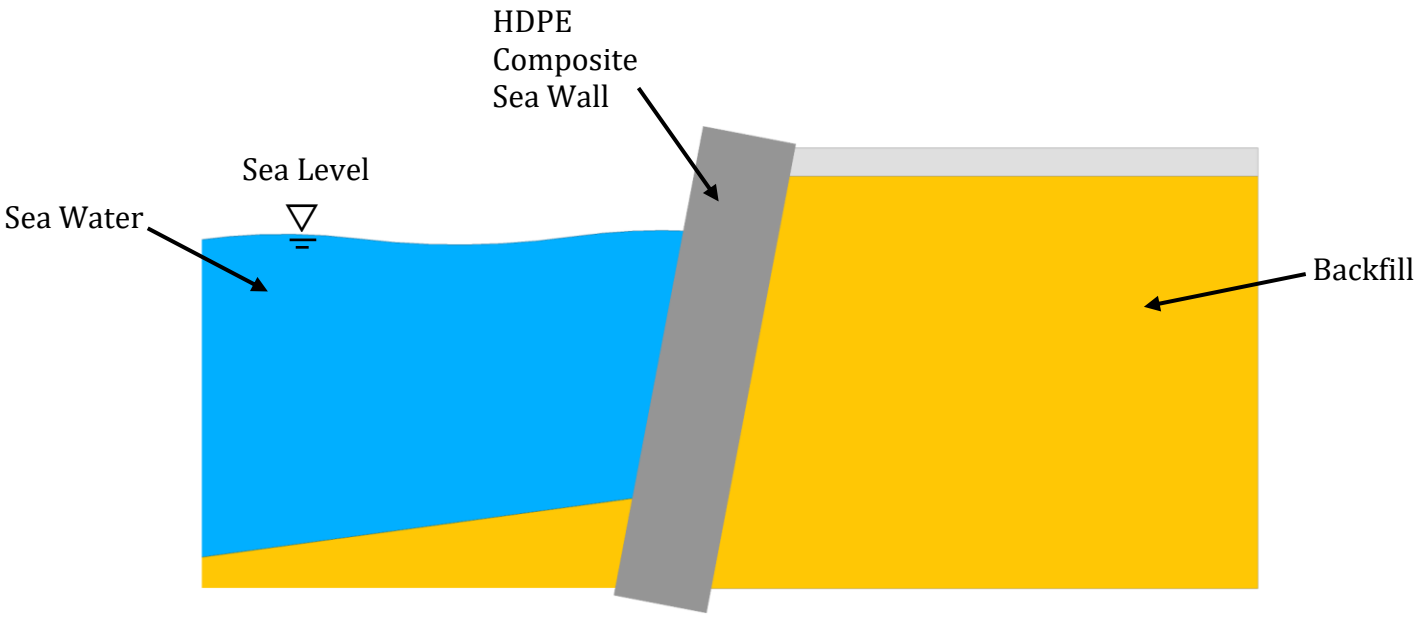

Figure 6. Seawall Application of HDPE Composite

This research helps to obtain local material properties of HDPE crossties (i.e., variations spatially through the cross section) and can be used for the global design of crossties for piers and sea walls. Also, high strain rate tests can represent the viscoelastic material response and thus can assist with understanding the effect of high energy waves on HDPE composites used in ocean structures.

3. DEVELOPMENT OF CONTROL AND MEASUREMENT SETUP FOR A MATERIAL TESTING MACHINE

In order for the strength tests of HDPE composite to be performed on the MTS testing machine, both a control and measurement setup were created.

The control setup enables controlled cross-head movement of the MTS test machine. The cross-head, which can move up and down via servo-valve and actuator, enables tension and compression tests to be performed (Figure 7). With the new control setup, the signal sent to the valve can be adjusted and the user can decide at what speed and in which direction the cross-head can move.

After the analog signals obtained from the extensometer and load cell are amplified by the signal conditioner, they are converted into digital signals with the help of a data acquisition device (DAQ) and read with LabVIEW software.

Making the electronic connections for both control and measurement setups is one of the most important parts of this research. Making all connections correctly and successfully requires attention and experience. The quality of the connection made through the connectors directly affects the quality of the signal from the measuring devices. It is also important to use correct diagrams and grounding to avoid noise and to obtain an optimal signal.

A setup consisting of a DAQ, a signal conditioner, a LabVIEW software, a load cell, an extensometer, and a computer has been created to control the MTS Test Machine and to obtain measurements of the tests performed. (Figure 8).

3.1 Testing Machine

Uniaxial testing machines are generally used for static, dynamic and fatigue tests to characterize material properties. The basic principle of material testing is to apply mechanical

loading to determine mechanical properties of samples such as the stiffness or modulus (E), and yield strength (σ_y) and ultimate strength (σ_{ult}) and ultimate strain (ϵ_{ult}). With the movement of the crosshead, the compressive or tensile load is applied to the sample placed between the grips as seen in Figure 7. The strain and load values were measured with an extensometer and load cell, respectively.

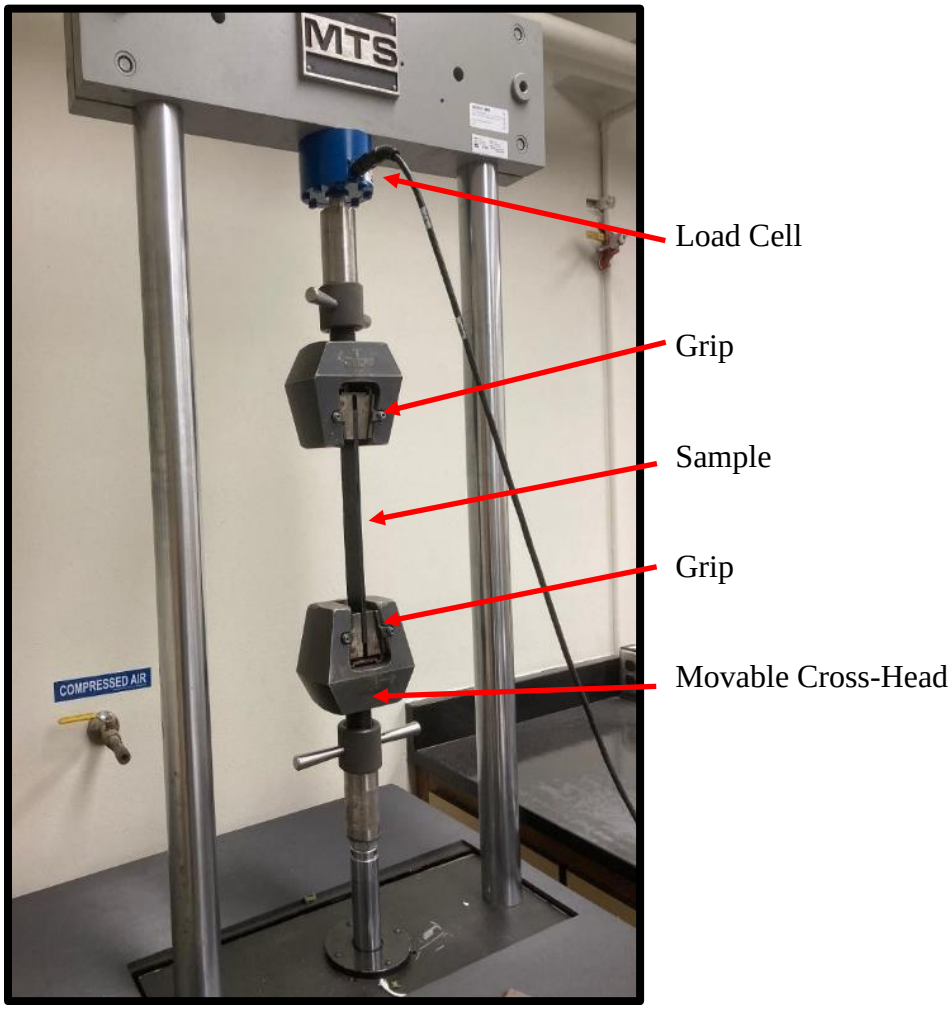

Figure 7. Testing Machine in Ocean Engineering Lab

Material testing can provide important information about the materials incorporated into products to ensure they perform within desired specifications (Adamczak et al., 2012).

Additionally, for a nonhomogeneous beam, the advantage of structural testing is to reveal any deficiencies in the final design of the product planned to be produced. Thus, problems that may arise during the deployment of the material can be predicted and measures can be taken to prevent unnecessary malfunctions. These tests are also crucial to ensuring that the product is manufactured adequately for the intended application, exposed to minimal damage, and designed with optimum performance in mind.

The testing machine crosshead movement is driven by hydraulic pressure. The control of the hydraulic pressure and the data acquisition (the extensometer reading strain and the load cell reading load) are accomplished by employing software on a laptop computer. This software, called LabVIEW, is widely used and provides for relatively easy set-up for various experiments (tensile tests to failure, calibration tests, fatigue, etc.).

The analog signals needed to drive the hydraulic valve that controls the pressure and read the extensometer and load cell data need to be converted from digital signals both output and input to the laptop. The circuit is diagrammed in Figure 8. The cross head is moved by the servo valve and the valve actuator. A computer and a DAQ are required to control the servo valve. As tensile force is applied to the sample for the test, the signals received from the load cell and extensometer are first sent to the signal amplifier and thereafter to the computer via the DAQ.

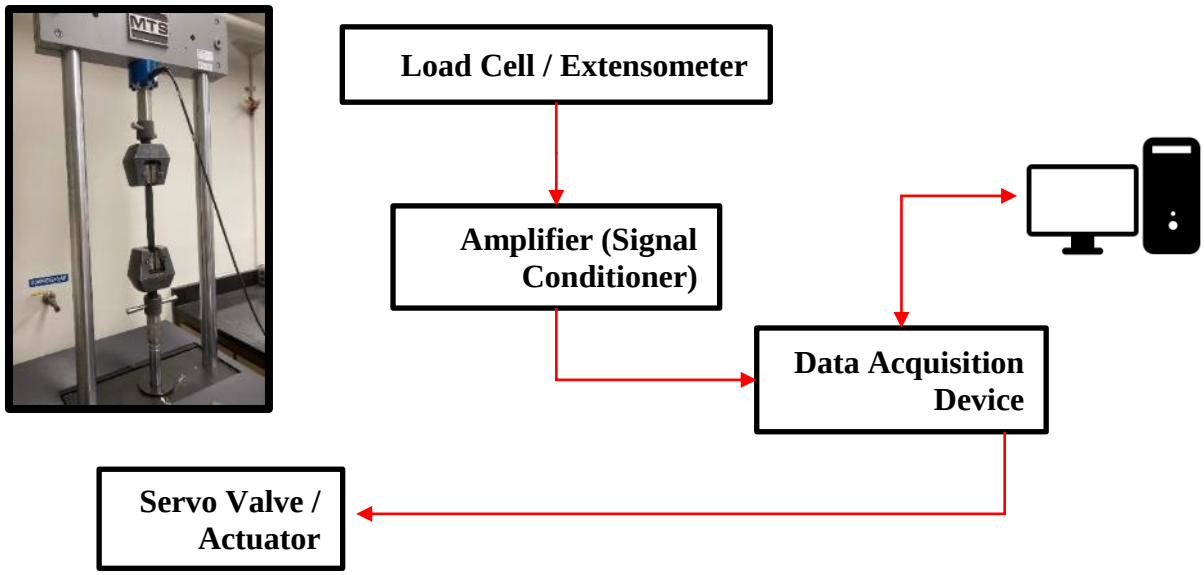

Figure 8. Working Principle for MTS Testing Machine

This new setup was created in the lab as shown in Figure 9.

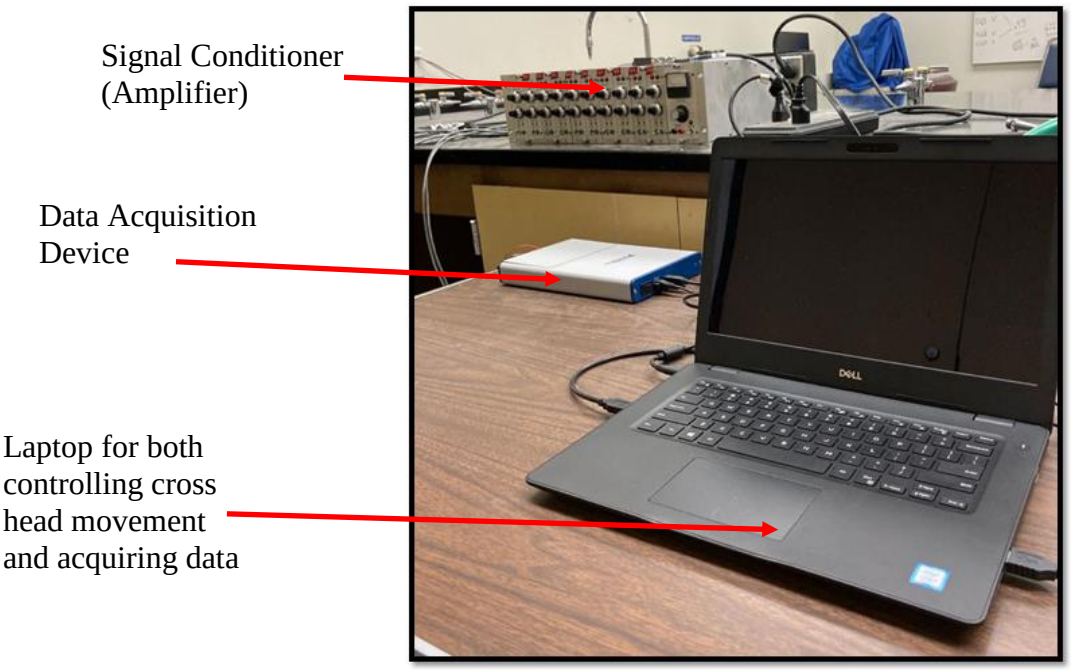

Figure 9. The New Setup in Materials and Structures Engineering Lab

3.2 Control Setup

The testing machine is controlled using the LabVIEW software. This software enables configuration of voltage outputs through a DAQ that controls the test machine's hydraulics. National Instrument equipment was procured as the DAQ and LabVIEW software as computer software.

3.2.1 Data Acquisition Device (DAQ)

The data acquisition process involves receiving the analog input signals (from the load cell and extensometer) and converting those signals into a format that can be read by the LabVIEW software. DAQ systems acquire physical phenomena/inputs in analog format and process or condition the signals, then convert them to digital format for display, transmission, and final use (Bansal, 2021).

To control the MTS Testing Device one of the output channels of the DAQ is connected to the servo hydraulic valve, thereby controlling the hydraulic pressure. In other words, the output channel of the DAQ device (National Instruments USB-6346) is connected to the control connector of the testing machine in order to control the crosshead movement of the test machine through the servo hydraulic valve. Also, two input channels are required to obtain load cell and extensometer data (Figure 10).

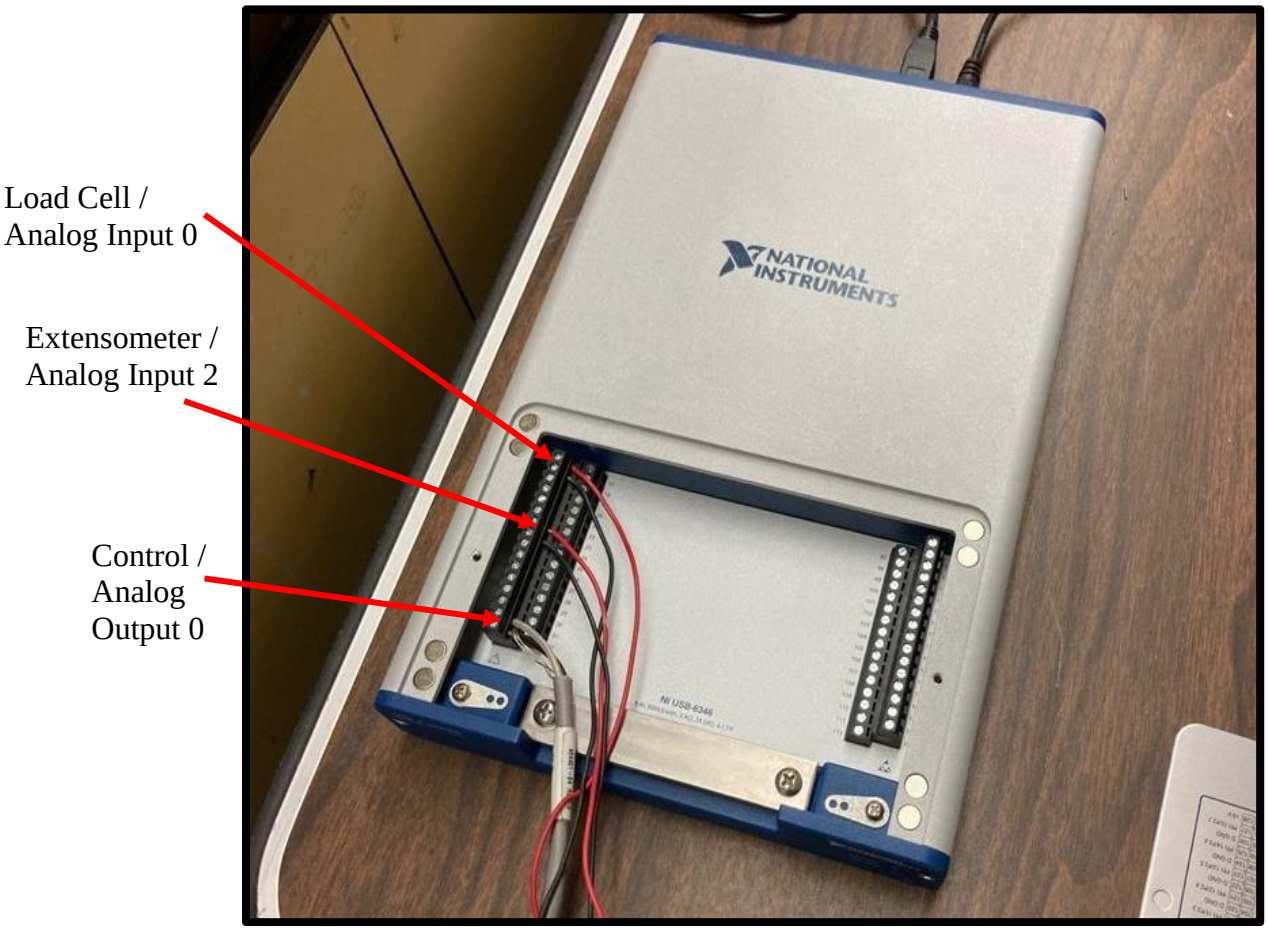

Figure 10. Connections made for the National Instrument USB-6346

3.2.2 LabVIEW

LabVIEW is a widely-used and adaptable graphical programming environment that was created largely for instrumentation control and data acquisition. Virtual instruments (VIs) are the common name for applications created in LabVIEW. The content of VIs is encompassed in a block diagram. Another window called the front panel is used to interface with the VI for input and output. The user-friendly apps are made possible by the graphical icon-based source code and interface, which removes the need to type in long character-based code (Moore, 1995).

LabVIEW software is a graphical programming algorithm that enables viewing every element of the application, allowing the creation of data analysis algorithms and the ability to

create unique user interfaces. Because it is a very comprehensive industrial suite, it enables hardware integration with a wide variety of sensors and controllers and offers well-established developer support (Asenjo et al., 2018). An example of the screen view of an application is shown in Figure 11.

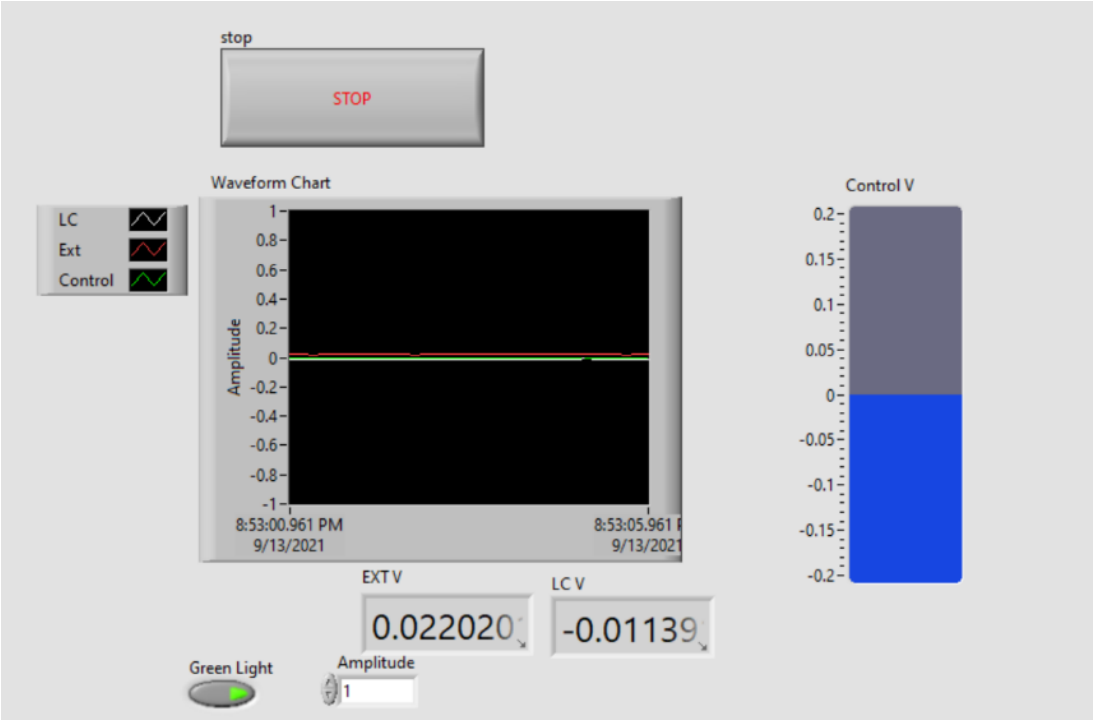

Figure 11. Front Panel of the VI for Controlling the Crosshead

In LabVIEW, three virtual instrumentation (VI) modules were designed, the first of which controls the crosshead movement manually, the second applies a sinusoidal displacement to the crosshead for fatigue testing applications, and the third one adjusts the crosshead displacement based on the measured strain rate. Subsequent control tests were carried out to ensure the correct operation of all three modules. An example of the block diagram logic is shown in Figure 12.

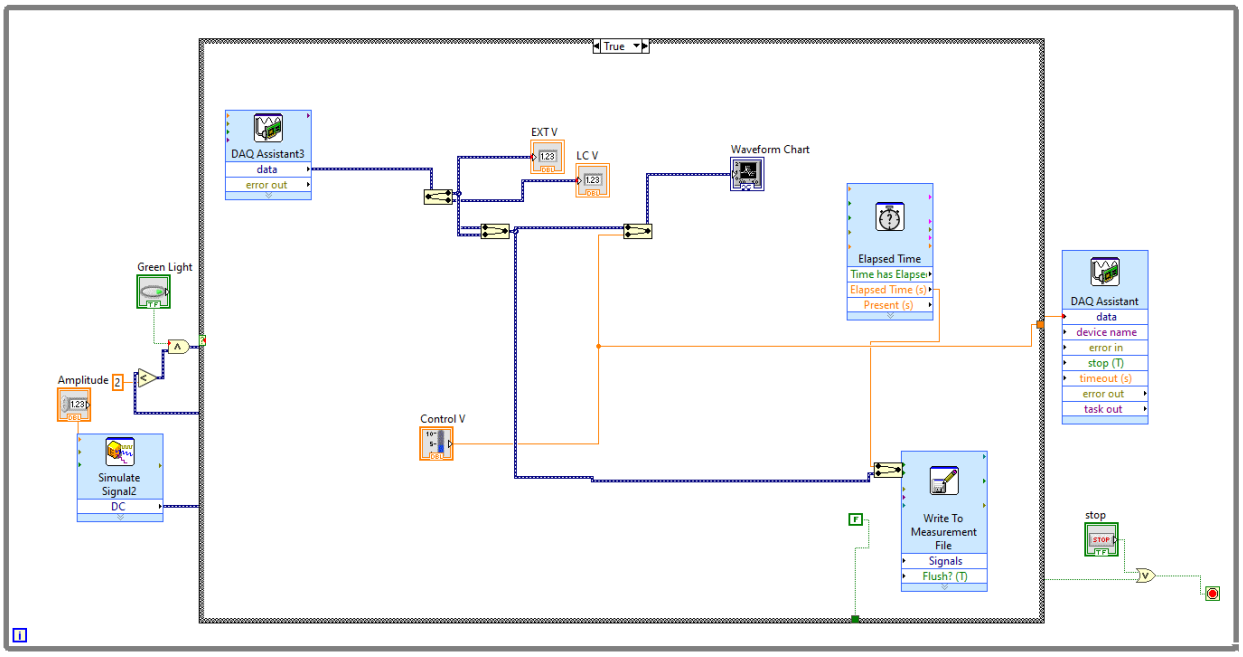

Figure 12. Block Diagram of the VI for Controlling the Crosshead

The first VI controls the crosshead movement manually. With the help of the slide control bar, the control voltage can be adjusted to the testing machine's hydraulic valve, and the up and down movement of the crosshead is enabled. With the help of the indicators on the front panel, some information is obtained during the test. For example, extensometer and load cell voltage are provided. Lastly, output data is written to a file.

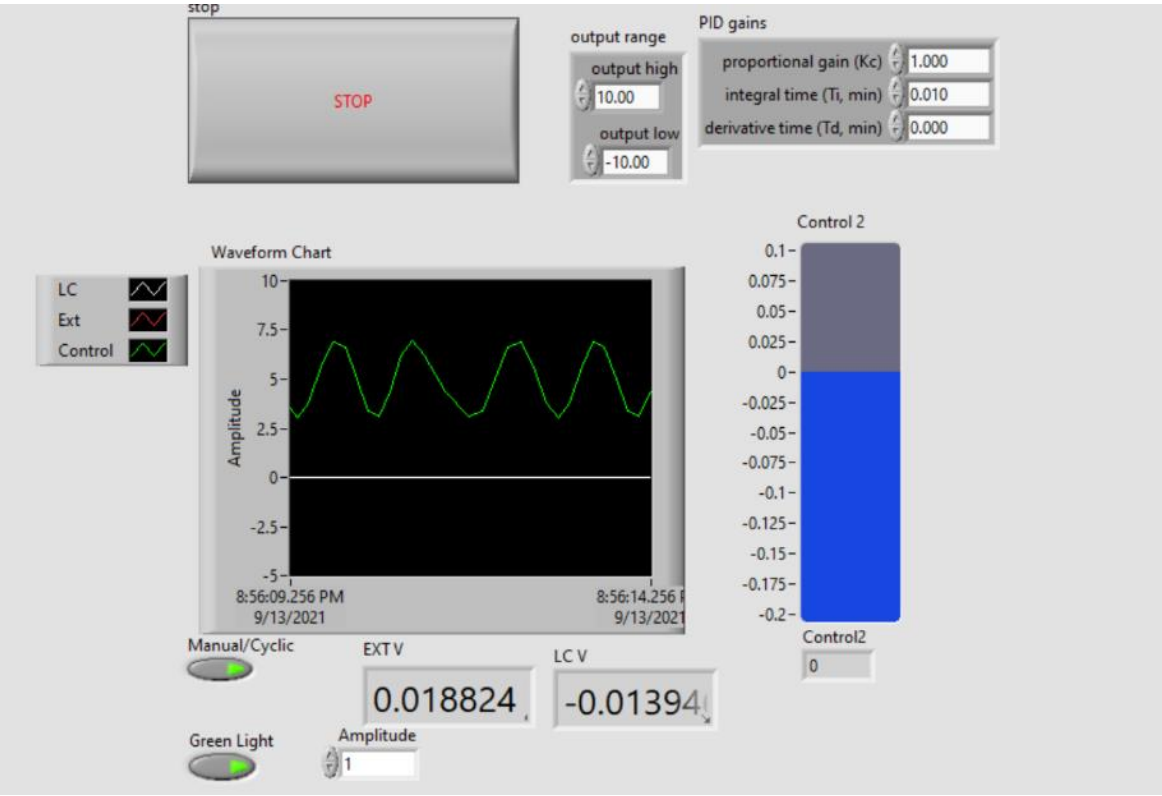

Figure 13. Front Panel of the VI for Fatigue Testing

In the second VI (shown in Figure 13), in addition to providing the crosshead movement manually, it controls sinusoidal movement of the crosshead. Thus, a fatigue test program has been created using this VI. The generation and acquisition of signals are also provided by Data Acquisition Assistant Modules. Utilizing the Cyclic/Manual button, the crosshead movement can be changed between sinusoidal movement and manual control. Again, the output data is recorded to a data file in order to obtain the necessary results. The block diagram of the logic is shown in Figure 14.

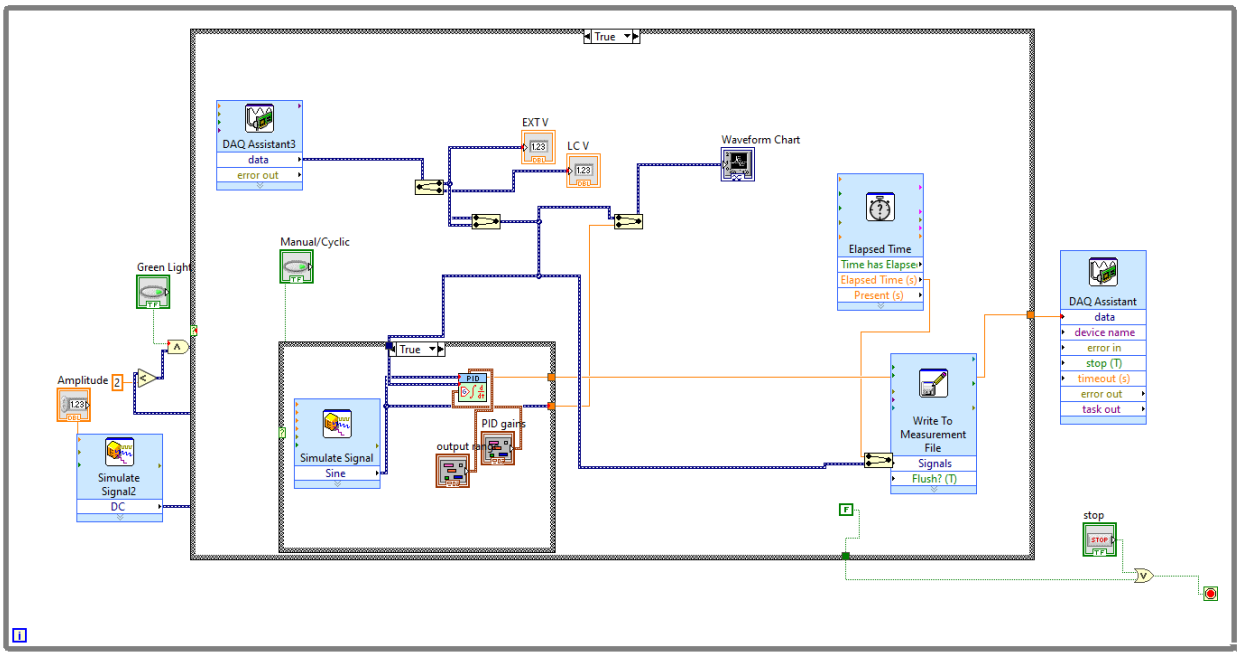

Figure 14. Block Diagram of the VI for Fatigue Testing

The third VI adjusts the crosshead movement automatically rather than manually during a tensile test. This VI is created to enable adjustments to the control voltage for the purpose of controlling the strain rate ($\dot{\epsilon}$). In this closed-loop configuration, the strain rate is calculated during the test by dividing the change in strain from the extensometer by the corresponding change in time. Thus, especially when testing a material with strain-rate dependence like HDPE composite, a constant strain rate can be prescribed. This automatic control system also enables strain rate to be used as a parameter in the tests designed to study void volume fraction's effect on HDPE composite's stress-strain response. Figures showing the user interface and block logic are shown in Figure 15 and Figure 16.

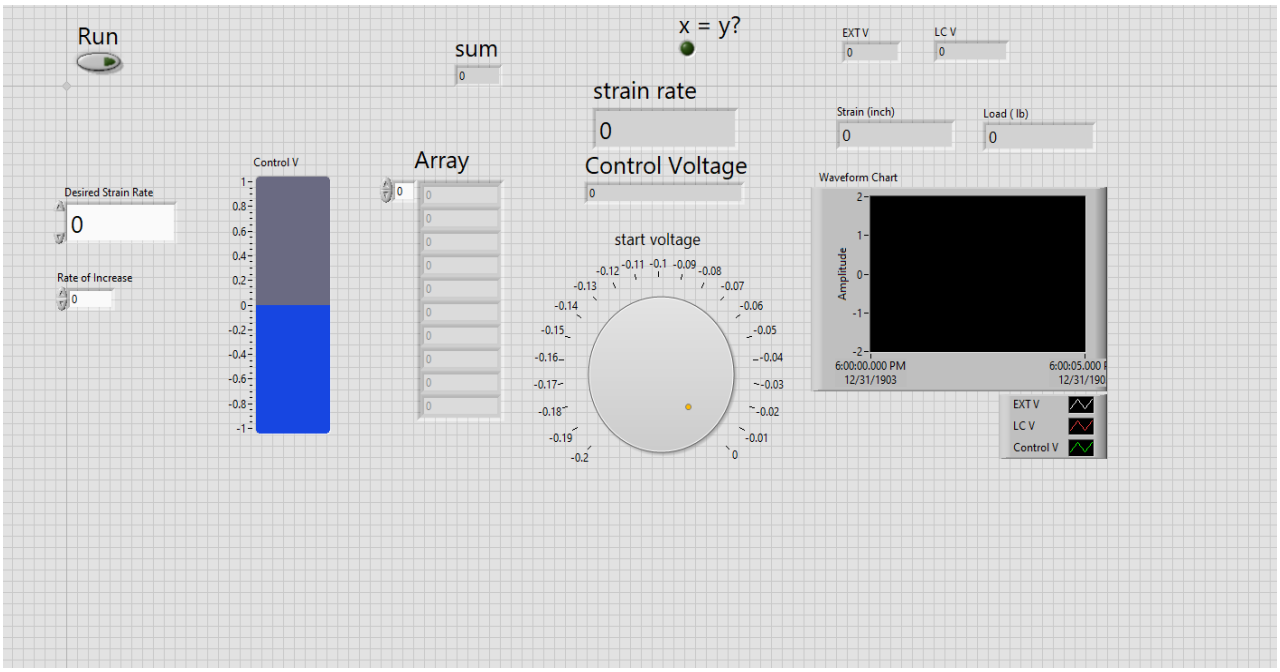

Figure 15. Front Panel of the VI for Strain Rate Controlled Tests

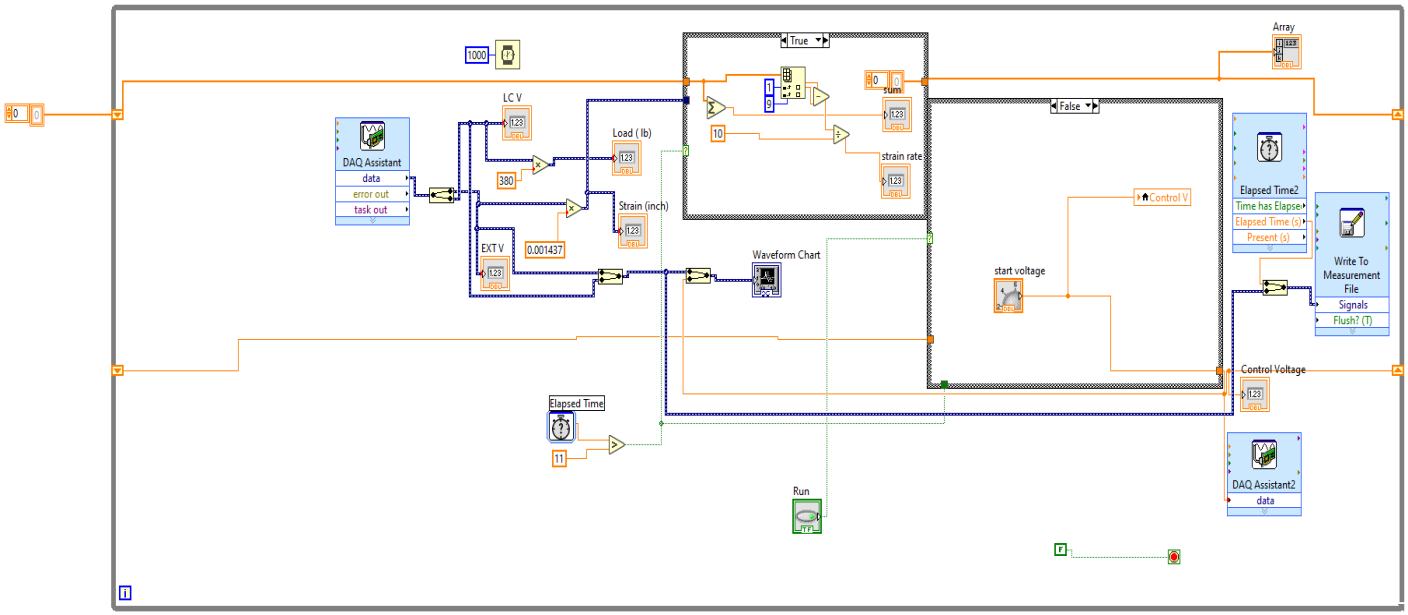

Figure 16. Block Diagram of the VI for Strain Rate Controlled Tests

3.3 Measurement Setup

The control system is focused on data acquisition that can produce graphs of stress vs. strain. To investigate the effect of void volume fraction on the strength of HDPE composite, the test will be a stress-strain test to failure on rectangular (not dog-boned) specimens. The basic elements of this measurement setup are the measurement devices: the load cell and the extensometer. The LabVIEW software is used to acquire the readings from the DAQ after they are amplified by a signal conditioner and scale them to stress and strain values.

3.3.1 Load Cell

A load cell is a mechanical device that is configured with a strain gage to linearly relate changes in load to changes in resistance across the strain gage. In this manner, with the strain gage incorporated into a Wheatstone bridge, an activation voltage can be applied and the output voltage from the bridge can be calibrated to load. The use of the Wheatstone bridge enables small changes in the load cell's strain gage to be amplified and read with more precision via a signal conditioner. The load cell in the test machine is a 5K (25 kN) Interface Fatigue Rated Load Cell (Figure 17).

Figure 17. Interface Load Cell

The load cell is in series with the specimen, which is attached to the grips of the test machine. The electronic signal obtained from the load cell is amplified in the signal conditioner before it is read by the National Instrument's DAQ and fed into the laptop.

3.3.2 Extensometer

An extensometer is a device that measures a specimen's elongation under applied load. Contact extensometers measure deformation of a prescribed gage length by direct contact, such as two knife-edges, on the sample. The MTS 632.11E-20 model extensometer with 25 mm (1 inch) gage length and knife edge was used in the experiments (Figure 18)

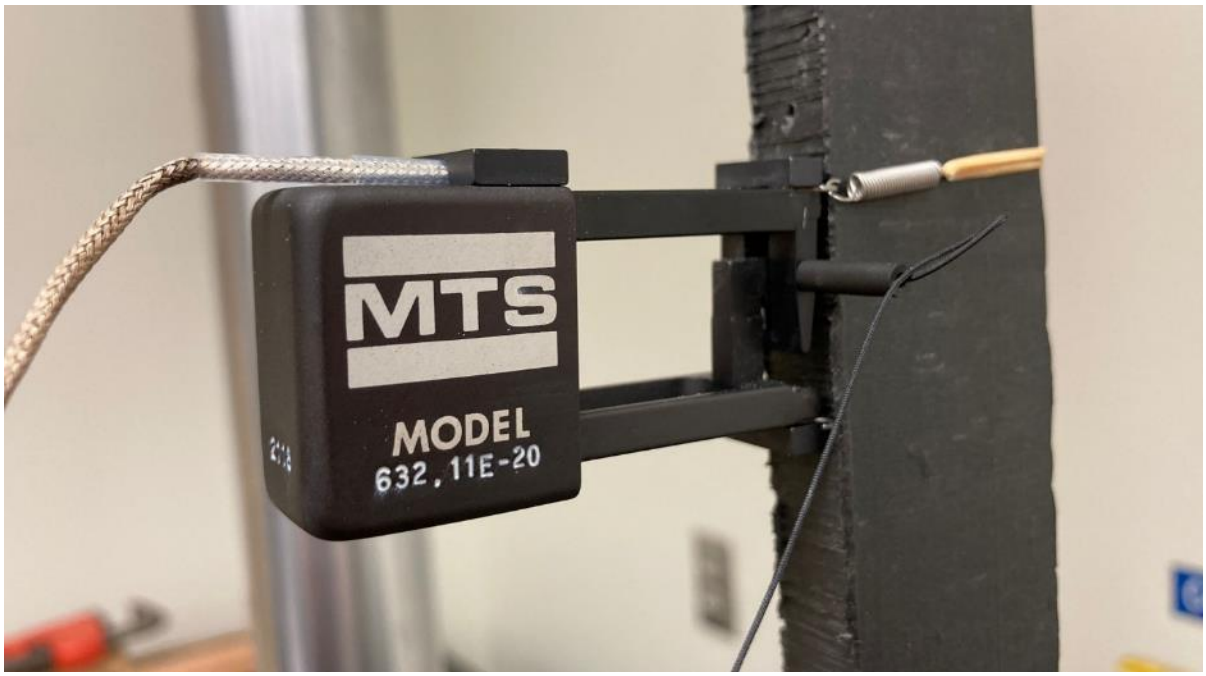

Figure 18. MTS 632.11E-20 Extensometer

4. EXPERIMENTAL METHODOLOGY

The experiments were conducted in the Materials and Structures Engineering Lab at the Department of Ocean Engineering at Texas A&M University. The research objective is to utilize the testing of samples of HDPE composite with different void volumes to develop an understanding of the effect of void volume fraction (V_{VF}) on specimen strength. To achieve this objective, HDPE composite blocks (crossties) were divided into four basic geometric regions within the crossties: outer (section A), middle two (section B), middle one (section C) and inner (section D) as shown in Figure 19. Thus, regions with different V_{VF} were obtained, where individual V_{VF} defined as:

$$V_{VF} = \frac{V_{void}}{V_{total}} \qquad (2)$$

As shown in Figure 19, the rounded corners of the HDPE composite were eliminated with the cuts. To obtain multiple specimens, the beam then was divided into five separate pieces and numbered as shown in Figure 20 and Figure 21. These samples have approximate cross sections of 1.40 X 0.75 in and lengths of 12 in. All cuts were made with a miter saw (Figure 22) and a band saw (Figure 23) available in the Materials and Structures Engineering Lab.

After obtaining samples, each sample was reduced to a constant thickness using a planer (Figure 24). Tensile tests were performed on the MTS Test Machine on the samples with similar dimensions and different V_{VF}. In addition, sets of HDPE composite samples were tested with varying strain rates to determine the effect of strain rate on the stress-strain response.

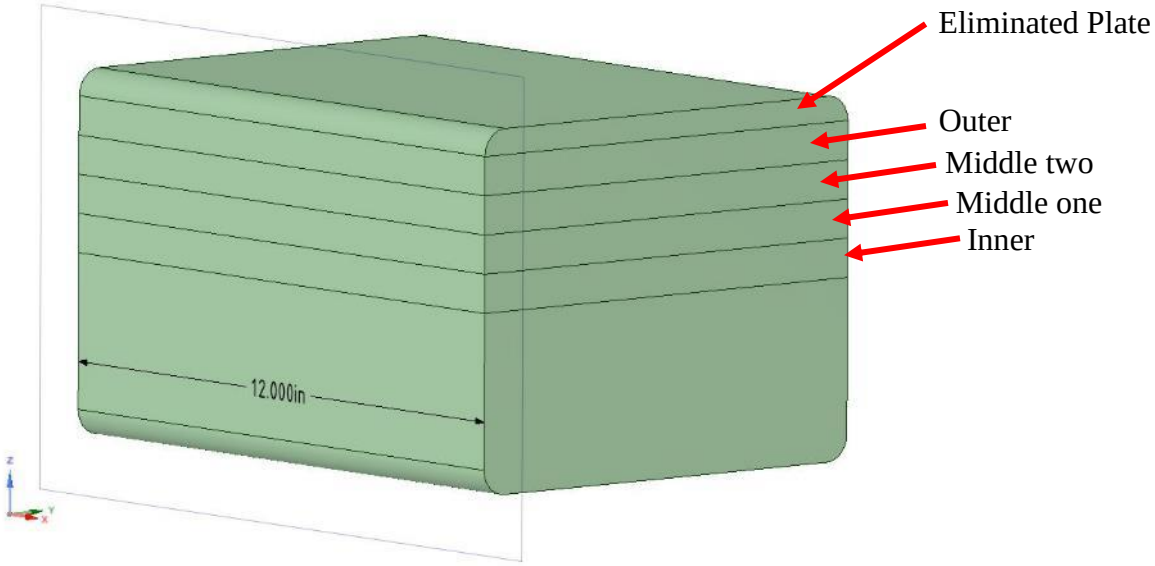

Figure 19. 3D Drawing of Recycled HDPE Composite Block

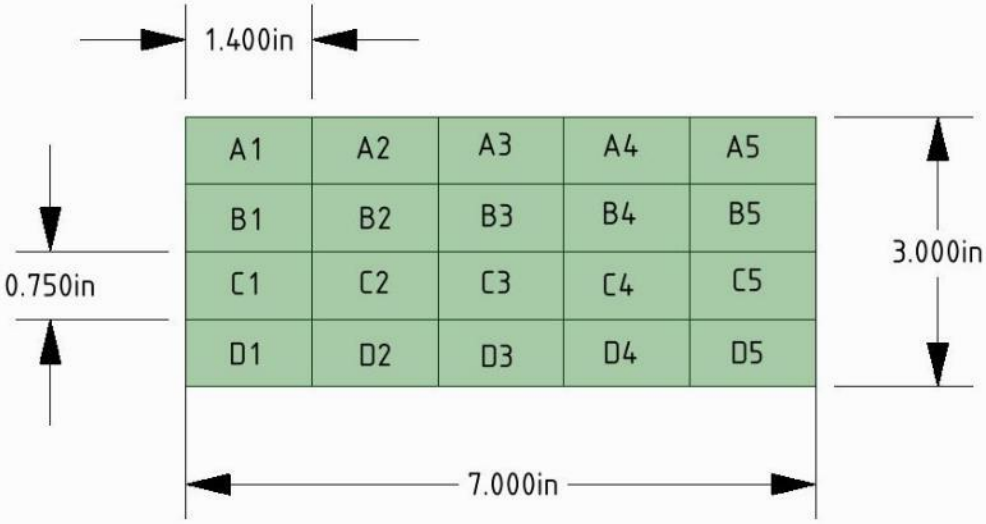

Figure 20. Front View and Partitions of HDPE Composite Block

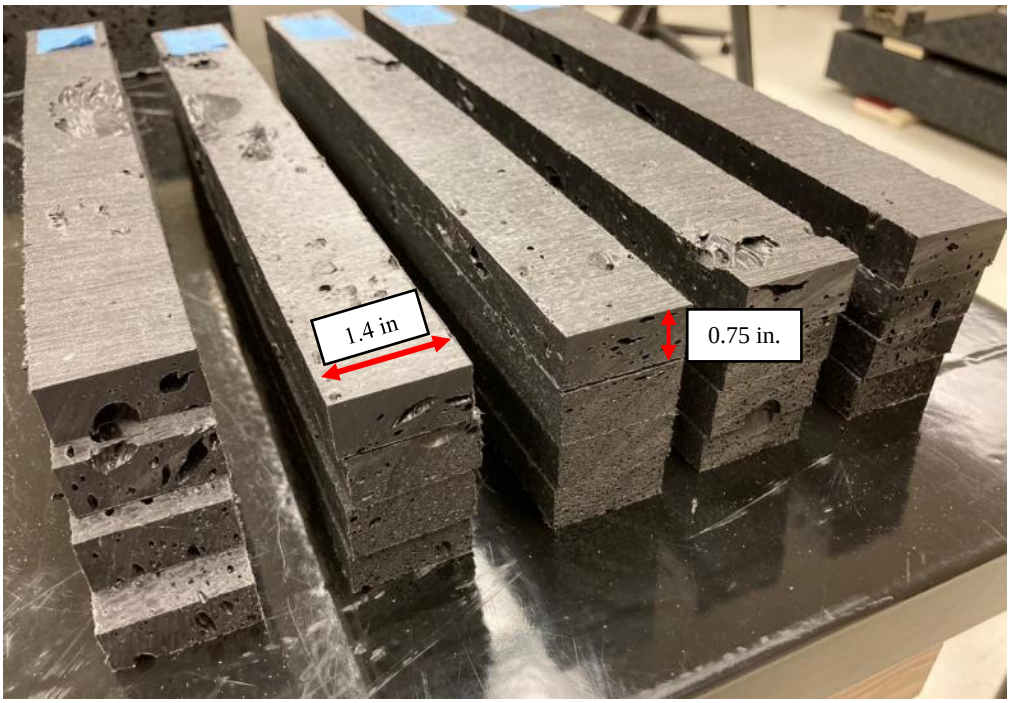

Figure 21. Samples from different Partitions of the HDPE Composite Block

Figure 22. Miter Saw in Materials and Structures Engineering Lab

Figure 23. Band Saw in Materials and Structures Engineering Lab

Figure 24. Planer in Materials and Structures Engineering Lab

4.1 Calibration

Calibrating the control of the test machine and the DAQ is critical for experimental accuracy. The extensometer and the load cell are both based on strain gages which produce quite small resistance changes as their readings change. To amplify the signals sufficiently to obtain voltages that have a high signal-to-noise ratio, both are transmitted through a Wheatstone bridge amplifier with adjustable gain and balance.

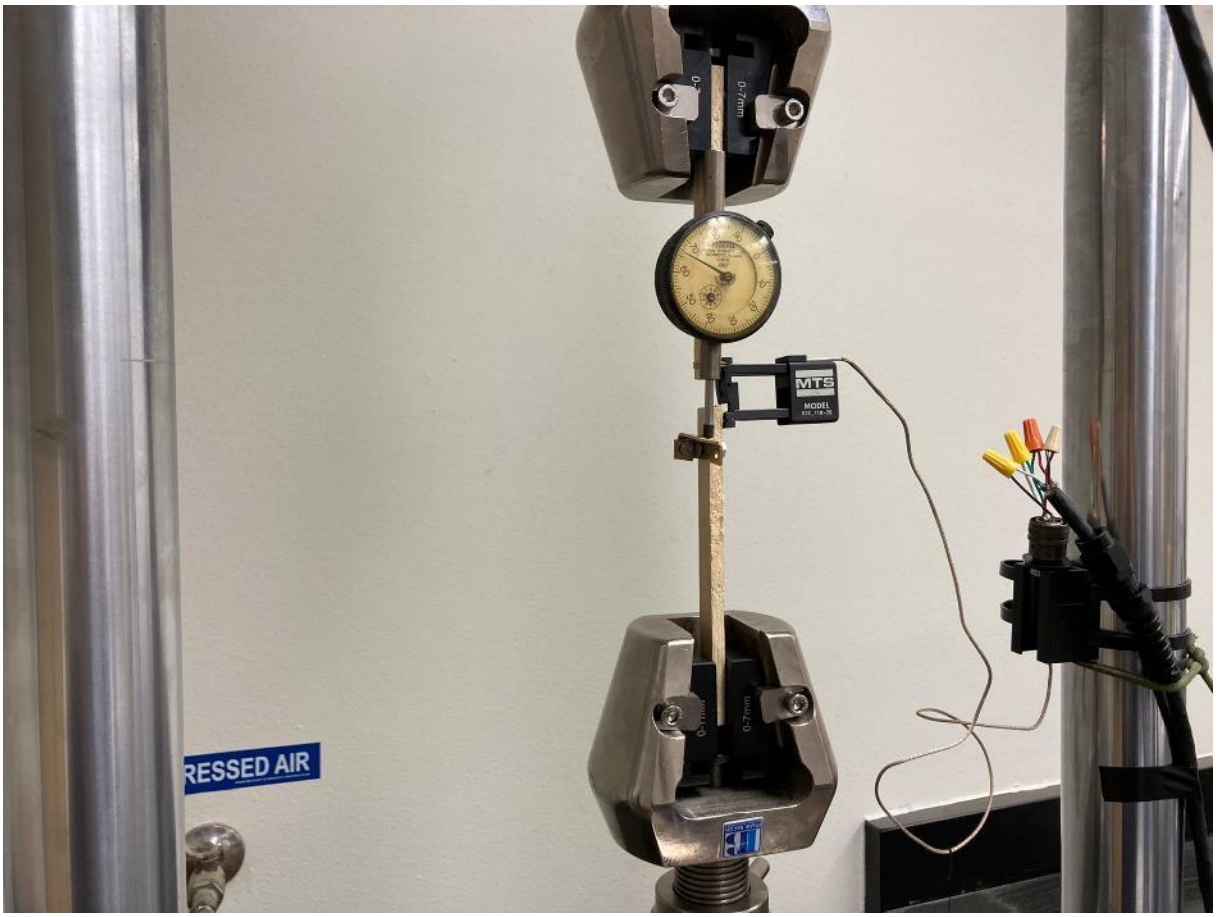

Figure 25. Calibration of the Extensometer

Calibration of the extensometer is performed by comparing the electronic output to a mechanical dial displacement gage as seen in Figure 25 with an accuracy of 0.001 inches over the extensometer's range of 0.200 inches (0.5%).

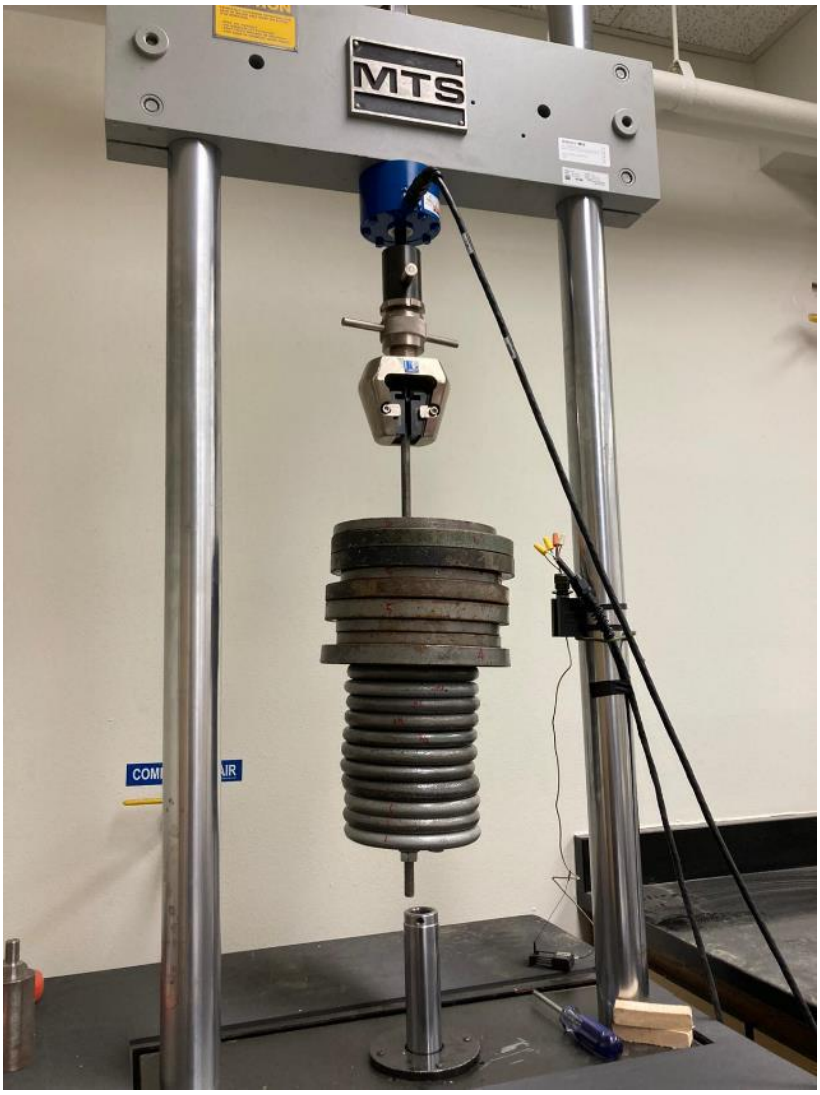

Figure 26. Calibration of the Load Cell

Calibration of the load cell was performed by comparing electronic output to a series loads applied by known weights as seen in Figure 26. The load value, which is read as voltage, was compared with the weights. The weights were weighed to an accuracy of 0.1 lbs. for an anticipated accuracy of 0.5 % for the collected weights. After calculating the load corresponding to the unit voltage, the calibration was further confirmed based on stress-strain testing in the proportional region for known materials such as 6061 aluminum, 6063 aluminum, 316 steel, 304 steel and brass. In this manner the elastic modulus could be confirmed from the combined load cell and strain gage

readings and compared with expected values for those materials. An example is shown in Figure 27 and Figure 28 where the elastic modulus of 6061 aluminum is shown to be 9.58xE6 psi, in the expected range for 6061 aluminum.

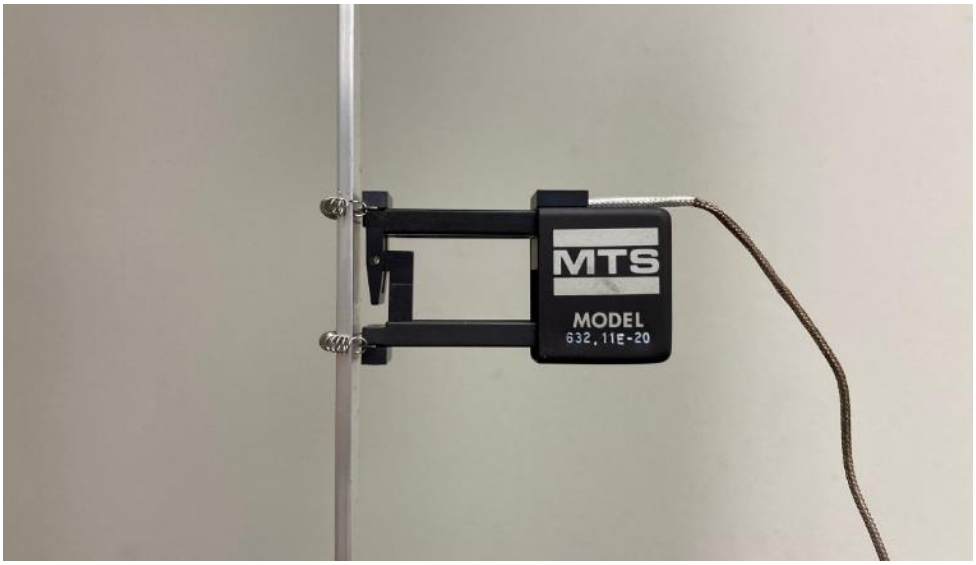

Figure 27. Extensometer Calibration During the Aluminum 6061 Test

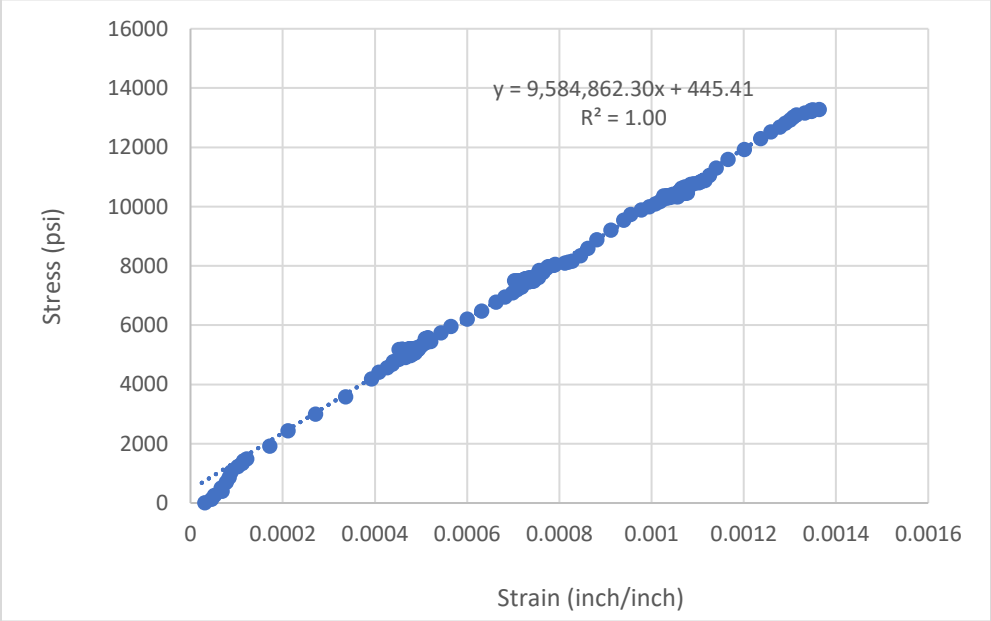

Figure 28. Stress-Strain Curve for Testing Aluminum 6061

4.2 Calculation of Void Volume Fraction

To calculate the density of HDPE composite (ρ_{hdpe}), several samples with negligible voids were used according to equation (3):

$$\rho_{hdpe} = \frac{m_{hdpe}}{V_{hdpe}} \quad (3)$$

The resulting density without voids was calculated to be 1.0558 g/cm^3.

For the V_{VF}, the geometric measurements of each sample were taken and each piece was weighed separately. The densities of each sample were calculated from the calculated volume (V) and mass (m) values according to equation (4):

$$\rho_{sample} = \frac{m_{sample}}{V_{sample}} \quad (4)$$

With the help of the equations (5) and (6), idealized mass (or expected mass without voids) and missing mass (the loss of mass due to the presence of voids) were calculated for each piece.

$$m_{ideal} = V_{sample} \times \rho_{hdpe} \quad (5)$$

$$m_{missing} = m_{ideal} - m_{sample} \quad (6)$$

The missing volume, the equivalent void volume of the entire sample, was calculated according to equation (7) below:

$$V_{missing} = \frac{m_{sample}}{\rho_{hdpe}} \quad (7)$$

Finally, V_{VF} (Table 1) was obtained for each specimen according to equation (8). V_{VF} ranged from 8 to 59%.

$$V_{VF} = \frac{V_{missing}}{V_{sample}} \quad (8)$$

Table 1. Void Volume Fraction Calculations

Sample	Width (inch)	Height (inch)	Length (inch)	Cross Sectional Area (inch^2)	Volume (inch^3)	Volume (cm^3)	Mass (g)	Density (g/cm^3)	Idealized mass (g)	Missing mass (g)	Missing volume (cm^3)	V_{VF}
C2	1.66	0.52	12.19	0.87	10.58	173.39	167.72	0.97	183.08	15.36	14.54	0.08
C3	1.61	0.51	12.12	0.82	9.96	163.24	158.85	0.97	172.36	13.51	12.79	0.08
C4	1.63	0.51	12.12	0.83	10.08	165.12	160.83	0.97	174.35	13.52	12.80	0.08
B2	1.58	0.54	12.12	0.85	10.28	168.51	128.57	0.76	177.93	49.36	46.75	0.28
B4	1.61	0.55	12.12	0.88	10.63	174.27	122.66	0.70	184.01	61.35	58.10	0.33
A2	1.57	0.54	12.19	0.84	10.22	167.54	104.98	0.63	176.90	71.92	68.11	0.41
A3	1.59	0.54	12.12	0.86	10.38	170.11	87.25	0.51	179.61	92.36	87.48	0.51
A4	1.58	0.51	12.12	0.81	9.77	160.04	94.33	0.59	168.98	74.65	70.70	0.44
B5	1.63	0.52	12.12	0.84	10.23	167.70	155.10	0.92	177.06	21.96	20.80	0.12
A1_2	1.37	0.51	12.00	0.69	8.34	136.66	123.89	0.91	144.29	20.40	19.32	0.14
A2_2	1.37	0.51	10.62	0.70	7.39	121.18	91.18	0.75	127.95	36.77	34.82	0.29
A3_2	1.31	0.51	11.93	0.67	7.95	130.24	94.92	0.73	137.51	42.59	40.34	0.31
A4_2	1.27	0.51	8.00	0.65	5.20	85.18	69.23	0.81	89.93	20.70	19.61	0.23
A5_2	1.35	0.51	7.81	0.69	5.41	88.63	74.05	0.84	93.59	19.54	18.50	0.21
B1_2	1.35	0.51	8.12	0.69	5.58	91.48	72.40	0.79	96.59	24.19	22.91	0.25
B2_2	1.35	0.51	10.68	0.69	7.36	120.61	70.38	0.58	127.35	56.97	53.95	0.45
B3_2	1.32	0.51	7.18	0.68	4.85	79.49	41.73	0.52	83.93	42.20	39.97	0.50
B4_2	1.25	0.51	8.00	0.64	5.10	83.57	51.30	0.61	88.24	36.94	34.99	0.42
B5_2	1.36	0.51	7.90	0.69	5.48	89.84	68.03	0.76	94.85	26.82	25.40	0.28
C1_2	1.34	0.51	10.31	0.69	7.08	116.03	85.10	0.73	122.51	37.41	35.43	0.31
C2_2	1.36	0.51	10.38	0.69	7.17	117.58	59.72	0.51	124.14	64.42	61.02	0.52
C3_2	1.32	0.51	10.38	0.67	6.96	114.11	56.08	0.49	120.48	64.40	60.99	0.53
C4_2	1.25	0.51	7.70	0.64	4.92	80.70	43.18	0.54	85.20	42.02	39.80	0.49
C5_2	1.35	0.51	11.88	0.69	8.18	134.04	96.45	0.72	141.53	45.08	42.70	0.32
D1_2	1.35	0.51	10.81	0.69	7.44	121.96	90.75	0.74	128.78	38.03	36.01	0.30
D2_2	1.34	0.50	10.18	0.67	6.82	111.77	48.01	0.43	118.01	70.00	66.30	0.59

D3_2	1.31	0.47	8.37	0.62	5.16	84.58	37.13	0.44	89.30	52.17	49.41	0.58
D4_2	1.26	0.50	8.12	0.64	5.16	84.53	41.95	0.50	89.26	47.31	44.80	0.53
D5_2	1.35	0.51	9.12	0.69	6.25	102.49	64.50	0.63	108.22	43.72	41.40	0.40
A1_1	1.36	0.51	12.00	0.68	8.21	134.56	122.65	0.91	142.07	19.42	18.40	0.14
A2_1	1.28	0.51	12.00	0.65	7.79	127.62	111.12	0.87	134.75	23.63	22.38	0.18
A3_1	1.36	0.51	12.00	0.69	8.31	136.19	118.13	0.87	143.80	25.67	24.31	0.18
A4_1	1.23	0.51	12.00	0.63	7.51	123.05	109.34	0.89	129.93	20.59	19.50	0.16
A5_1	1.28	0.50	12.00	0.64	7.66	125.46	109.16	0.87	132.47	23.31	22.07	0.18
B1_1	1.36	0.51	12.00	0.69	8.31	136.16	113.44	0.83	143.76	30.32	28.72	0.21
B2_1	1.26	0.51	12.00	0.64	7.69	125.97	90.16	0.72	133.00	42.84	40.58	0.32
B3_1	1.36	0.52	11.88	0.70	8.30	135.95	96.78	0.71	143.55	46.77	44.29	0.32
B4_1	1.21	0.51	9.75	0.61	5.99	98.21	72.98	0.74	103.70	30.72	29.09	0.30
C2_1	1.32	0.51	11.88	0.67	8.00	131.06	79.02	0.60	138.38	59.36	56.22	0.43
C3_1	1.36	0.51	11.88	0.70	8.26	135.36	80.15	0.59	142.92	62.77	59.45	0.44
C4_1	1.22	0.51	11.88	0.62	7.42	121.64	70.76	0.58	128.44	57.68	54.62	0.45
C5_1	1.31	0.51	8.75	0.67	5.85	95.80	72.82	0.76	101.15	28.33	26.83	0.28
D4_1	1.26	0.51	10.25	0.64	6.58	107.76	56.31	0.52	113.78	57.47	54.43	0.51
D5_1	1.31	0.52	8.36	0.68	5.67	92.96	68.34	0.74	98.16	29.82	28.24	0.30

4.3 Experimental Test Procedure

Each sample was mounted in the test machine by locating the crosshead and tightening the grips as seen in Figure 29. The extensometer was then attached to the specimen producing a 1.000 inch gage length. The test was run from the LabVIEW software, which adjusted the crosshead speed based on the desired strain rate. The tests were run under monotonic loading until failure. The force read from the load cell was divided by the cross-sectional area to give the average axial stress. In the reporting this average stress will simply be called the "stress" or "ultimate stress".

Following testing, the failure location was noted and the failure surface was observed and photographed. Very large voids in some samples (Figure 30) caused the local V_{VF} value to be extremely high. These samples were noted as exceptional, and studied further to determine if the local void rendered the tests invalid.

Figure 29. HDPE Composite Sample Mounted for Testing

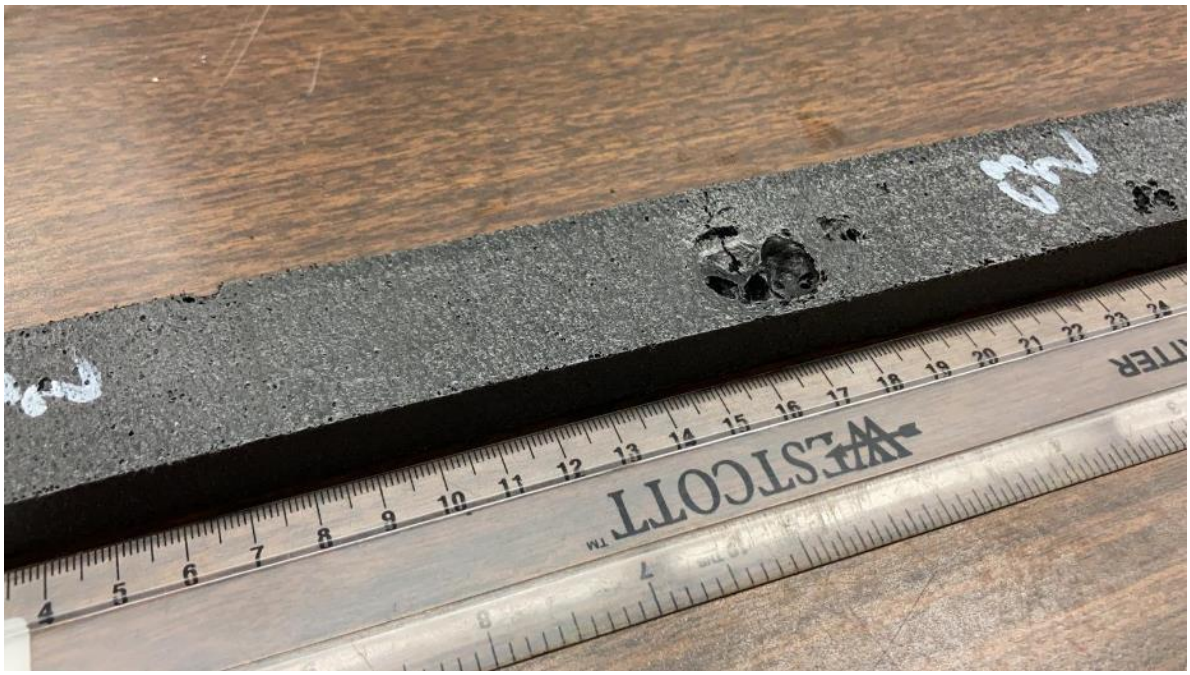

Figure 30. Large voids cause exceptional results and possibly invalid results

4.4 Experimental Error

A primary result of the experiments was the generation of a stress-strain curve for each specimen. These curves then produced three important material properties:

a) Elastic modulus

b) Ultimate stress

c) Ultimate strain

Based on the calibration of the testing apparatus, the instrumentation accuracies are 0.5% for the 1-inch gage length extensometer, and 0.5% for the load cell. The resolution from the DAQ system into LabView gave resolutions of 4.58E-06 for strain (inch/inch) and 0.12 lbs. for load.

The measurement of the volume and dimensions of the specimens were accurate to the nearest 0.001". While some geometric differences existed along the lengths of the specimens, the volume accuracy is estimated (based on measurement errors of 0.001" and dimension variations locally to 0.010") to be on the order of 1%.

The experimental results for stress are based on the local force over the gage length and the cross-sectional area in the gage length region.

$$\sigma_{experiment} = \frac{F_{load\ cell}}{A_{Gage\ length}} \tag{9}$$

Thus, the anticipated, worst-case accuracy of stress values from the load cell and dimensional measurements is 1.5%.

Experimental errors from two other sources are noteworthy. First, the specimens are simply rectangular prisms. Standard practice for testing metals includes thinning the specimen over the gage length to create a dog-bone specimen. Doing so makes the local stress over the gage length increase and thus the failure is likely to occur in the gage length and not near the grips. For the current tests on HDPE composite, not creating dog-bone specimens introduces high local, 3D stresses near the grips that can lead to failure near the grips. Thus, for tests in which the failure was located outside the gage length, the ultimate stress and ultimate strain values from these tests will be less than the actual properties found if the test could have continued until failure occurred in the gage length. For the ultimate stress, this difference is expected to be slight (possibly 5 to 10% because of the plateau in the stress-strain curve of HDPE composite). However, the ultimate strain values are expected to be significantly higher if the failure is not in the gage length.

The second source of error arises because of local void configurations. Specifically, locally large voids create locally high V_{VF} and locally high stresses. In effect these local regions should be treated as a higher V_{VF} result. In the current study, the failure surfaces are examined and photographed and certain specimens are labeled as "invalid" if the local void renders the results inaccurate. Finally, the presence of a local void can also influence local bending in the gage length. This will be discussed in Section 5 and can significantly dampen or amplify the strain reading.

5. RESULTS

5.1 Overview of Void Populations

A total of 44 samples with varying V_{VF} were tested and stress-strain curves constructed for each sample. The tests were carried out with samples ranging from 8% V_{VF} to 60% $V_{VF.}$ Examples of structural differences between samples with high and low void content can be seen in Figure 31.

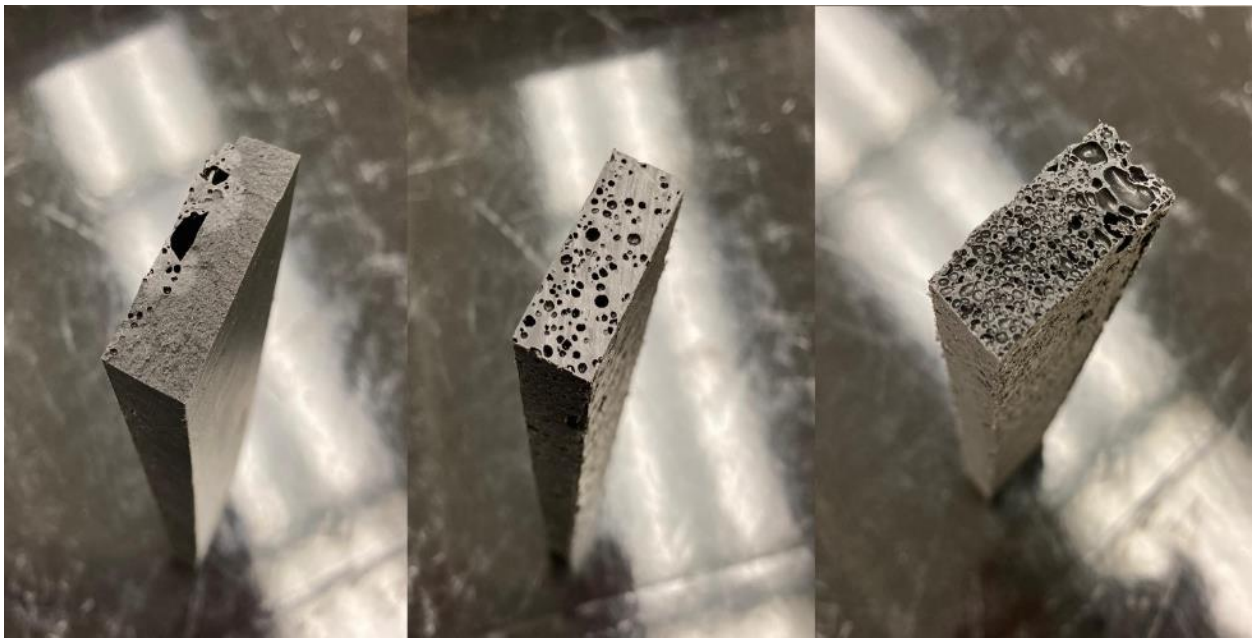

Figure 31. Samples with 8%, 30% and 50% V_{VF}

Samples with 8% V_{VF} generally appear to have a solid structure, with voids approximately 8 mm diameter and some smaller voids. On the other hand, Samples with 30% V_{VF} contain several voids with a diameter of 2mm and smaller. Samples with 50% V_{VF} can have large voids with approximate diameters of 5 to 8 mm and also have many smaller voids throughout the entire sample.

5.2 Specimen Results: Invalid and Valid Tests

Results from each test are summarized in Table 2. Individual stress-strain curves and post-test photographs are provided in Appendix A. As has been discussed, in several specimens, the presence of a large void significantly influenced the local behavior and the results. These invalid tests are summarized in Table 3 and are further described in Appendix B.

It is observed that with increasing $V_{VF,}$ Young's modulus (E), ultimate stress (σ_{ult}) and ultimate strain (ϵ_{ult}) values decreased significantly.

Table 2. Material Properties of Samples of Valid Tests

Sample	V_{VF}	Ultimate Stress (psi)	Ultimate Strain (inch/inch)	E (psi)
C4	7.75%	2424	0.0377	430000
C3	7.84%	2413	0.0326	350000
C2	8.39%	2153	0.0213	337000
B5	12.40%	2031	0.0184	332000
A1_1	13.67%	2047	0.018	287000
A1_2	14.14%	1862	0.02	273000
A4_1	16.72%	2140	0.022	250000
A2_1	17.53%	1849	0.021	224000
A5_1	17.59%	1973	0.021	196000
A3_1	17.85%	1754	0.021	218000
A5_2	20.87%	1354	0.015	174000
B1_1	21.09%	1921	0.0175	208000
A4_2	23.02%	1333	0.014	150000
B1_2	25.04%	1301	0.016	114000
B2	27.74%	1291	0.016	171500
C5_1	28.01%	1216	0.015	123000
A2_2	28.74%	1104	0.016	171000
B4_1	29.62%	1221	0.017	166000
D5_1	30.38%	1048	0.017	140000
C1_2	30.54%	913	0.015	117000
B3_1	32.58%	1170	0.016	136000
B4	33.34%	933	0.015	110000
D5_2	40.40%	794	0.009	128000
A2	40.65%	783	0.011	104000

C2_1	42.90%	995	0.016	124000
C3_1	43.92%	900	0.017	110000
A4	44.18%	729	0.011	91000
B2_2	44.73%	672	0.012	78000
C4_1	44.91%	830	0.015	109000
D4_1	50.51%	578	0.01	82000
A3	51.42%	460	0.009	69000
C2_2	51.89%	438	0.009	50000
C3_2	53.45%	315	0.009	48000
D2_2	59.32%	287	0.007	58000

Table 3. Material Properties of Samples of Invalid Tests

Sample	V_{VF}	Ultimate Stress (psi)	Ultimate Strain (inch/inch)	E (psi)
B5_2	28.28%	1136	0.01	230000
D1_2	29.53%	1067	0.03	90000
A3_2	30.97%	505	0.006	200000
C5_2	31.85%	1042	0.009	236000
B2_1	32.21%	1209	0.011	215000
B4_2	41.86%	729	0.019	68000
C4_2	49.32%	651	0.02	58000
B3_2	50.28%	664	0.022	78000
D4_2	53.00%	571	0.018	61000
D3_2	58.42%	324	0.014	49000

5.3 Stress-Strain Curves and Influence of V_{VF}

Figure 32 shows the change of material properties of HDPE composite as a function of $V_{VF.}$

In cases where the samples fail outside the gauge length of the extensometer, the measured strain represents the local values. In other words, the measured strain value should be considered as the minimum ultimate strain for that sample. The ultimate strain values from all the test (valid and invalid) are shown in Figure 33. As shown, for low V_{VF}, the HDPE composite exhibits approximately 4% strain-to-failure. As the V_{VF} increases, the strain to failure drops, eventually dropping lower than 1% as the V_{VF} goes above 50%.

The changes in elastic modulus, stress and strain values as functions of increasing V_{VF} are given in the Figure 34, Figure 35 and Figure 36. Simple curve fits and their correlation coefficients are also provided, noting that the curve fits are only valid over the V_{VF} range (and cannot be extrapolated to 0% V_{VF} in their current form). Also shown in the figures are shifted curves representing ±2σ or 2 standard deviations, encompassing 95% of the data points. Based on this, for the elastic modulus, ultimate stress, and ultimate strain the standard deviations (σ) were found to be 29000 psi, 157 psi and 0.3% strain, respectively.

Increasing V_{VF} from 10% to 20% reduces the elastic modulus of HDPE composite by 45%. With an increase in V_{VF} from 20% to 40%, there is a 40% decrease in elastic modulus. Also, the change of void content from 40% to 60% causes a 45% decrease in elastic modulus.

The ultimate stress is reduced by approximately half as the V_{VF} goes from 10% to 30% and again from 30% to 50%. This is a larger drop than expected based simply on the loss of cross-sectional area due to the increase in void percentage and is presumably due to the local stress concentrations that develop around the individual voids. Finally, as noted, most samples did not fail in the gage length because of the shape of the samples (i.e., no dog-bone specimen shape) and thus the predicted ultimate stresses are somewhat erroneous.

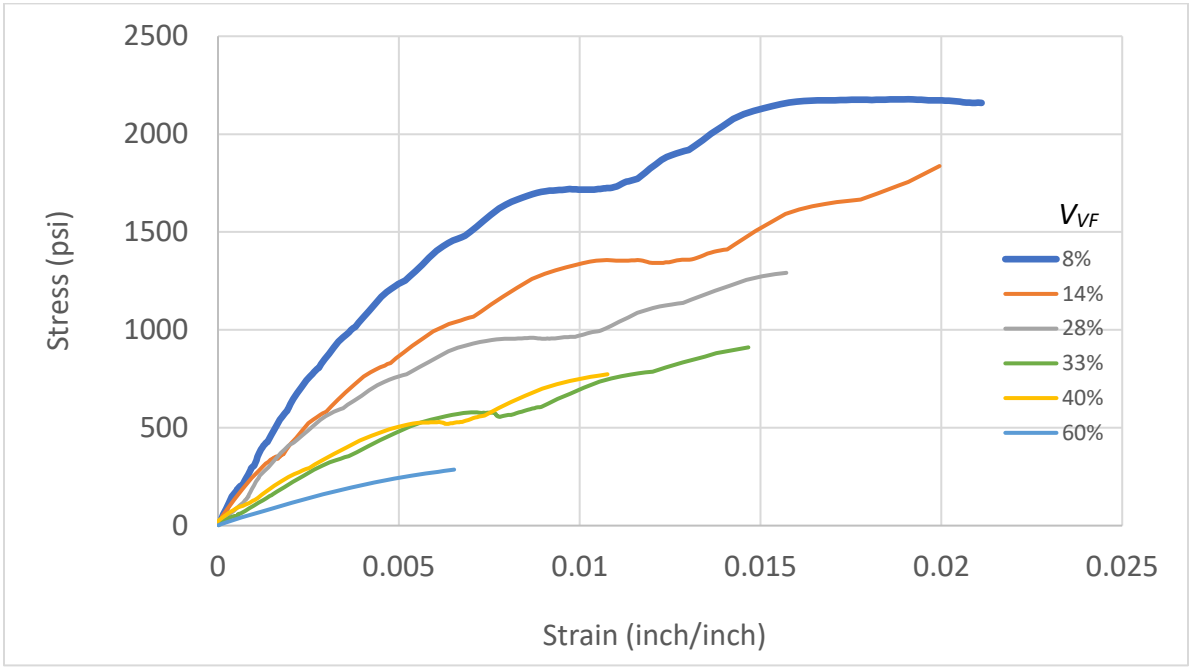

Figure 32. Stress-Strain Curves of Samples with Different V_{VF}

Note: The samples used in this graph are: C2_1, A1_2, B2_1, B4_1, A2_1, D2_2

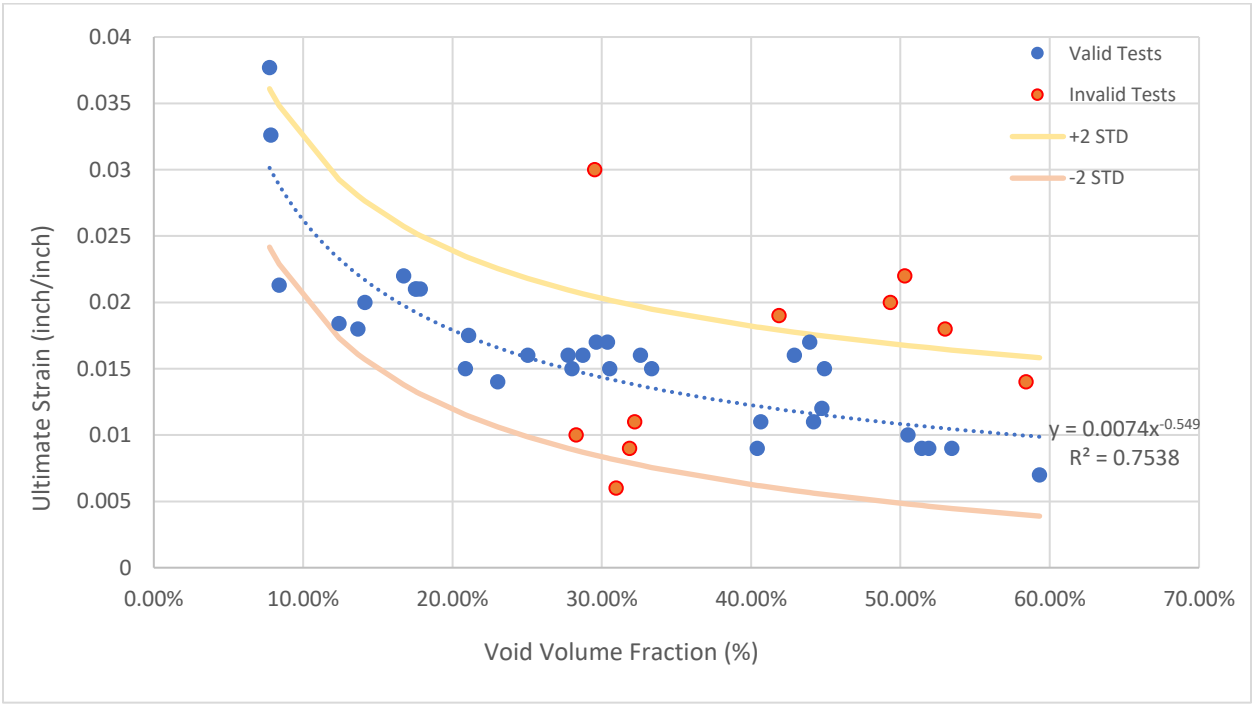

Figure 33. Change of Ultimate Strain with V_{VF} for Valid and Invalid Tests

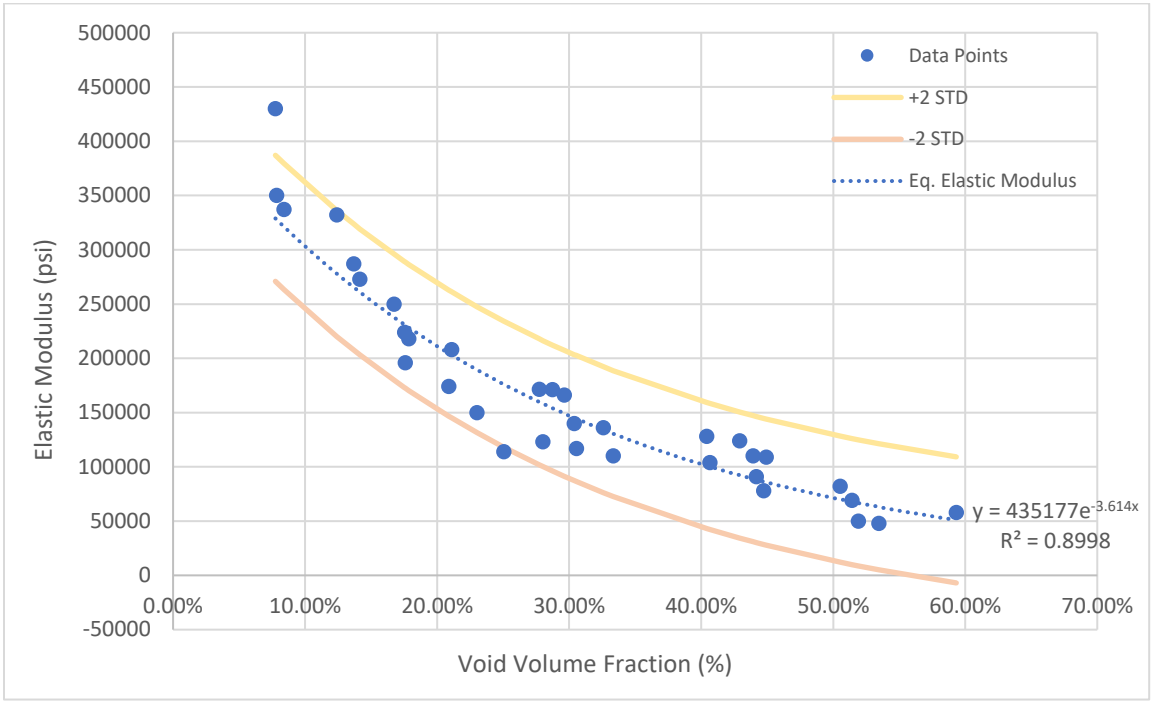

Figure 34. Change of Elastic Modulus with the V_{VF}

`

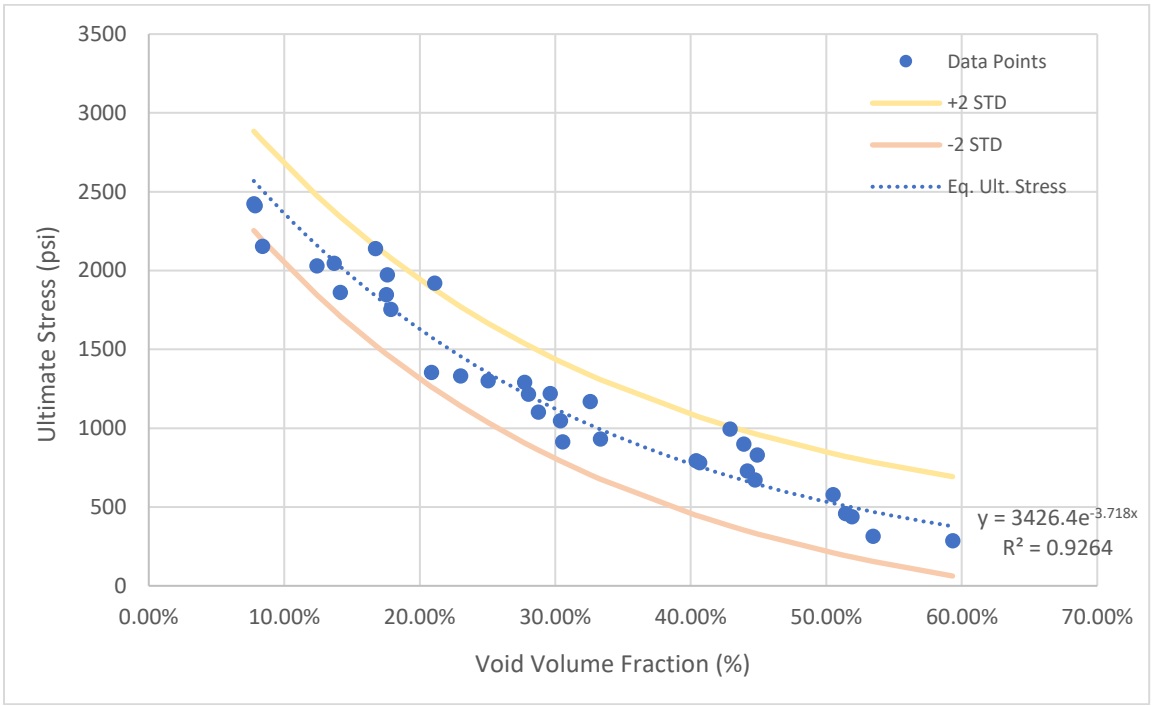

Figure 35. Change of Stress with the V_{VF}

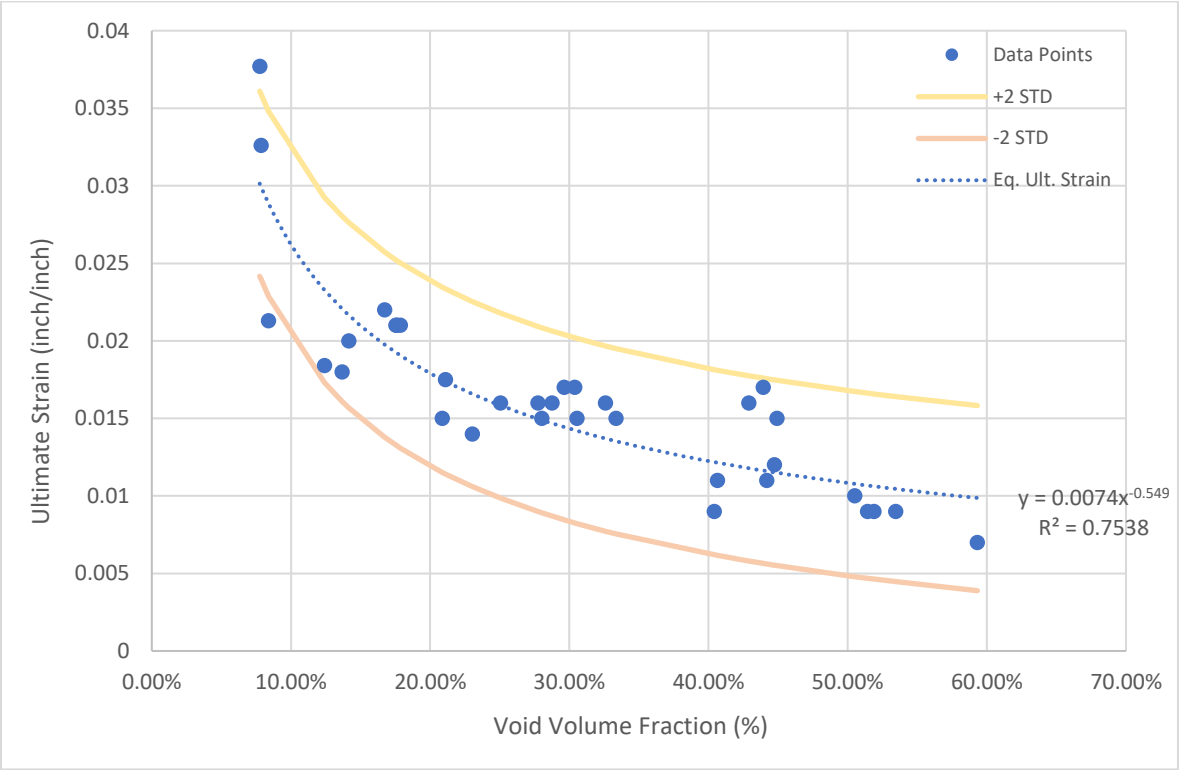

Figure 36. Change of Ultimate Strain with the V_{VF}

5.4 Influence of Strain Rate

To understand the effect of strain rate on material properties, samples with similar V_{VF} were tested at different strain rates. Tests were divided into two groups: slow and fast tests. While slow tests have low strain rates with test durations from 2 to 6 minutes, fast tests take 5 to 20 seconds and have high strain rate values. Slow tests run at a strain rate of ~10^{-4} order of magnitude, and fast tests at a strain rate of ~10^{-3} order of magnitude.

The effect of the increase in strain rate on materials with similar V_{VF} is shown in Figure 37, Figure 38 and Figure 39 for three similar V_{VF}. In each comparison, the higher strain rate test

displayed a steeper initial shape (higher initial modulus) and reached a higher ultimate stress and ultimate strain.

The increase of the strain rate from 10^{-4} to 10^{-3} order of magnitude caused an average 18% increase in measured elastic modulus values. The increase of the E values can be seen in Figure 40.

Table 4 gives all test results to show the effect of strain rate on material properties of HDPE composite.

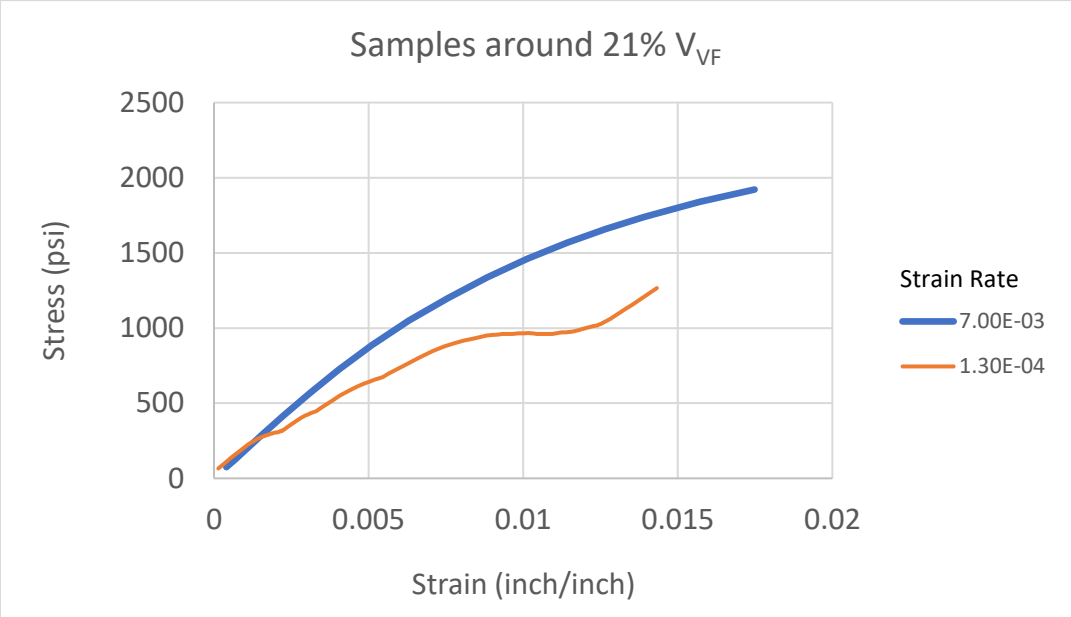

Figure 37. Strain Rate Effect on Samples with 21% V_{VF}

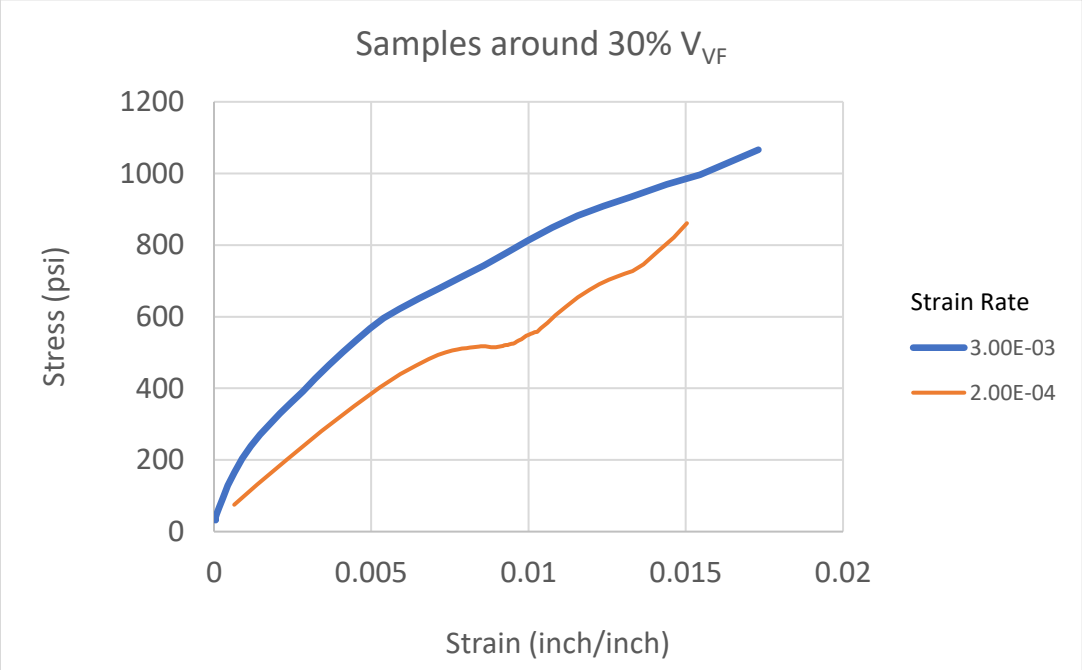

Figure 38. Strain Rate Effect on Samples with 30% V_{VF}

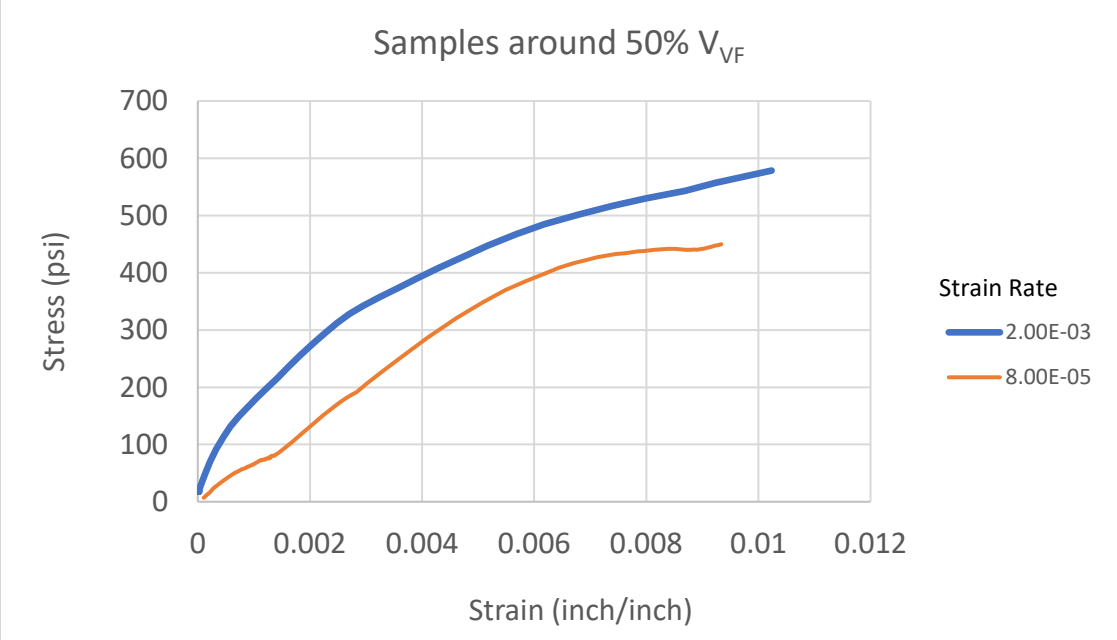

Figure 39. Strain Rate Effect on Samples with 50% V_{VF}

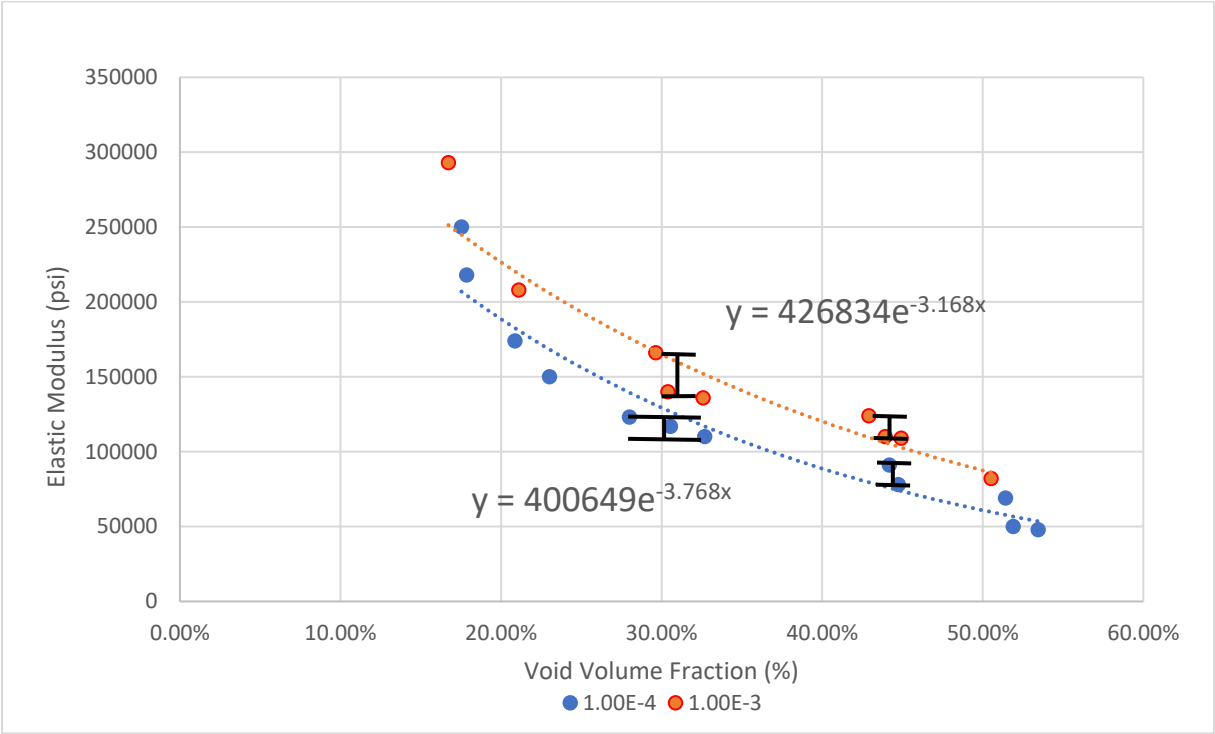

Figure 40. Strain Rate Effect on Elastic Modulus

Note: The error bands approximate the range on similar V_{VF} results for comparisons between the two strain rates.

Table 4. Change of the Material Properties with the Strain Rate

Sample	V_{VF}	Ultimate Stress (psi)	Ultimate Strain (inch/inch)	E (psi)	Strain Rate
A4_1	16.72%	2140	0.022	293000	2.00E-03
A2_1	17.53%	1849	0.021	250000	1.60E-04
A3_1	17.85%	1754	0.021	218000	1.60E-04
A5_2	20.87%	1354	0.0155	174000	1.30E-04
B1_1	21.09%	1921	0.0175	208000	7.00E-03
A4_2	23.02%	1333	0.014	150000	1.20E-04
B4_1	29.62%	1221	0.017	166000	3.00E-03
D5_1	30.38%	1048	0.017	140000	3.00E-03
C1_2	30.54%	913	0.015	117000	2.00E-04
B3_1	32.58%	1170	0.016	136000	1.00E-03
B4	32.68%	933	0.015	110000	1.20E-04
C2_1	42.90%	995	0.016	124000	4.00E-03
C3_1	43.92%	900	0.017	110000	1.10E-03
A4	44.18%	729	0.011	91000	1.00E-04
B2_2	44.73%	672	0.012	78000	6.00E-04
C4_1	44.91%	830	0.015	109000	3.70E-03
D4_1	50.51%	578	0.01	82000	2.00E-03
A3	51.42%	460	0.009	69000	8.00E-05
C2_2	51.89%	438	0.009	50000	6.00E-04
C3_2	53.45%	315	0.009	48000	6.40E-04

6. CONCLUSIONS

Within this research a relationship between the stress-strain material response and V_{VF} for properties HDPE composite was investigated. Furthermore, the strain rate effect on material properties was observed. The results revealed a clear trend from the obtained data- the material properties dependence on the V_{VF} and strain rate. Parameters for samples were calculated on the investigated range of V_{VF} (8–60%). With higher V_{VF}, Young's modulus (E), ultimate stress (σ_{ult}) and ultimate strain (ϵ_{ult}) values all decreased. Also, with higher strain rate tests, HDPE composite responded with a higher modulus (stiffer) and ultimate stresses and strains compared to slower test rates.

Based on the obtained experimental results, the following conclusions can also be made:

1- For tests in which the failure was located outside the gage length, the ultimate stress and ultimate strain values from these tests will be less than the actual properties found if the test could have continued until failure occurred in the gage length.

2- Large voids affect the results significantly. Since large voids cause a decrease of local area, local stresses can reach very high values, thereby substantially reducing ultimate strength.

3- Within the cross section, the local stresses and displacements (ergo strains) can be a function of local, large voids. The proximity of the f extensometer to local, large voids can influence the results since the extensometer is taken as the average strain across the gage length and is assumed not to vary spatially. Local bending may cause the measured values to be incorrect.

In summary, due to its wide range of applications, HDPE has sparked widespread attention all over the world. The effects of V_{VF} and strain rate are important since structures built from this

material are subjected to a range of loadings and environments. The outcomes of this study may help to better predict the mechanical performance of HDPE composite components and structures.

This research also succeeded in calibrating the test machine and establishing initial programs in LabVIEW that can be expanded and improved in the future as further testing is performed, including fatigue testing.

Further work could be performed to clarify the results. For example, the limitation of the use of rectangular prisms for the specimens (vs dog-boned specimens) resulted in many tests failing near the grips, where there is a stress concentration from the compressive force from the grips. Modifying the specimen shape may clarify the ultimate stress and ultimate strain. The void populations, distributions, and influence of large voids locally and globally should be further studied to determine their influence both in specimens and in a complete crosstie.

REFERENCES

Adamczak, S., Bochnia, J., & Kundera, C. (2012). Metrology and Measurement Systems Stress and Strain Measurements in Static Tensile Tests. *Metrol. Meas. Syst, XIX* (3), 531–540. www.metrology.pg.gda.pl

Akash, M. P., & Vasudevan, A. (2021). Experimental analysis of recycled thermoplastic material. *Materials Today: Proceedings*, *45*, 6198–6203. https://doi.org/10.1016/J.MATPR.2020.10.516

Amjadi, M., & Fatemi, A. (2020). Tensile Behavior of High-Density Polyethylene Including the Effects of Processing Technique, Thickness, Temperature, and Strain Rate. *Polymers 2020, Vol. 12, Page 1857*, *12*(9), 1857. https://doi.org/10.3390/POLYM12091857

Asenjo, J., Vargas, V. I., & Mora, J. (2018). Control and data acquisition system for SCR-1 Stellarator. *Fusion Engineering and Design*, *129*, 263–268. https://doi.org/10.1016/J.FUSENGDES.2018.02.061

ASTM E8 / E8M-21, Standard Test Methods for Tension Testing of Metallic Materials, ASTM International, West Conshohocken, PA, 2021, www.astm.org

Ashpiz, E. S., Egorov, A. O., & Ushakov, A. E. (2010). *Application of composite materials for the protection of sea shores and engineering structures against the impact of waves*. https://doi.org/10.2495/ISLANDS100201

Badache, A., Benosman, A. S., Senhadji, Y., & Mouli, M. (2018). Thermo-physical and mechanical characteristics of sand-based lightweight composite mortars with recycled high-density polyethylene (HDPE). *Construction and Building Materials*, *163*, 40–52. https://doi.org/10.1016/J.CONBUILDMAT.2017.12.069

Bansal D. (2021), Real-Time Data Acquisition in Human Physiology Real-Time Acquisition, Processing, and Interpretation- A MATLAB-Based Approach https://doi.org/10.1016/B978-0-12-822118-1.00002-3

Bijaisoradat, O., Luttapreecha, M., & Manuspiya, H. (2020). Eco composites with synergistic combinations of natural rubber latex and wood flour toughened recycled HDPE. *Materials Today Communications*, *25*, 101483. https://doi.org/10.1016/J.MTCOMM.2020.101483

Broucke, B.V., Hegemann, J.D., Das, R., Oster, R., Hackl, K., Stössel, R., & Deutschland, E. (2007). Modelling of Textile Reinforced Composites Using Finite Element Tools and Investigation of The Influence of Porosity on Mechanical Properties.

Campbell, F. C. (2006). Polymer Matrix Composites. *Manufacturing Technology for Aerospace Structural Materials*, Chapter 7, 273–368. https://doi.org/10.1016/B978-185617495-4/50007-X

Corrosionpedia. *What is an Extensometer? - Definition from Corrosionpedia*. (n.d.). Retrieved September 11, 2021, from https://www.corrosionpedia.com/definition/4510/extensometer

Davis, J. R. (2004). *Tensile Testing*. https://www.asminternational.org/documents/10192/3465262/05105G_Chapter_1.pdf/e13396e8-a327-490a-a414-9bd1d2bc2bb8

Enderle, H. F. (2001). Polyethylene: High-density. *Encyclopedia of Materials: Science and Technology*, 7172–7180. https://doi.org/10.1016/B0-08-043152-6/01272-9

Gao, X., Yuan, L., Fu, Y., Yao, X., & Yang, H. (2020). Prediction of mechanical properties on 3D braided composites with void defects. *Composites Part B: Engineering*, *197*, 108164. https://doi.org/10.1016/J.COMPOSITESB.2020.108164

Harper, C.A. (2002), Handbook of Plastics, Elastomers, and Composites, McGraw-Hill, ISBN 0071384766

Holman, J.P. (2012), Experimental Methods for Engineers, McGraw-Hill, ISBN 0073529303

Koffi, A., Koffi, D., & Toubal, L. (2021). Mechanical properties and drop-weight impact performance of injection-molded HDPE/birch fiber composites. *Polymer Testing*, *93*, 106956. https://doi.org/10.1016/J.POLYMERTESTING.2020.106956

Limami, H., Manssouri, I., Cherkaoui, K., Saadaoui, M., & Khaldoun, A. (2020). Thermal performance of unfired lightweight clay bricks with HDPE & PET waste plastics additives. *Journal of Building Engineering*, *30*, 101251. https://doi.org/10.1016/J.JOBE.2020.101251

Macek, W., Zawiślak, S., Deptuła, A., & Ulewicz, R. (2019). Fatigue Testing Machines and Apparatus. *Quality Production Improvement*, *10*, 80–108. https://doi.org/10.30657/QPI.2019.10.08

Mallick, P. K. (2021). Thermoplastics and thermoplastic–matrix composites for lightweight automotive structures. *Materials, Design and Manufacturing for Lightweight Vehicles*, 187–228

Mamalis, A. G., Robinson, M., Manolakos, D. E., Demosthenous, G. A., Ioannidis, M. B., & Carruthers, J. (1997). Crashworthy capability of composite material structures. *Composite Structures*, *37*(2), 109–134. https://doi.org/10.1016/S0263-8223(97)80005-0

Middleton, B. (2016). Composites: Manufacture and Application. *Design and Manufacture of Plastic Components for Multifunctionality: Structural Composites, Injection Molding, and 3D Printing*, 53–101. https://doi.org/10.1016/B978-0-323-34061-8.00003-X

Mobasher, B. (2016). Textile Fiber Composites: Testing and Mechanical Behavior. In Textile Fibre Composites in Civil Engineering (pp. 101-150). Elsevier Inc. https://doi.org/10.1016/B978-1-78242-446-8.00006-9

Moore, J. H. (1995). Artificial intelligence programming with LabVIEW: genetic algorithms for instrumentation control and optimization. *Computer Methods and Programs in Biomedicine*, *47*(1), 73–79. https://doi.org/10.1016/0169-2607(95)01630-C

MTS Systems Corporation (2018), Extensometers. https://www.mts.com/-/media/materials/pdfs/brochures/mts-extensometer-catalog.pdf?as=1

New Hampshire Department of Environmental Sciences, Pressure-Treated Wood: Can It Be Used in New Hampshire's Waters, (2019) https://www.des.nh.gov/sites/g/files/ehbemt341/files/documents/2020-01/bb-19.pdf

Olivero, K. A., Barraza, H. J., O'Rear, E. A., & Altan, M. C. (2002). Effect of injection rate and post-fill cure pressure on properties of resin transfer molded disks. *Journal of Composite Materials*, *36*(16), 2011–2028. https://doi.org/10.1177/0021998302036016244

Olivier, P., Cottu, J. P., & Ferret, B. (1995). Effects of cure cycle pressure and voids on some mechanical properties of carbon/epoxy laminates. *Composites*, *26*(7), 509–515. https://doi.org/10.1016/0010-4361(95)96808-J

Ritchie, H., & Roser, M. (2018). Plastic Pollution. Our World in Data. https://ourworldindata.org/plastic-pollution

Sadik, W. A., El-Demerdash, A. G. M., Abokhateeb, A. E. A., & Elessawy, N. A. (2021). Innovative high-density polyethylene/waste glass powder composite with remarkable mechanical, thermal and recyclable properties for technical applications. In *Heliyon* Vol. 7, Issue 4 https://doi.org/10.1016/j.heliyon.2021.e06627

Sepe, M. (2011). *The Strain Rate Effect | Plastics Technology*. https://www.ptonline.com/articles/the-strain-rate-effect

United States Environmental Protection Agency, Facts and Figures about Materials, Waste and Recycling. https://www.epa.gov/facts-and-figures-about-materials-waste-and-recycling/plastics-material-specific-data

Werner, J., Aneziris, C. G., & Schafföner, S. (2014). Influence of porosity on Young′s modulus of carbon-bonded alumina from room temperature up to 1450°C. *Ceramics International*, *9 Part A*(40), 14439–14445. https://doi.org/10.1016/J.CERAMINT.2014.07.013

Y. Yang, X. Chen, N. Lu, F. Gao (2016), Injection Molding Process Control, Monitoring, and Optimization, ISBN 10:1569905924

Zhang, L., Gao, K., Elias, A., Dong, Z., & Chen, W. (2014). Porosity dependence of elastic modulus of porous Cr3C2 ceramics. *Ceramics International*, *40*(1), 191–198. https://doi.org/10.1016/J.CERAMINT.2013.05.122

APPENDIX A

SAMPLE RESULTS AND PHOTOS

Sample A2

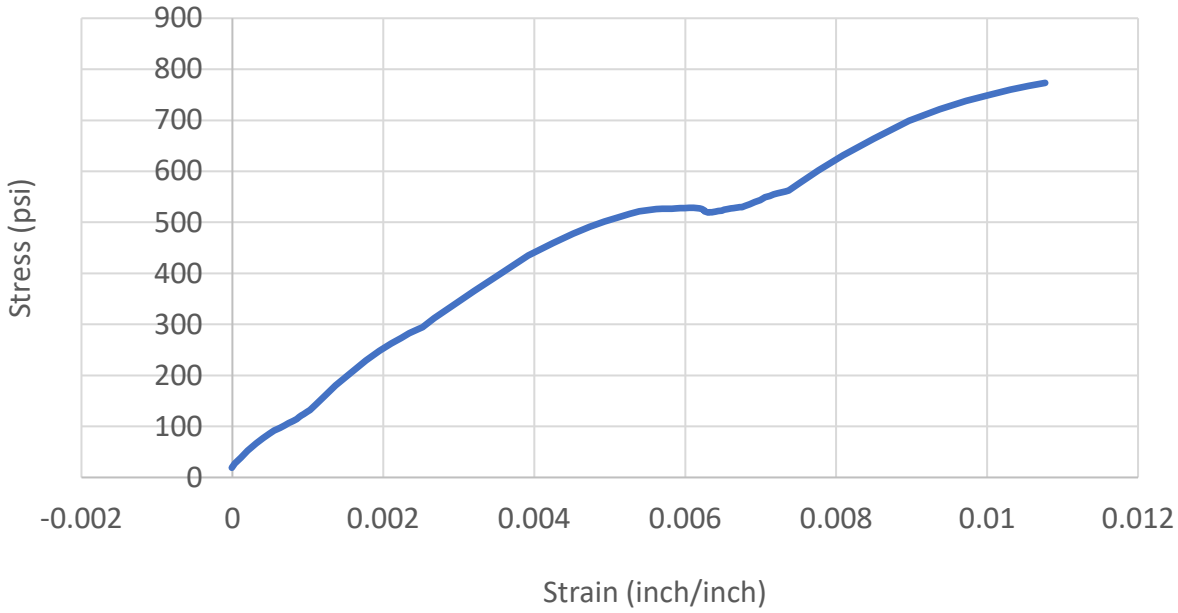

Figure 41. Stress-Strain Curve of Sample A2

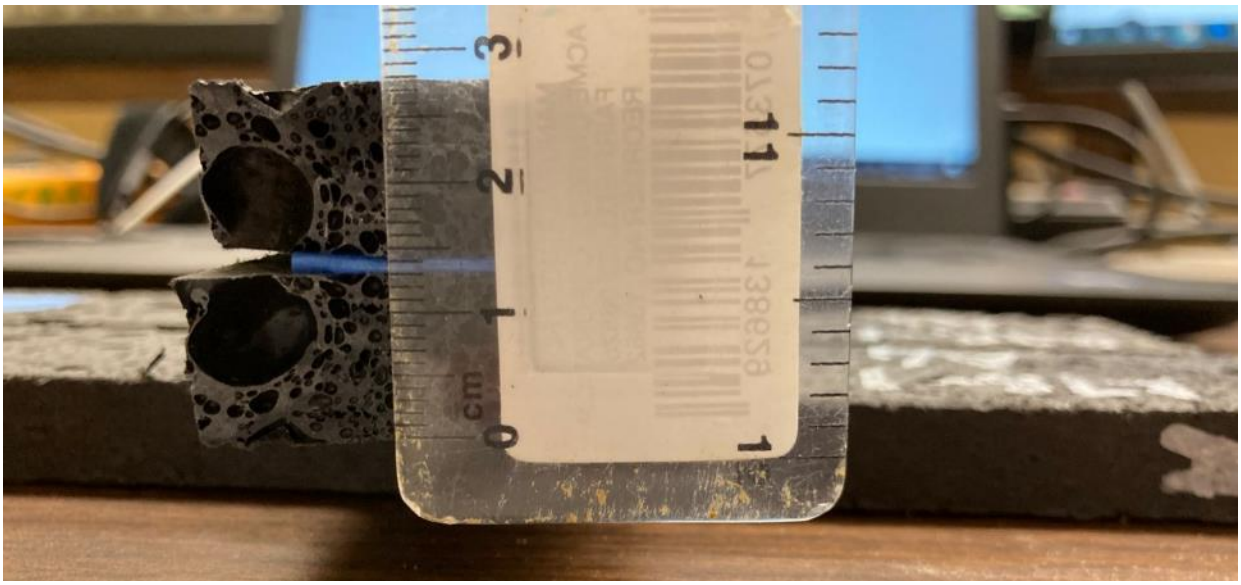

Figure 42. Detailed View of Damaged Area of Sample A2

Sample A3

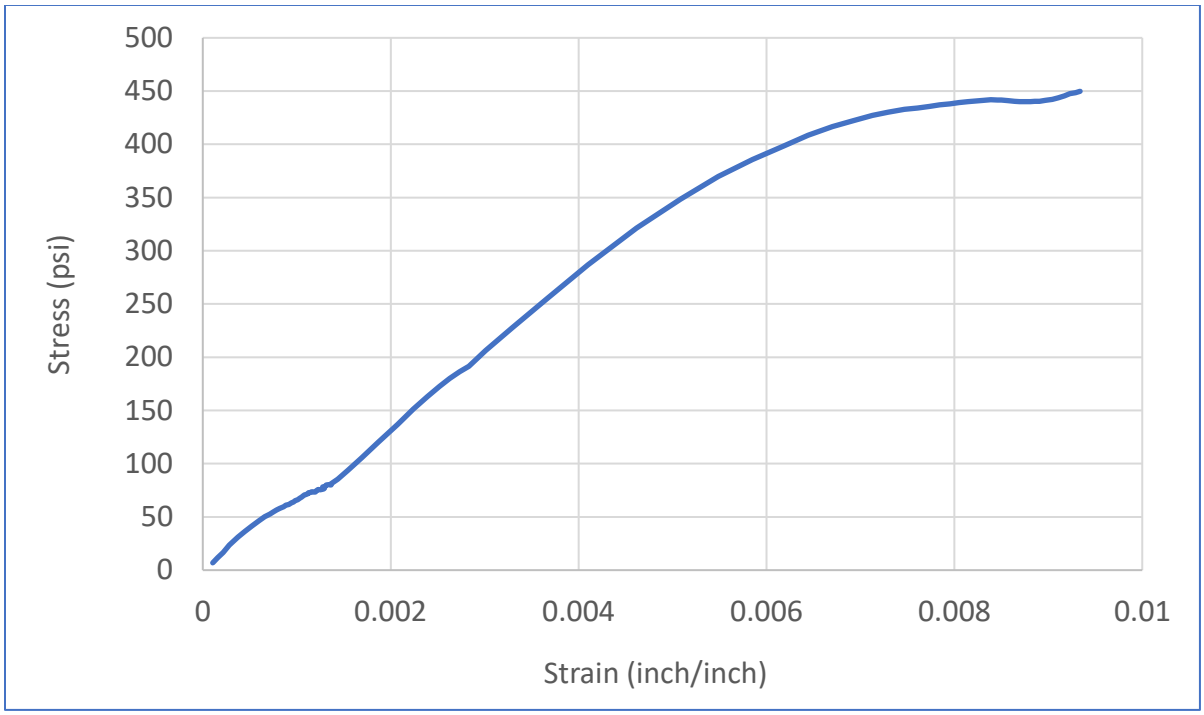

Figure 43. Stress-Strain Curve of Sample A3

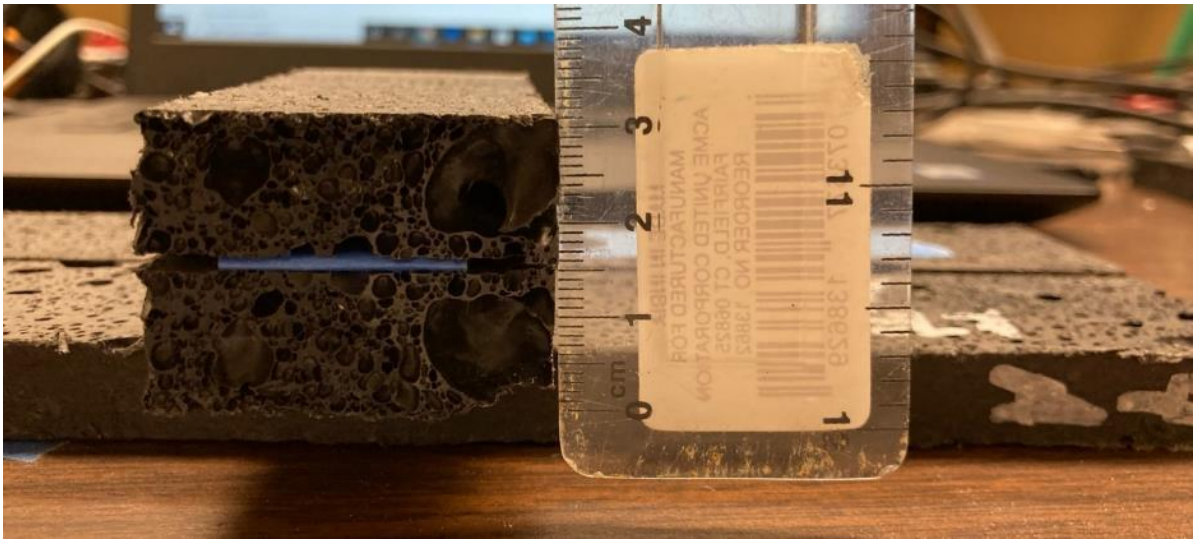

Figure 44. Detailed View of Damaged Area of Sample A3

Sample A4

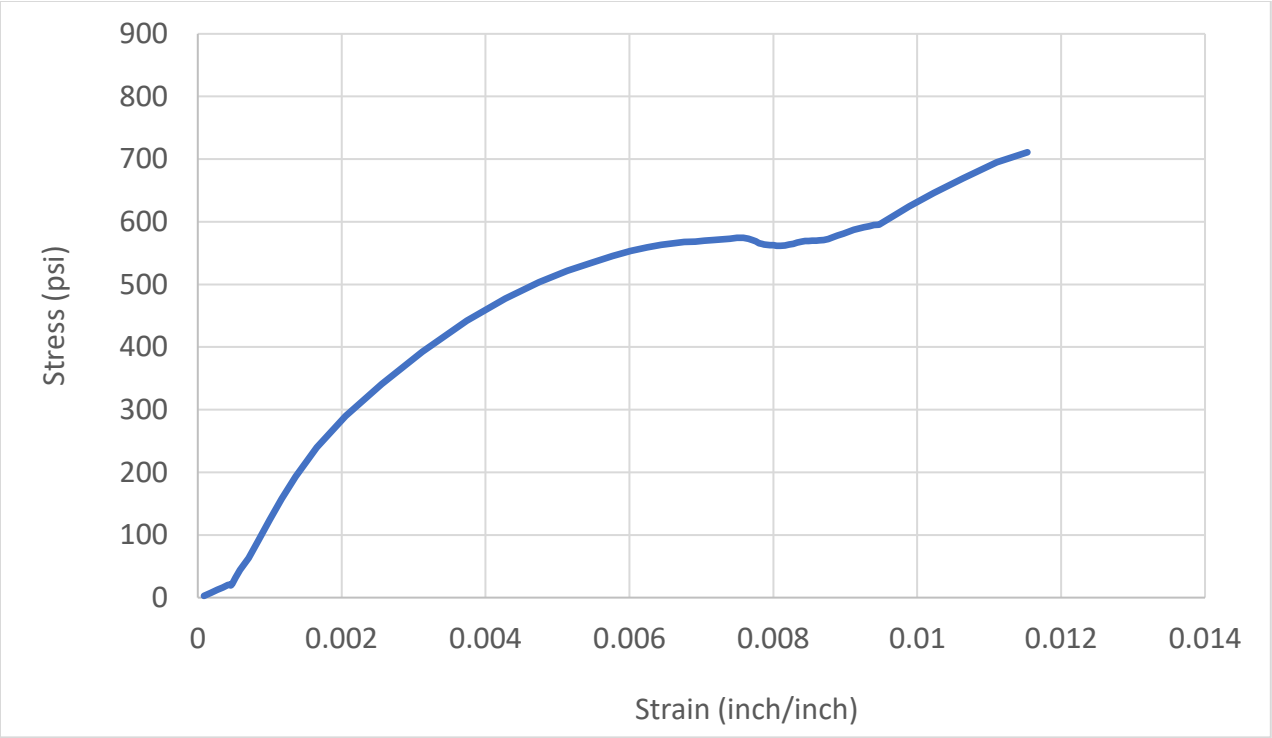

Figure 45. Stress-Strain Curve of Sample A4

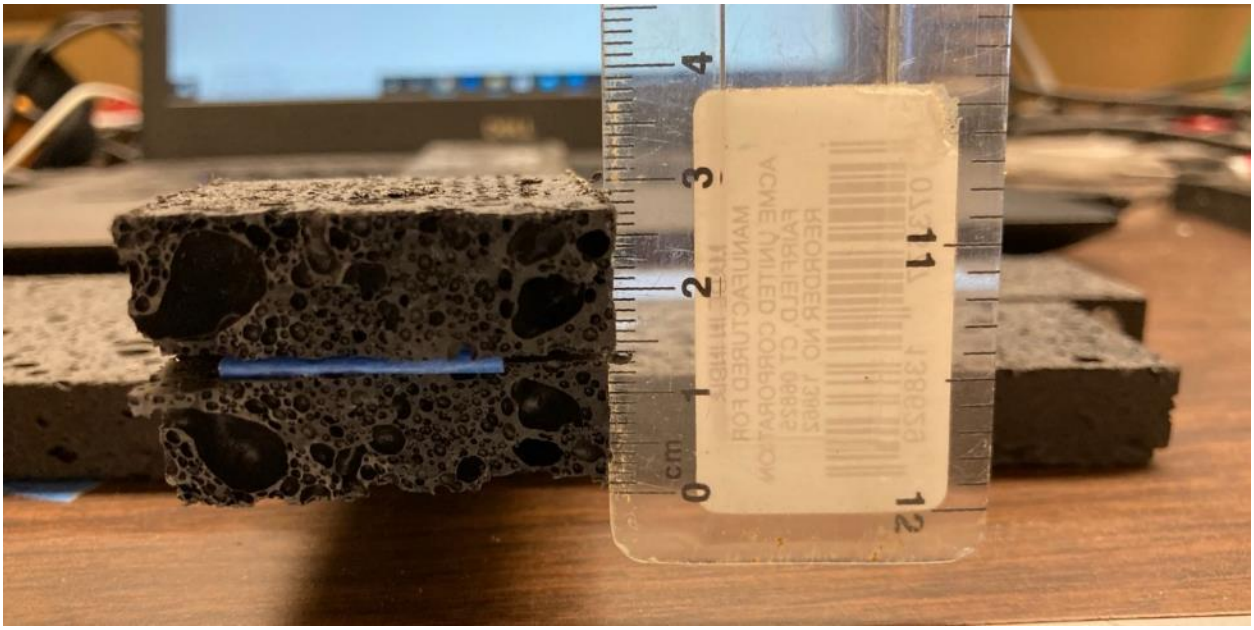

Figure 46. Detailed View of Damaged Area of Sample A4

Sample B2

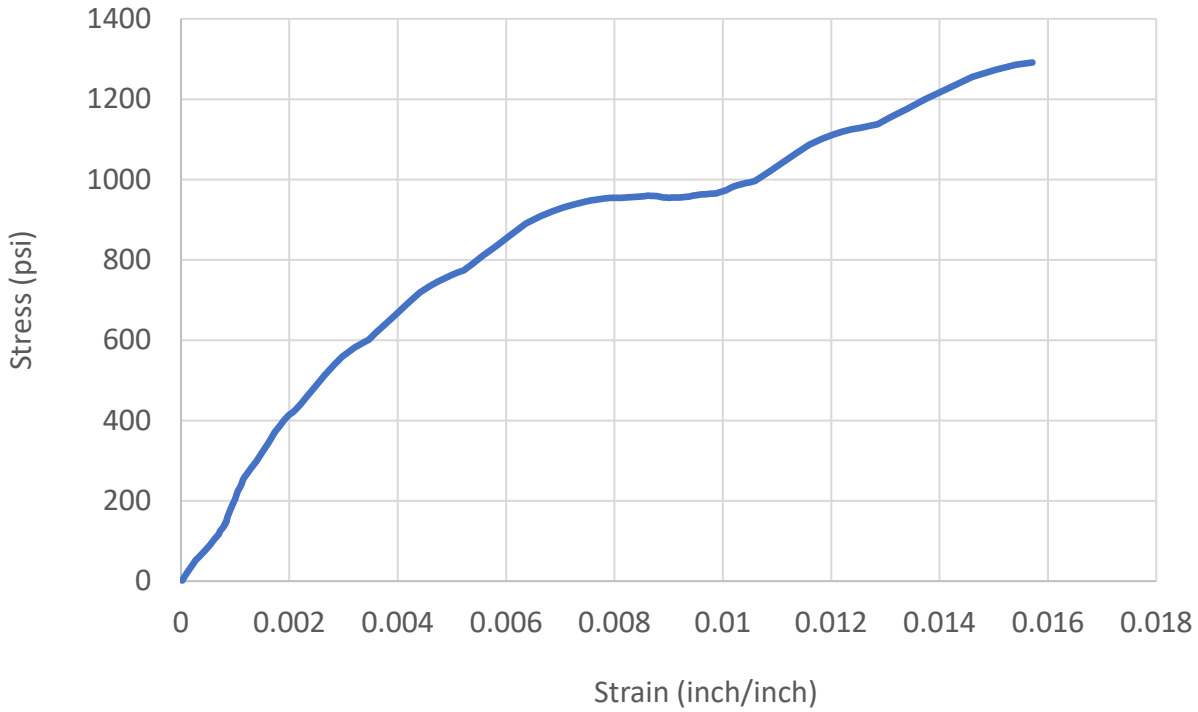

Figure 47. Stress-Strain Curve of Sample B2

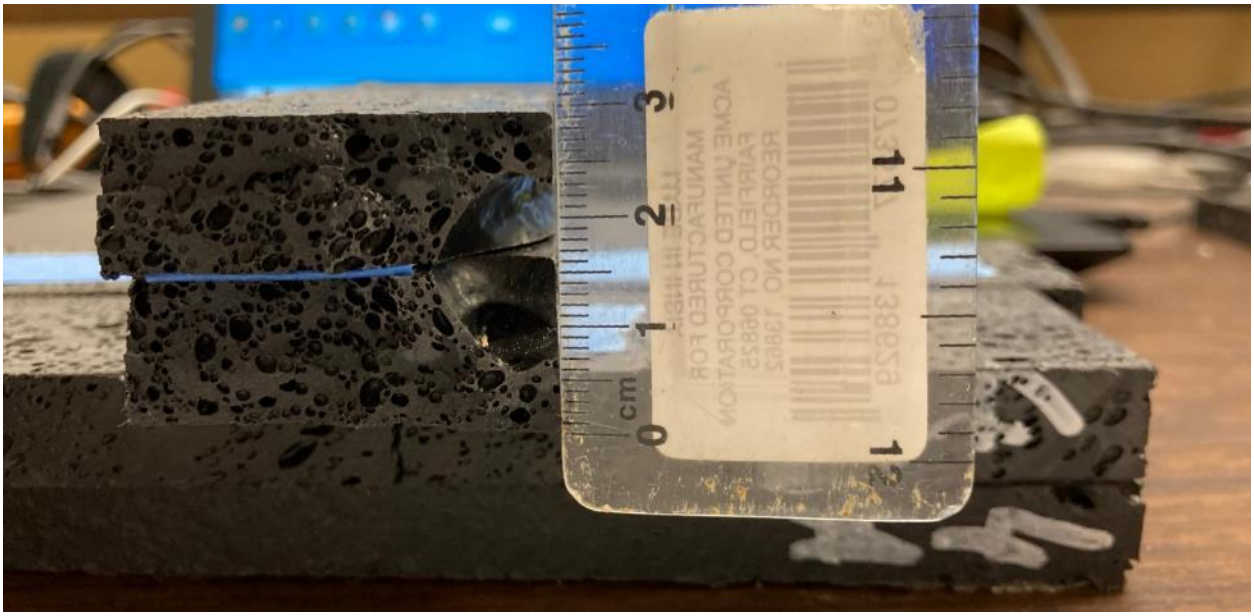

Figure 48. Detailed View of Damaged Area of Sample B2

Sample B4

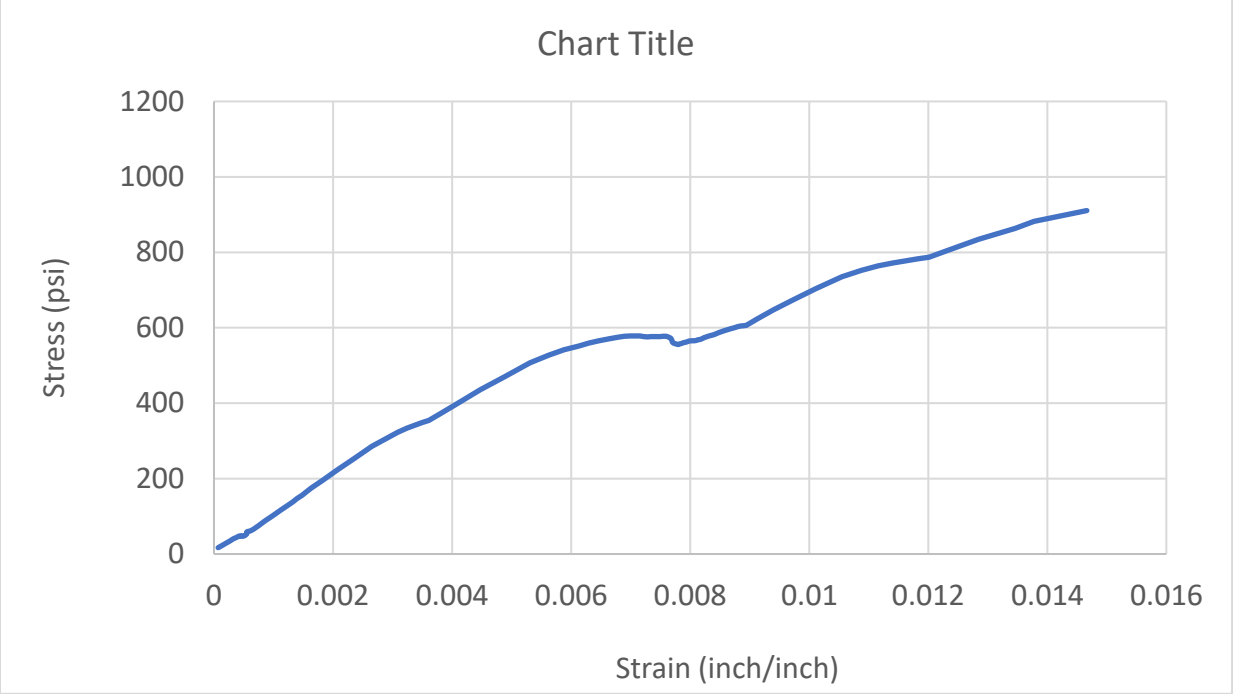

Figure 49. Stress-Strain Curve of Sample B4

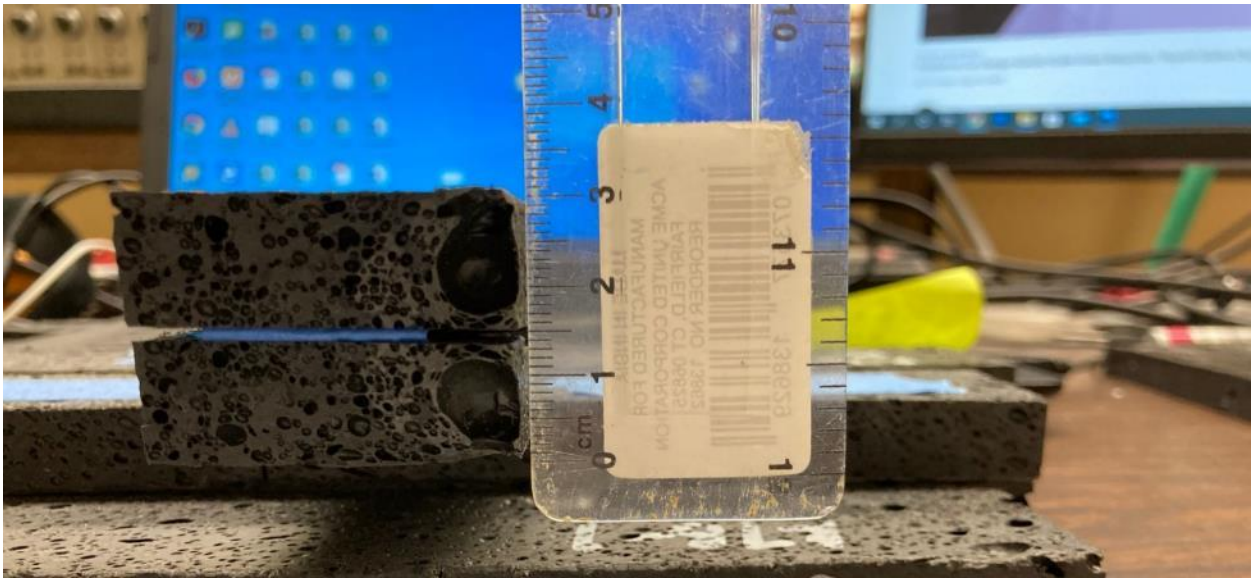

Figure 50. Detailed View of Damaged Area of Sample B4

Sample B5

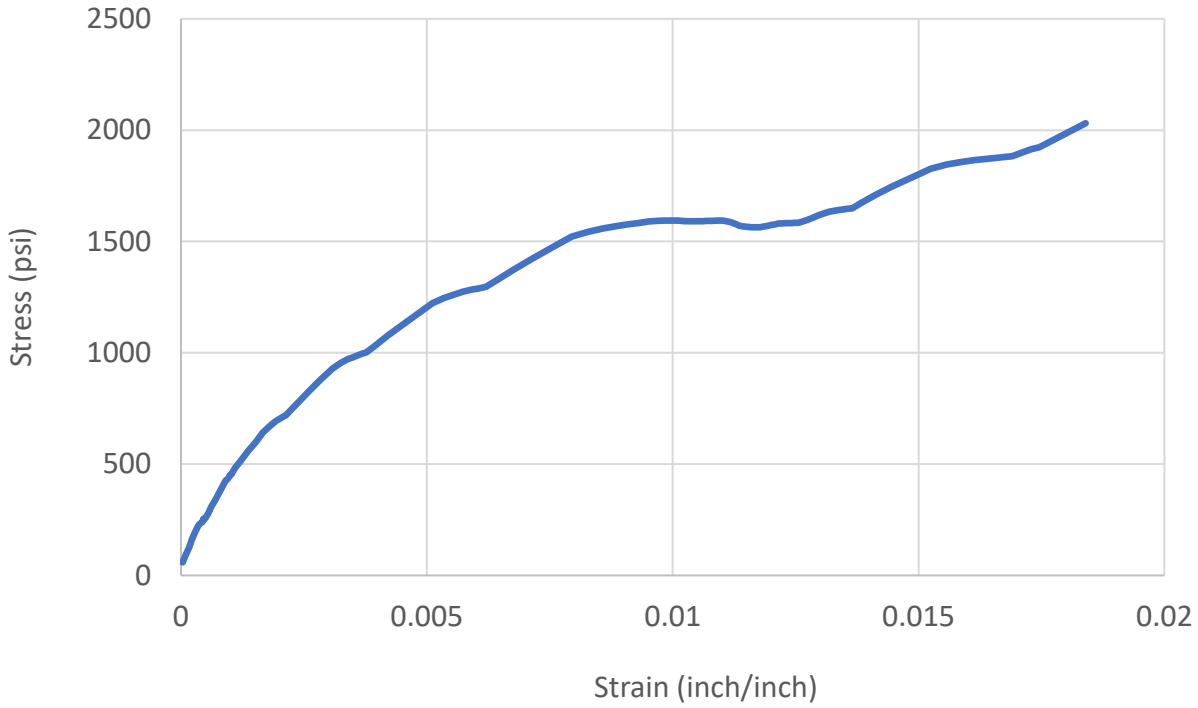

Figure 51. Stress-Strain Curve of Sample B5

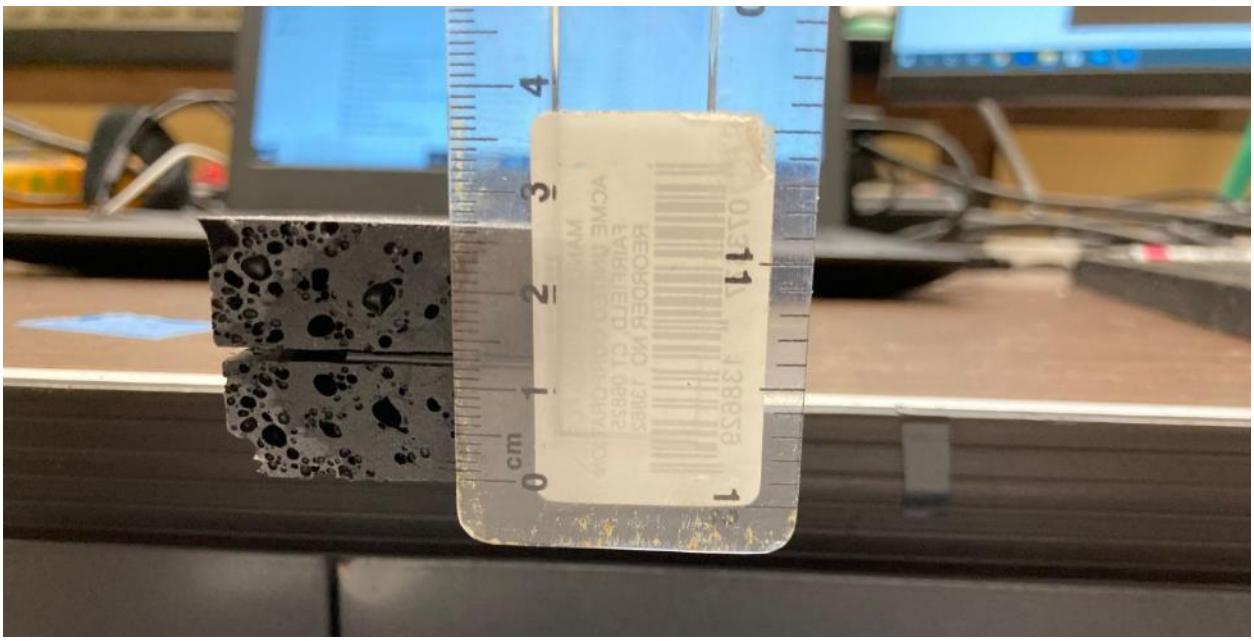

Figure 52. Detailed View of Damaged Area of Sample B5

Sample C2

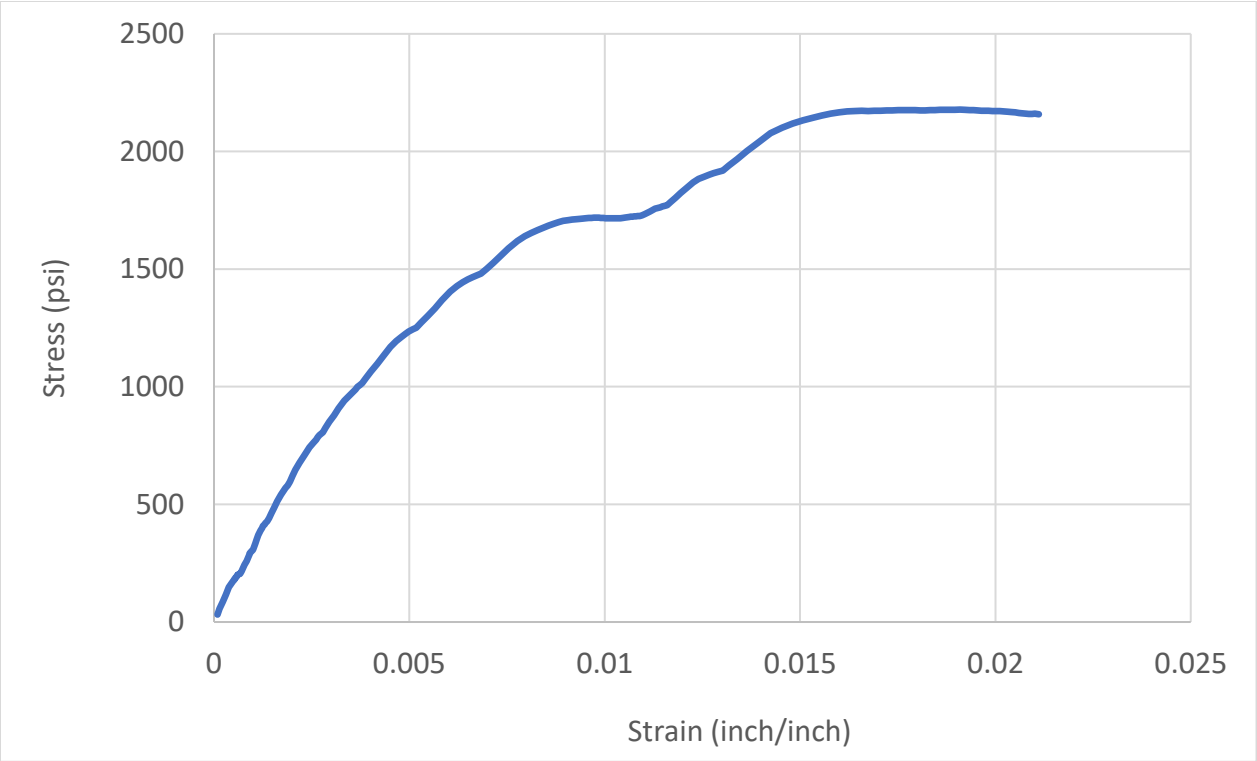

Figure 53. Stress-Strain Curve of Sample C2

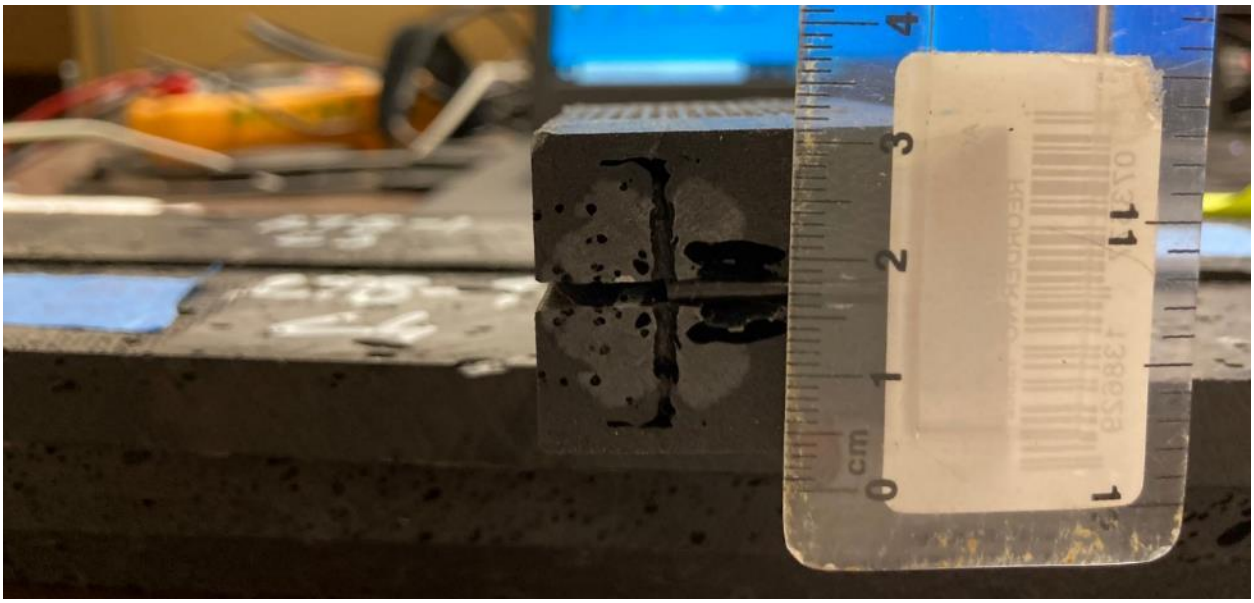

Figure 54. Detailed View of Damaged Area of Sample C2

Sample C3

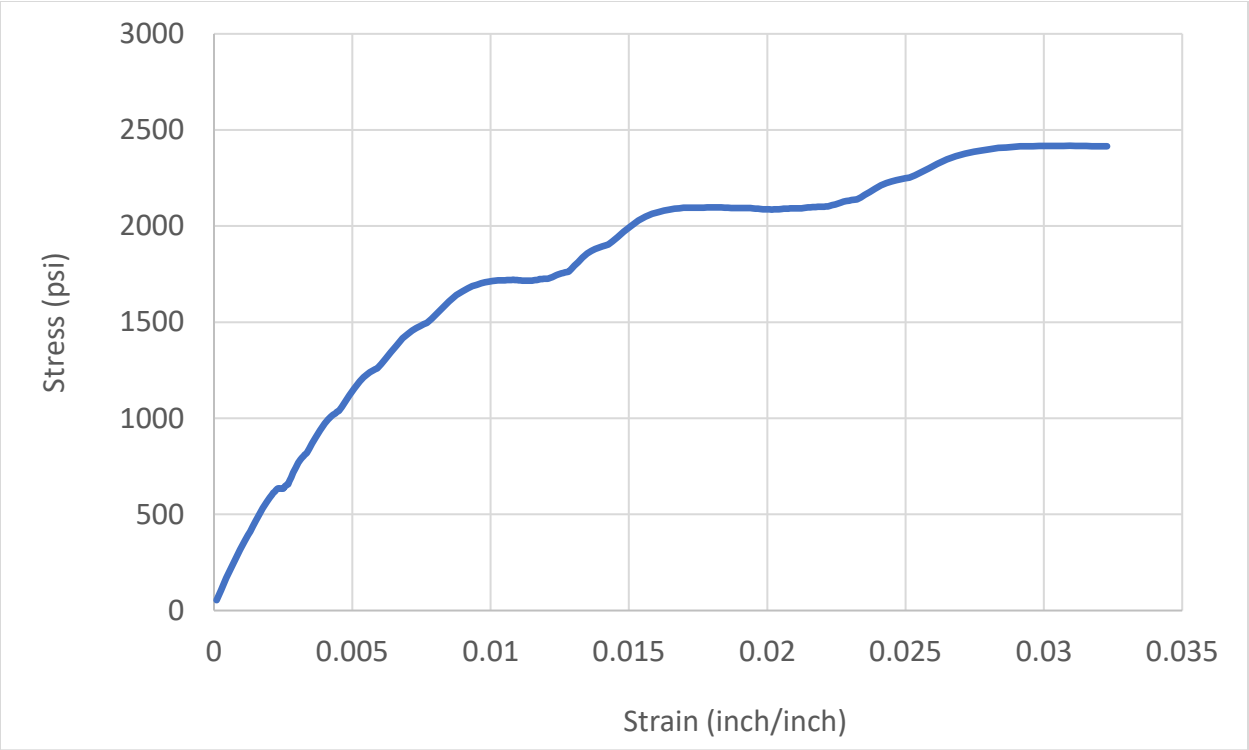

Figure 55. Stress-Strain Curve of Sample C3

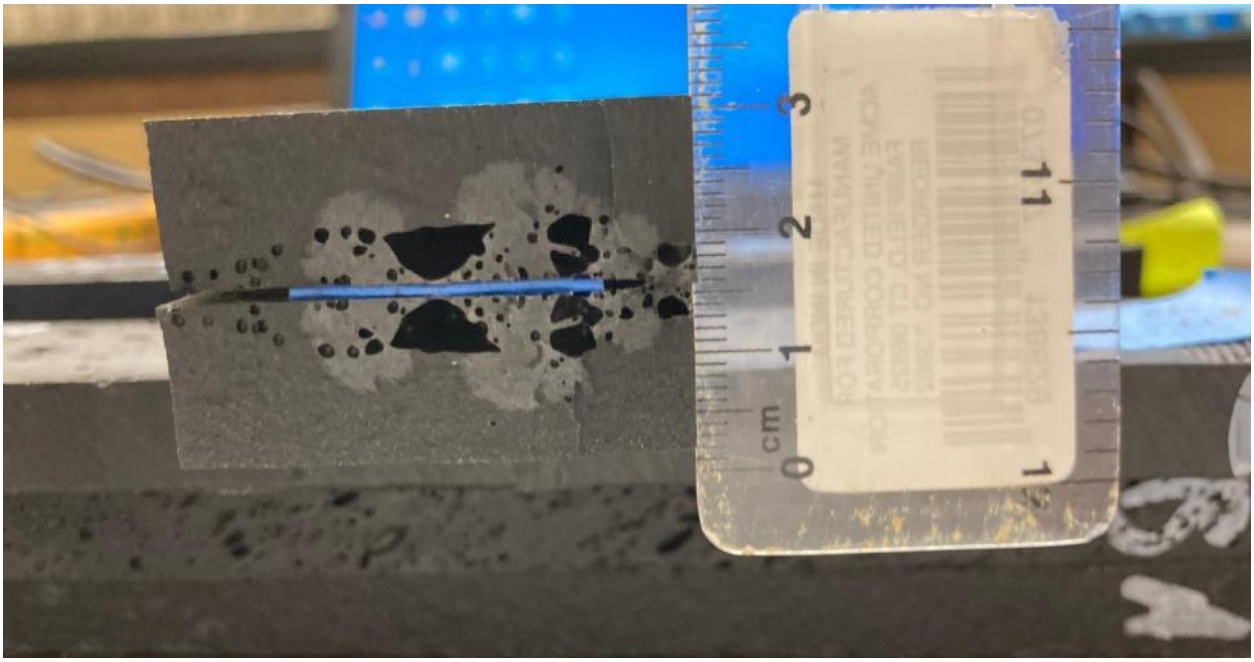

Figure 56. Detailed View of Damaged Area of Sample C3

Sample C4

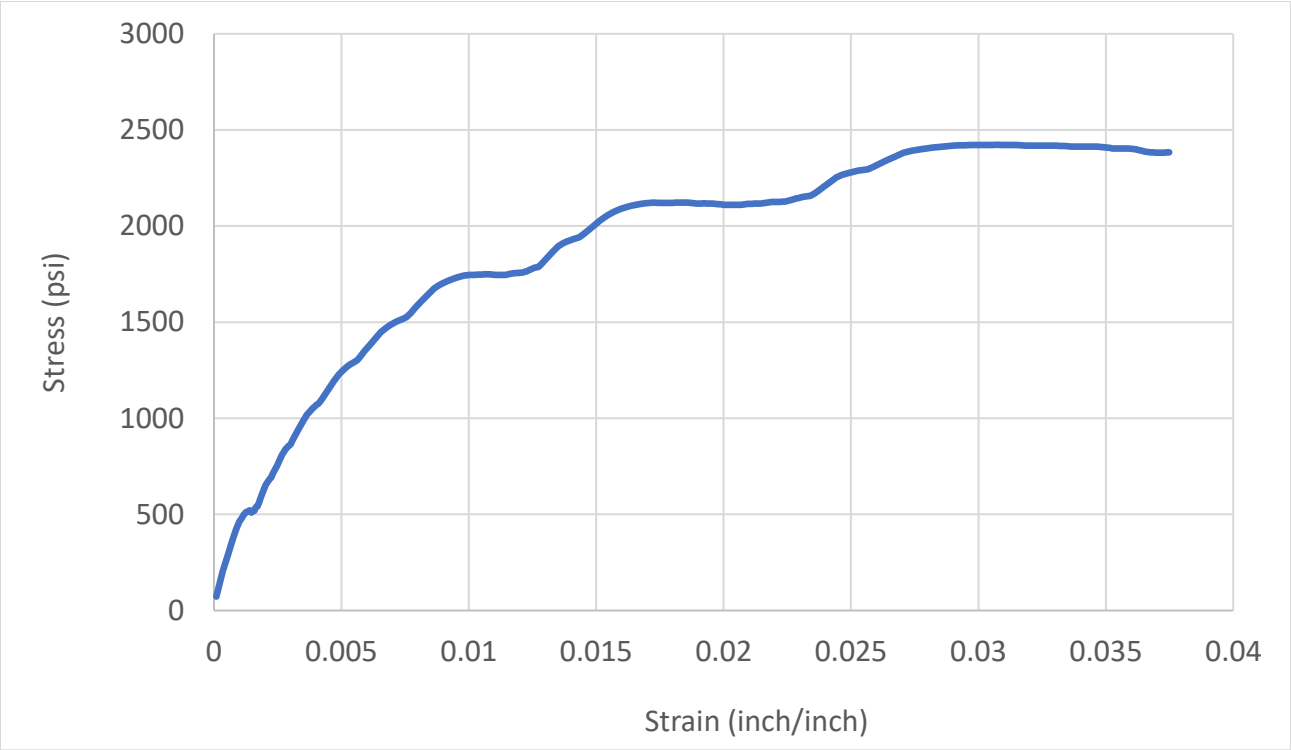

Figure 57. Stress-Strain Curve of Sample C4

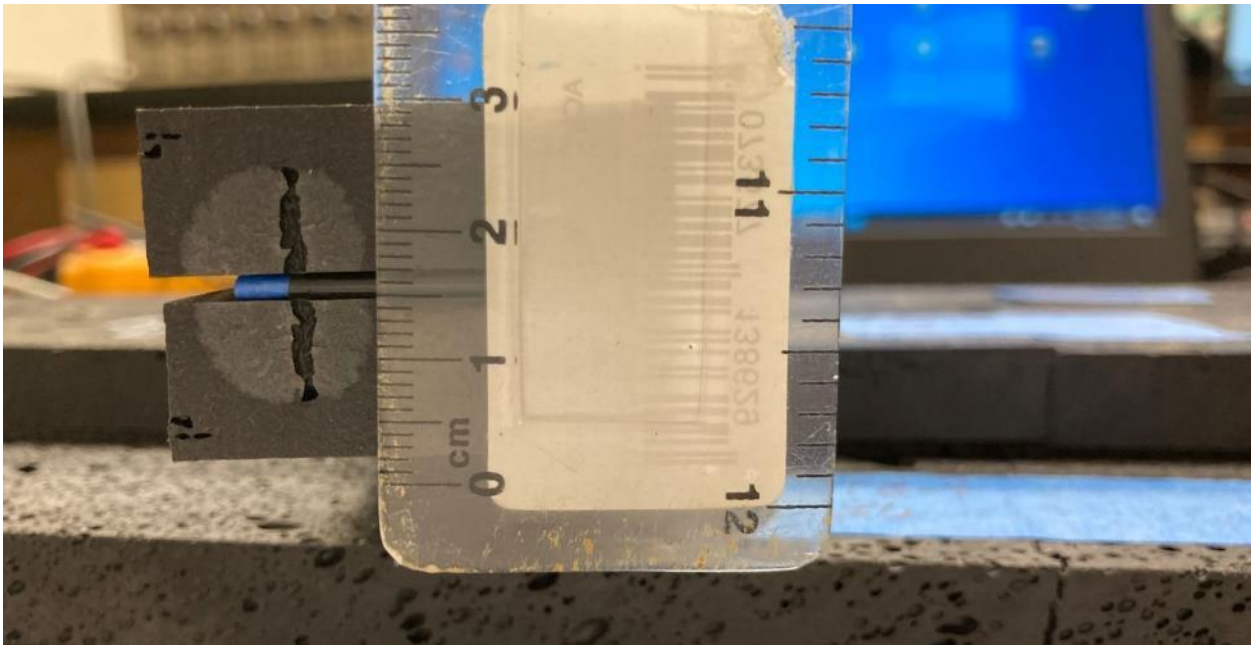

Figure 58. Detailed View of Damaged Area of Sample C4

Sample A1_2

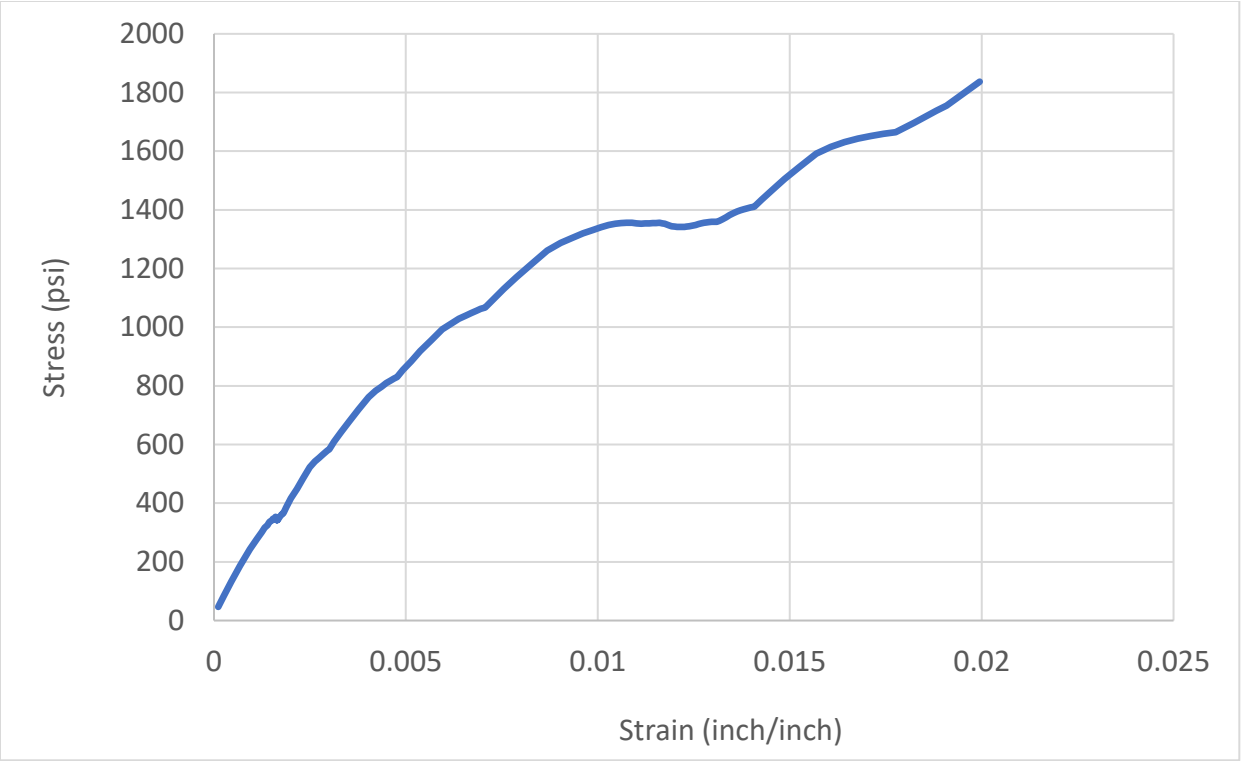

Figure 59. Stress-Strain Curve of Sample A1_2

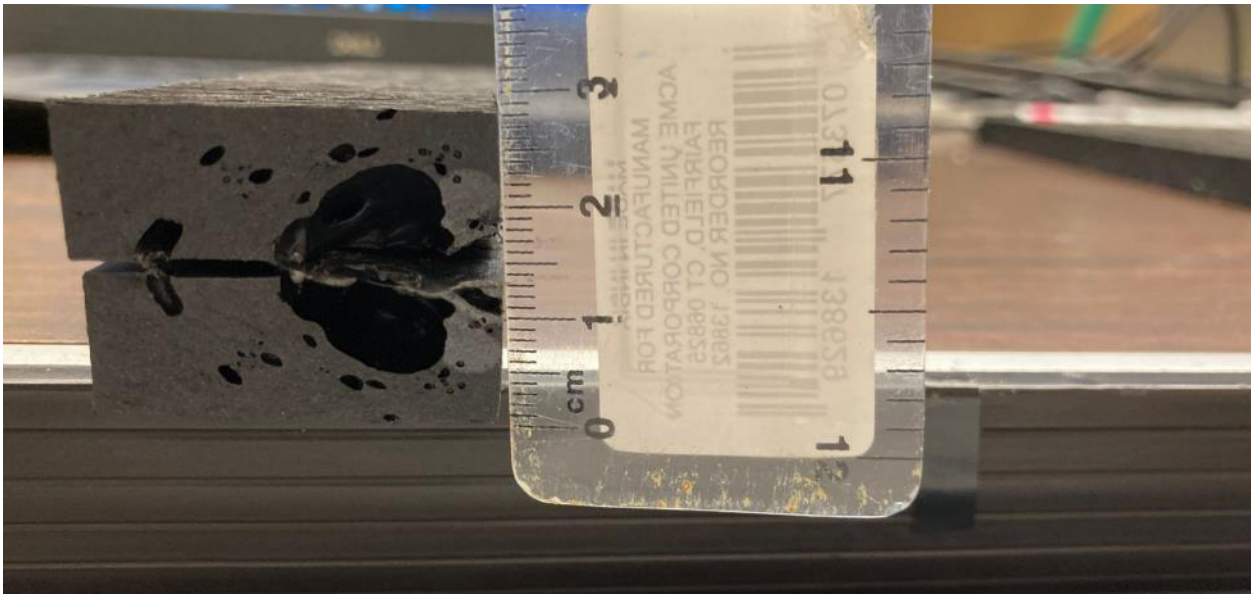

Figure 60. Detailed View of Damaged Area of Sample A1_2

Sample A2_2

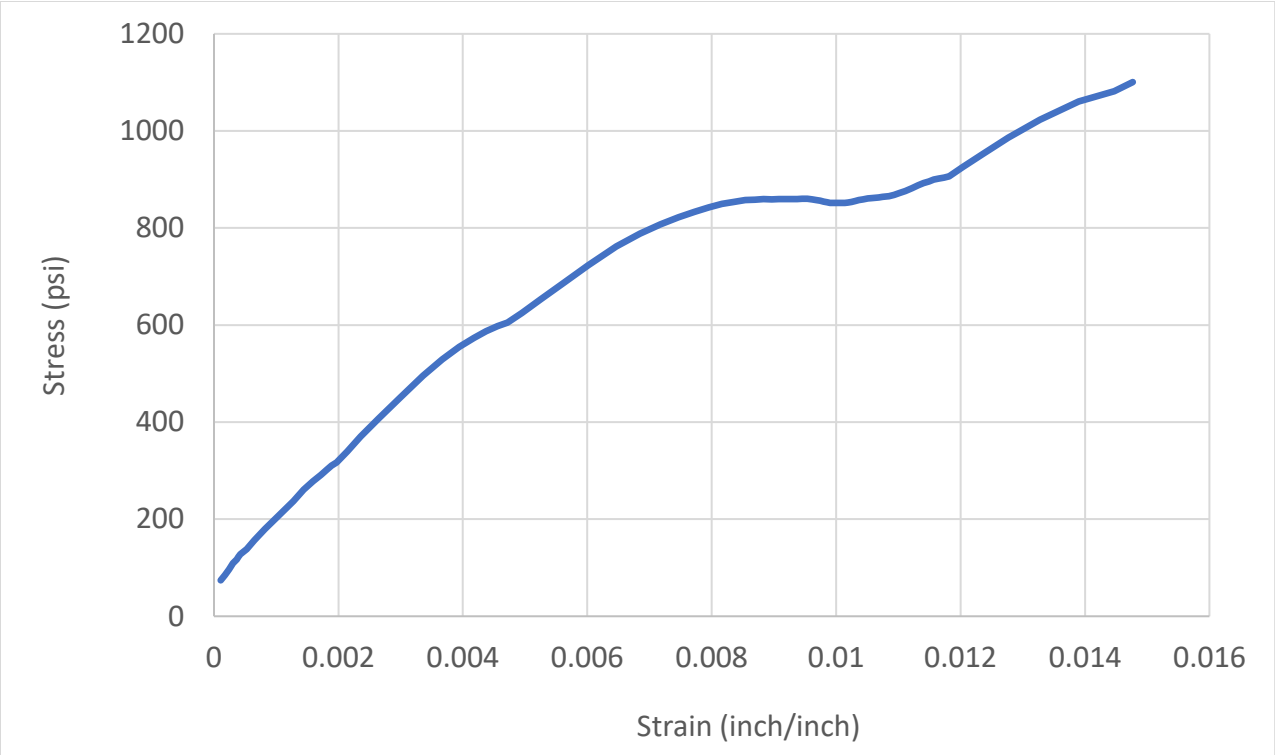

Figure 61. Stress-Strain Curve of Sample A2_2

Figure 62. Detailed View of Damaged Area of Sample A2_2

Sample A3_2

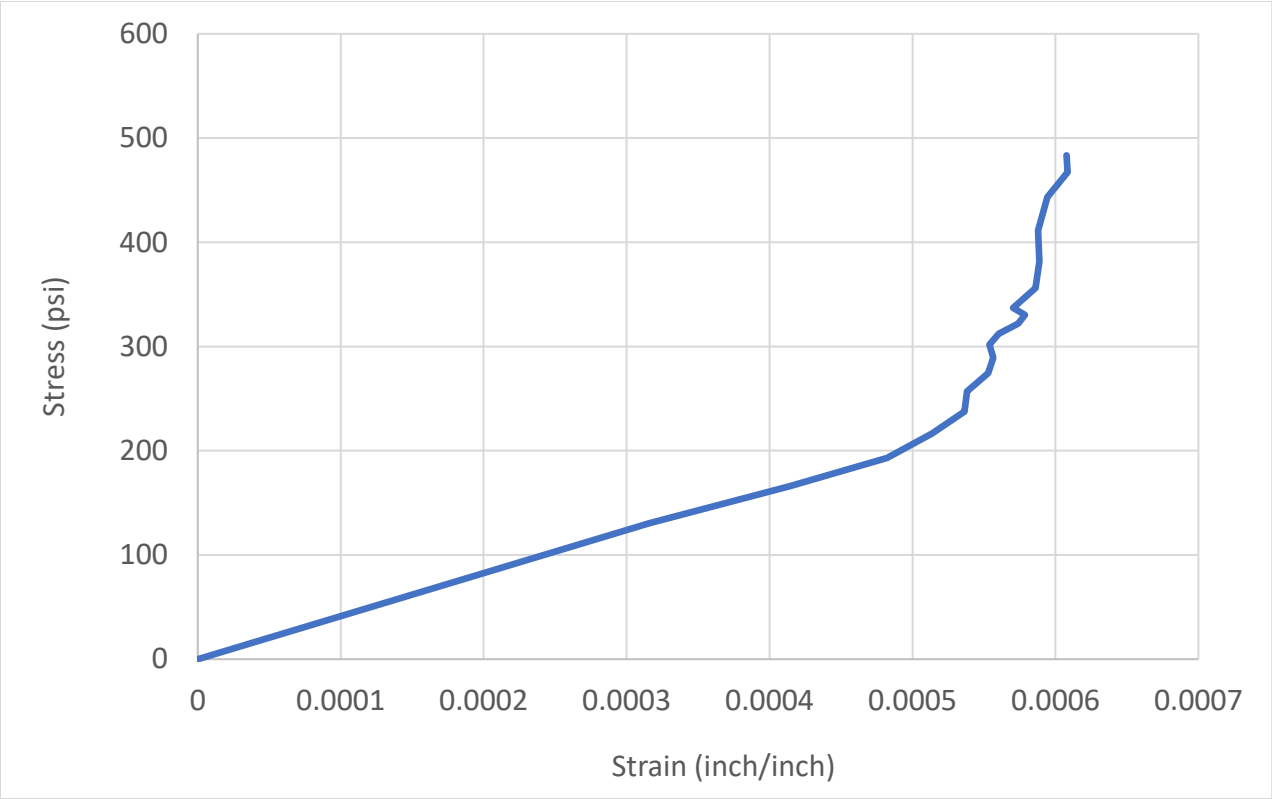

Figure 63. Stress-Strain Curve of Sample A3_2

Figure 64. Detailed View of Damaged Area of Sample A3_2

Sample A4_2

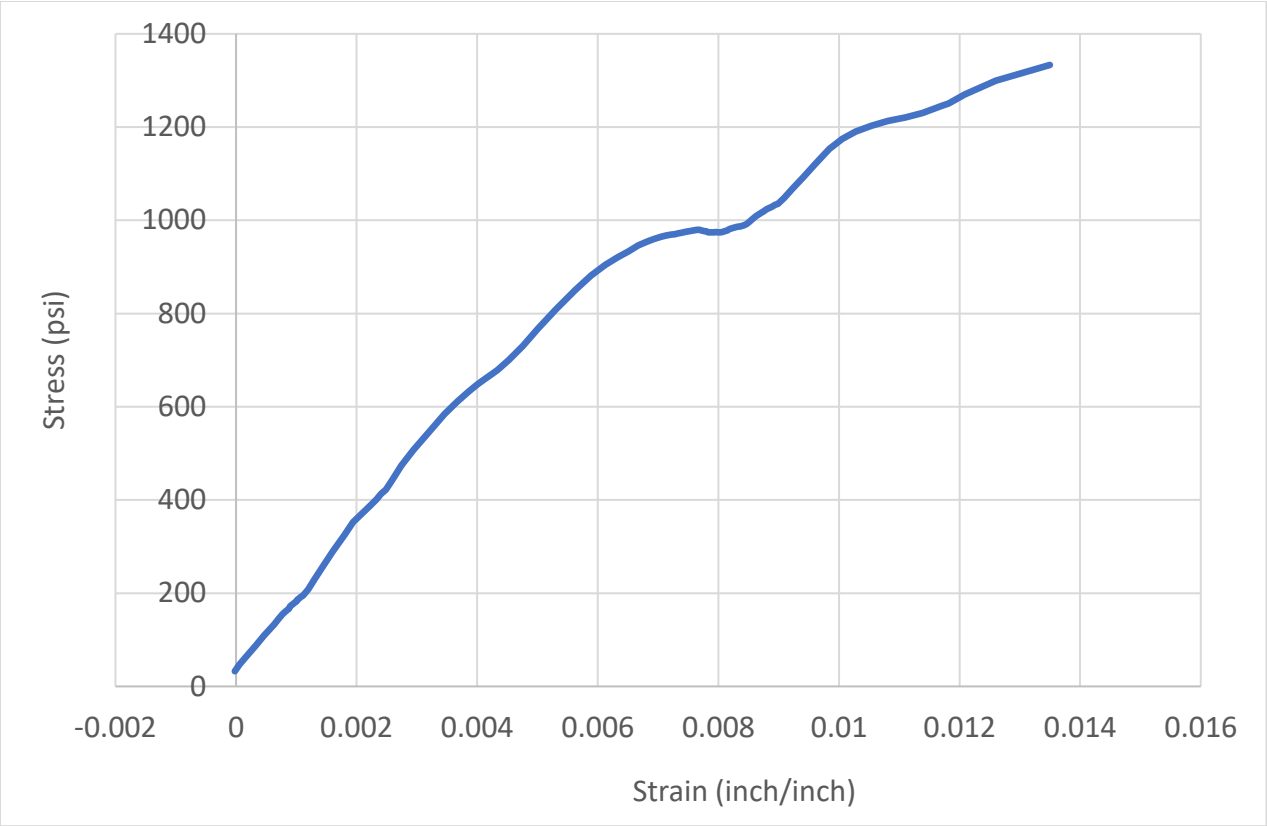

Figure 65. Stress-Strain Curve of Sample A4_2

Figure 66. Detailed View of Damaged Area of Sample A4_2

Sample A5_2

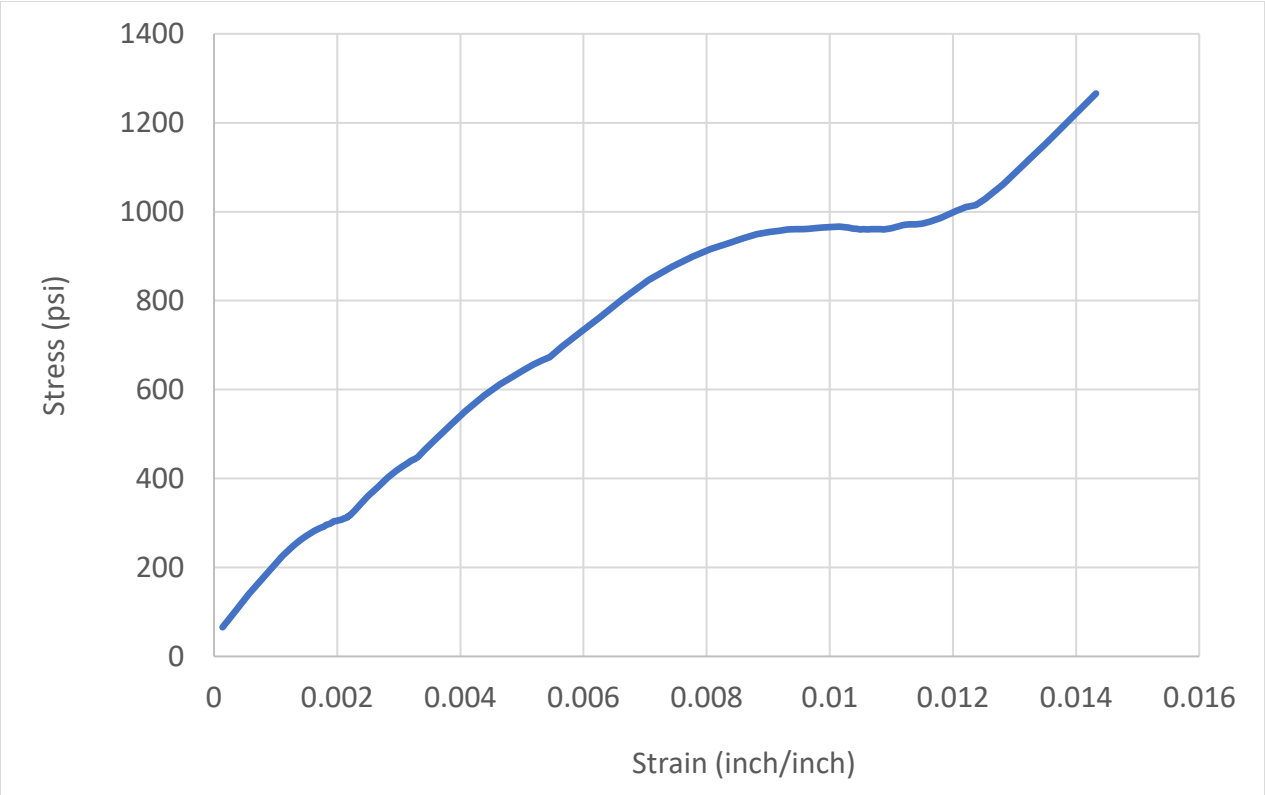

Figure 67. Stress-Strain Curve of Sample A5_2

Figure 68. Detailed View of Damaged Area of Sample A5_2

Sample B1_2

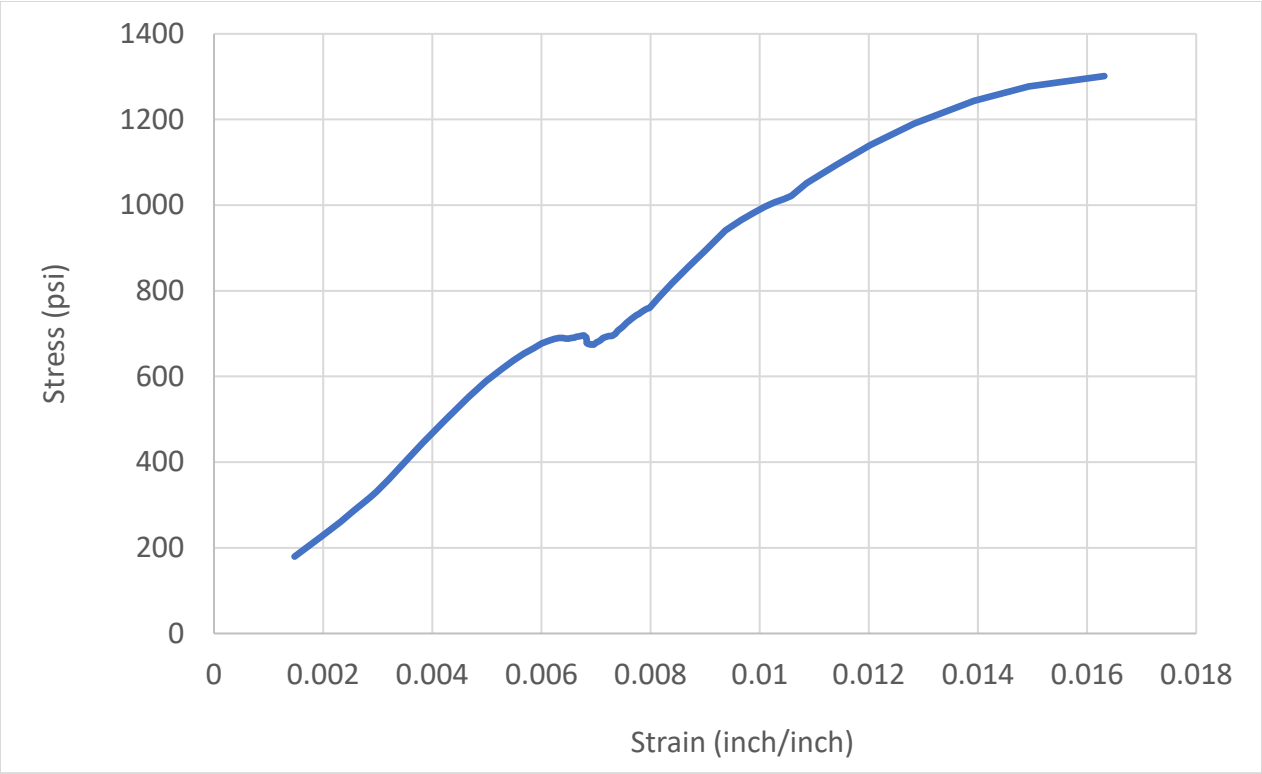

Figure 69. Stress-Strain Curve of Sample B1_2

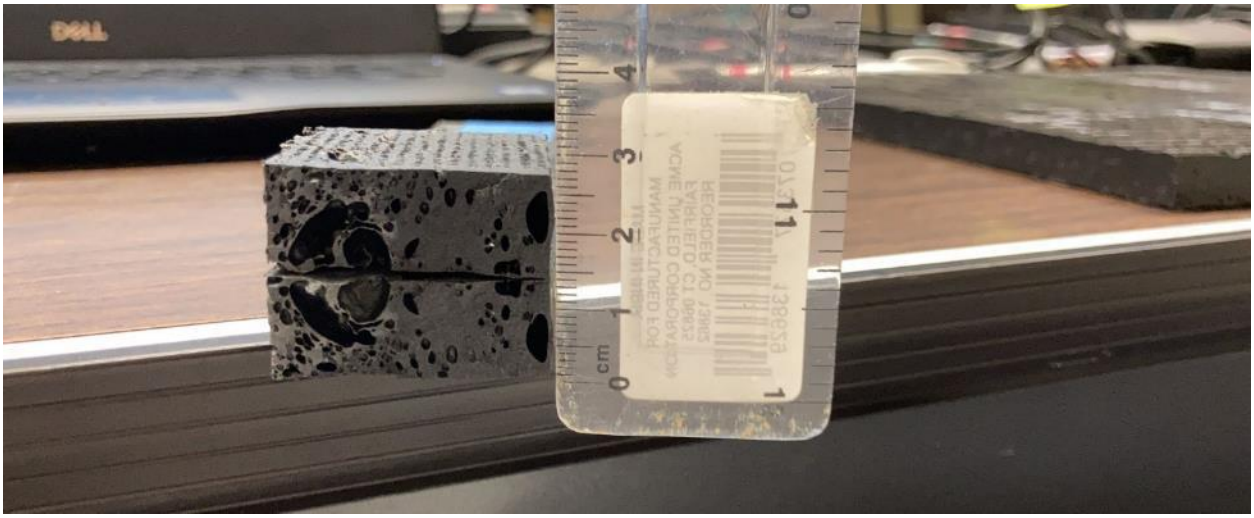

Figure 70. Detailed View of Damaged Area of Sample B1_2

Sample B2_2

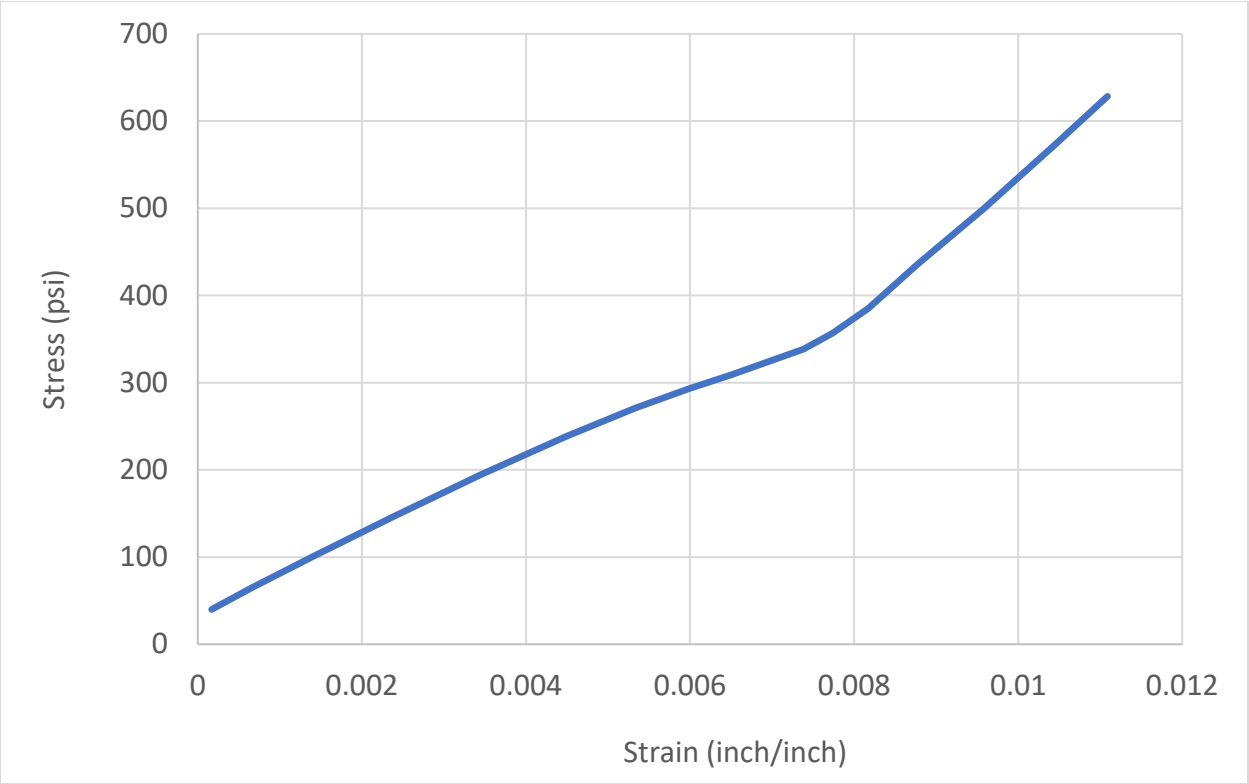

Figure 71. Stress-Strain Curve of Sample B2_2

Figure 72. Detailed View of Damaged Area of Sample B2_2

Sample B3_2

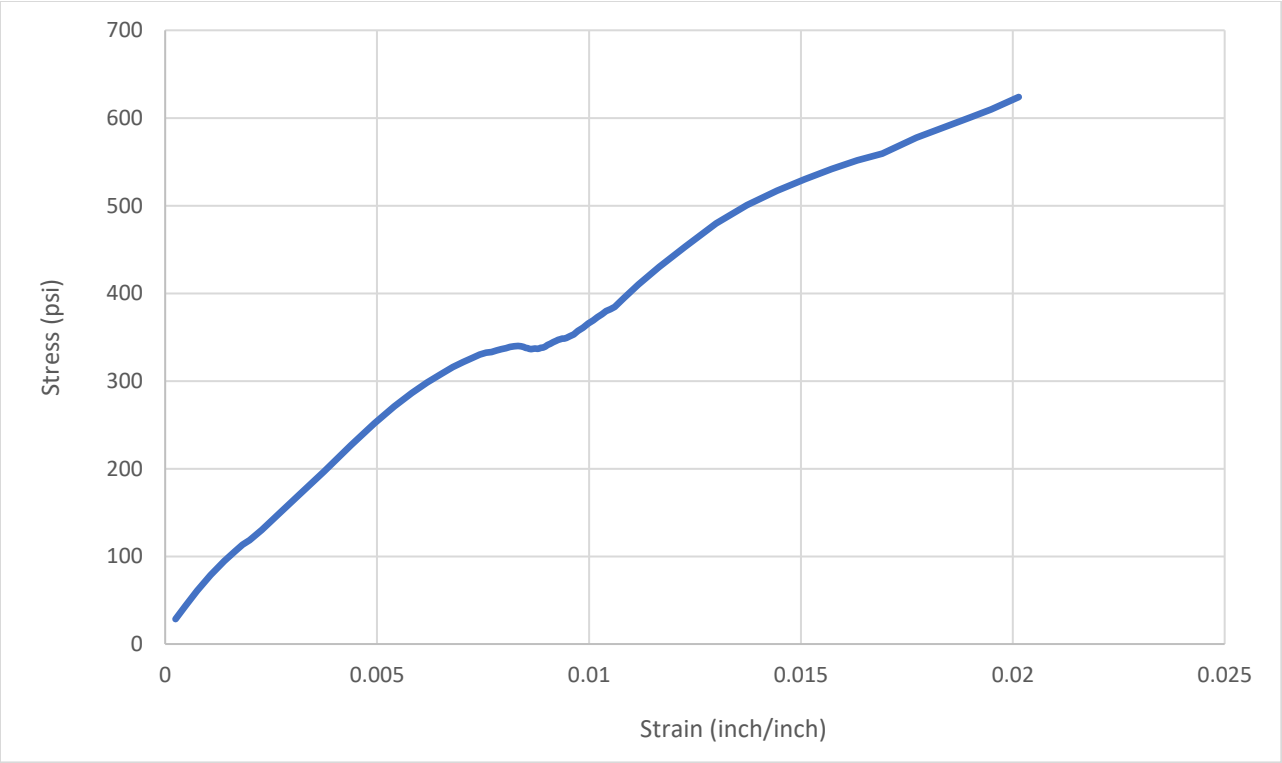

Figure 73. Stress-Strain Curve of Sample B3_2

Figure 74. Detailed View of Damaged Area of Sample B3_2

Sample B4_2

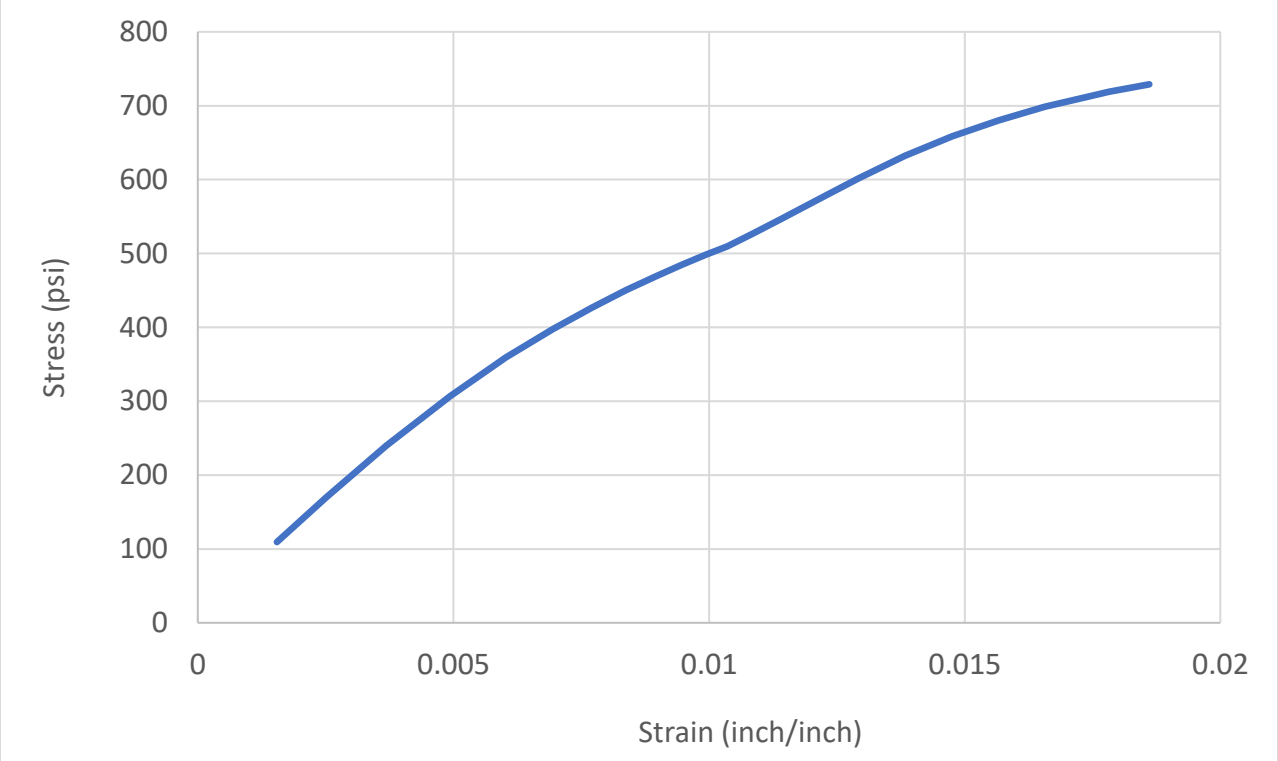

Figure 75. Stress-Strain Curve of Sample B4_2

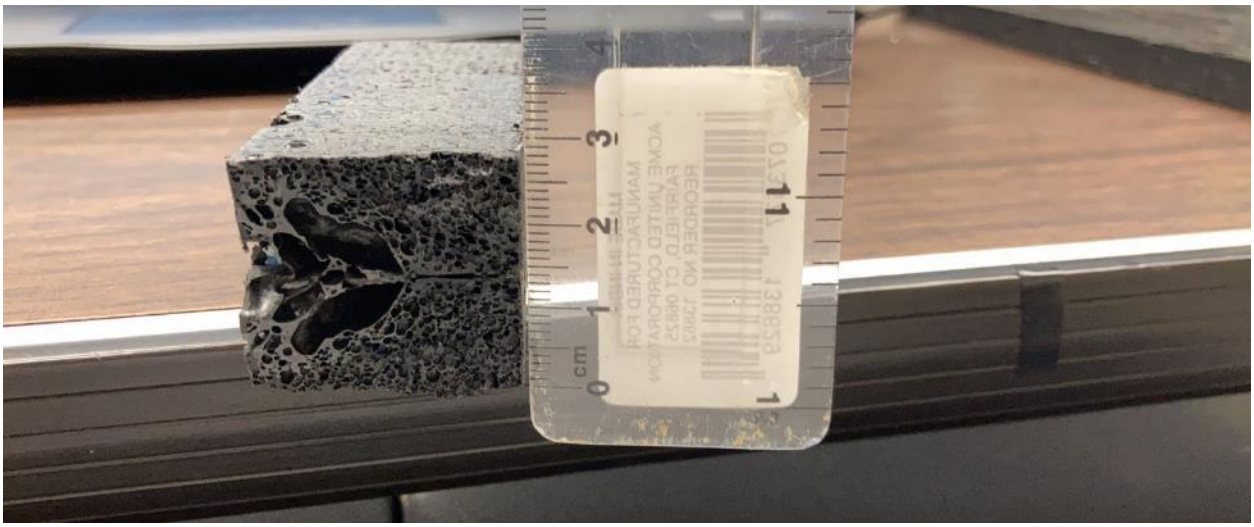

Figure 76. Detailed View of Damaged Area of Sample B4_2

Sample B5_2

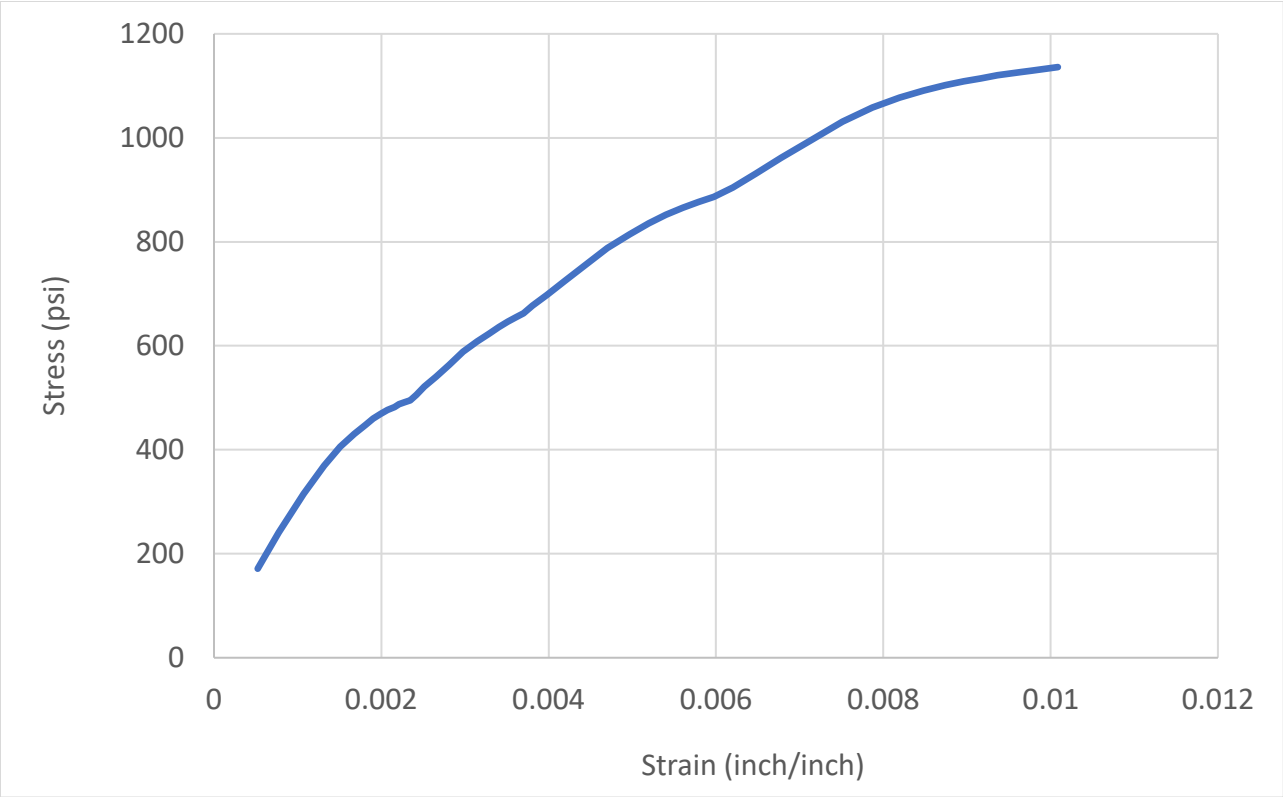

Figure 77. Stress-Strain Curve of Sample B5_2

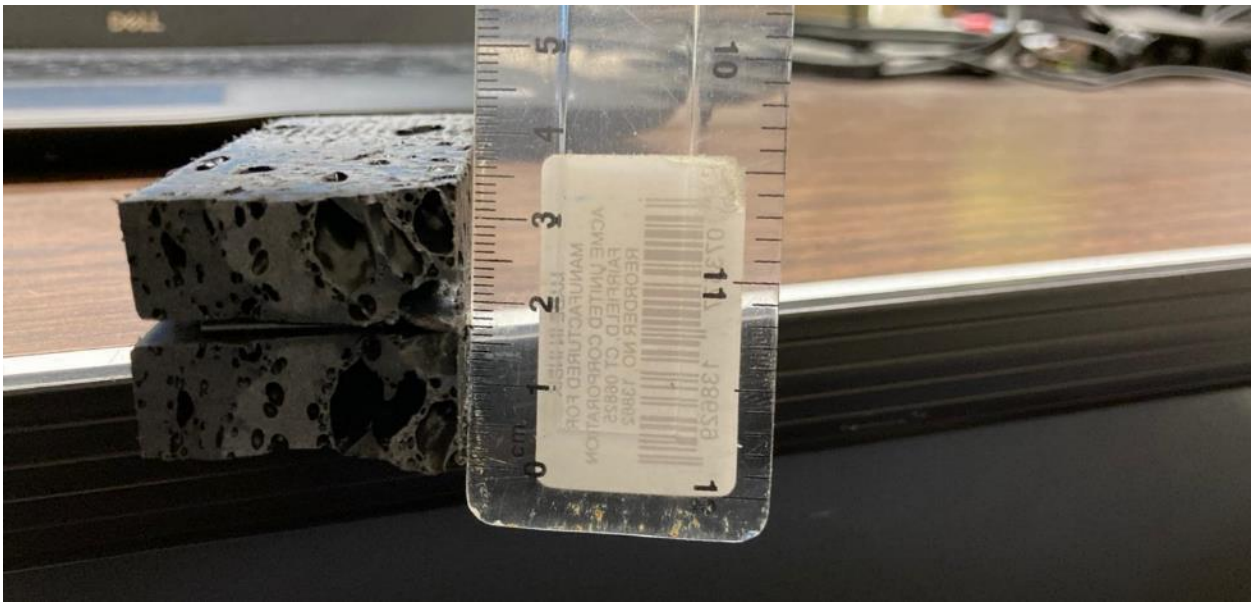

Figure 78. Detailed View of Damaged Area of Sample B5_2

Sample C1_2

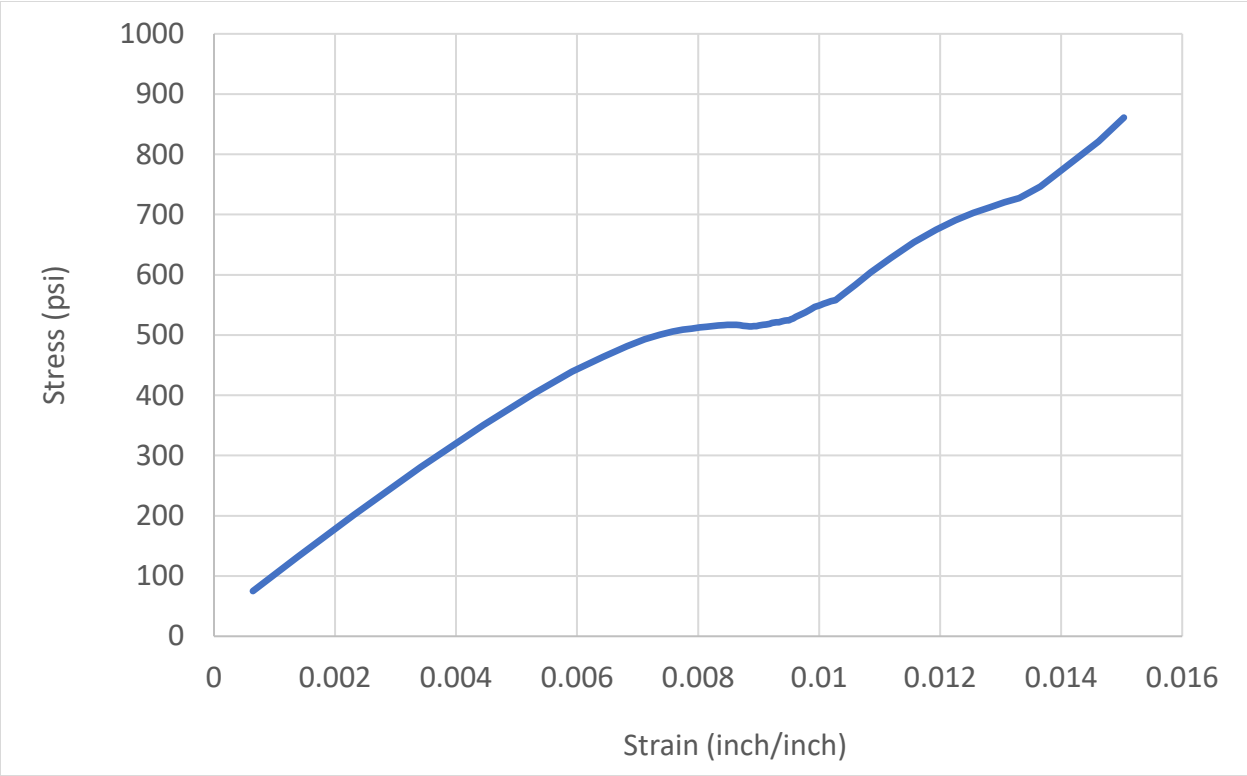

Figure 79. Stress-Strain Curve of Sample C1_2

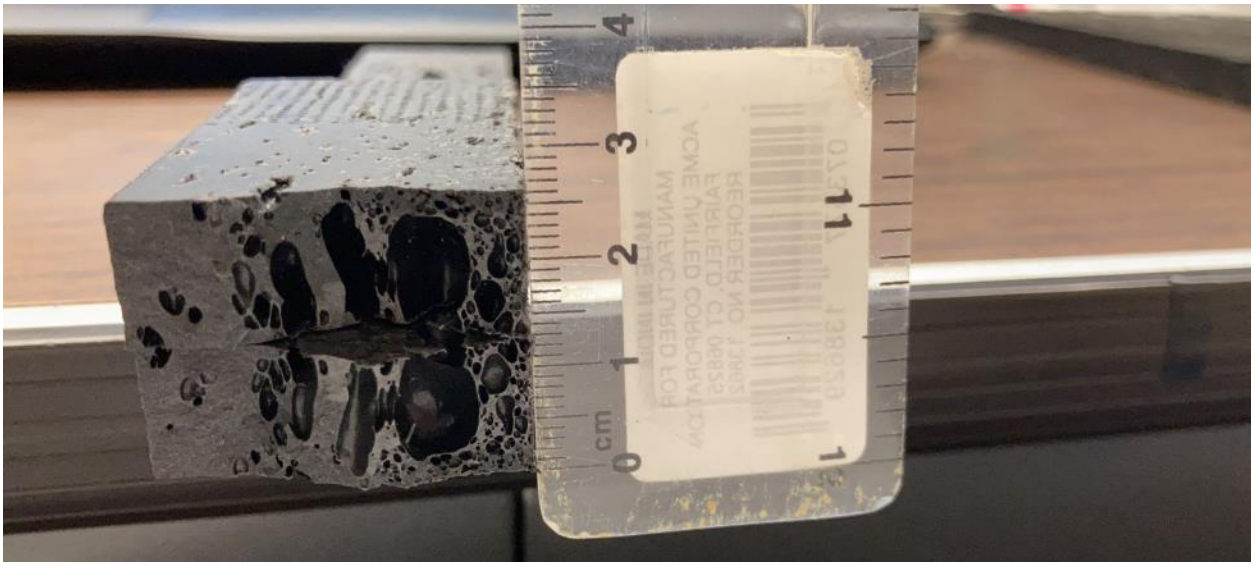

Figure 80. Detailed View of Damaged Area of Sample C1_2

Sample C2_2

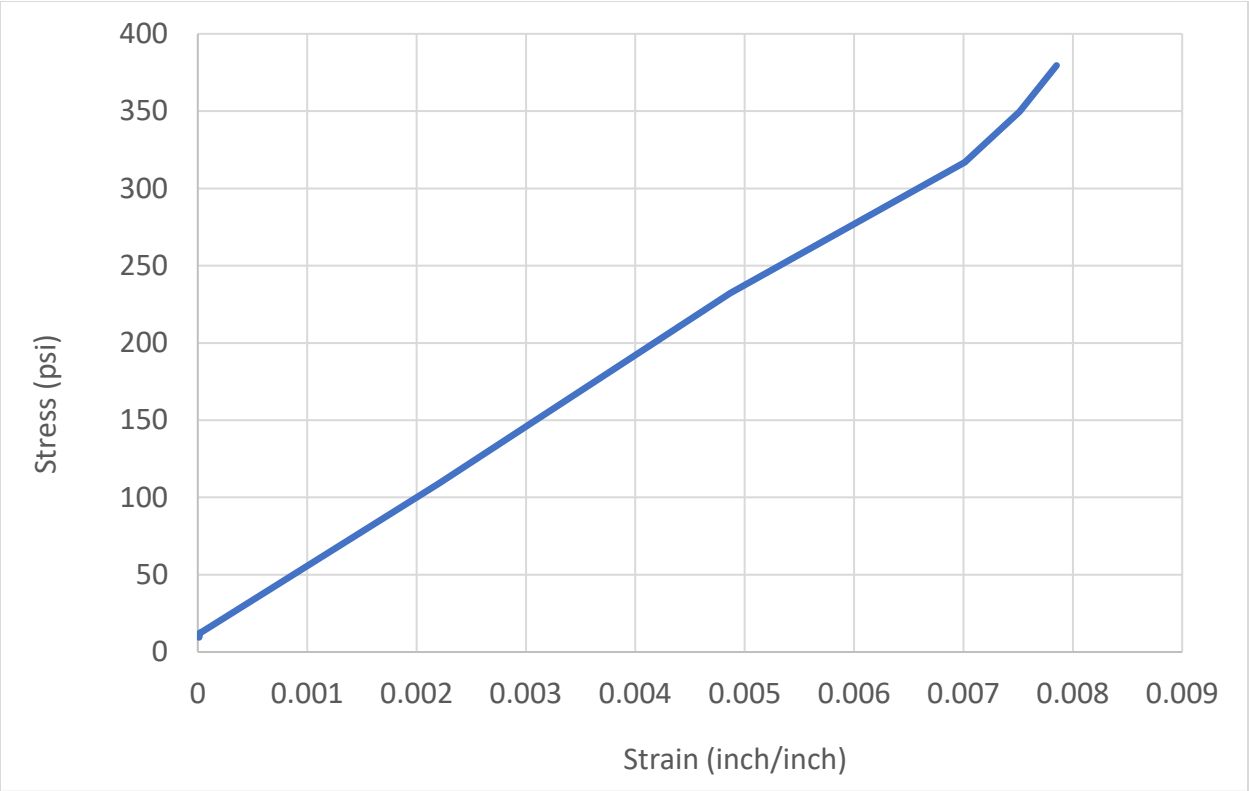

Figure 81. Stress-Strain Curve of Sample C2_2

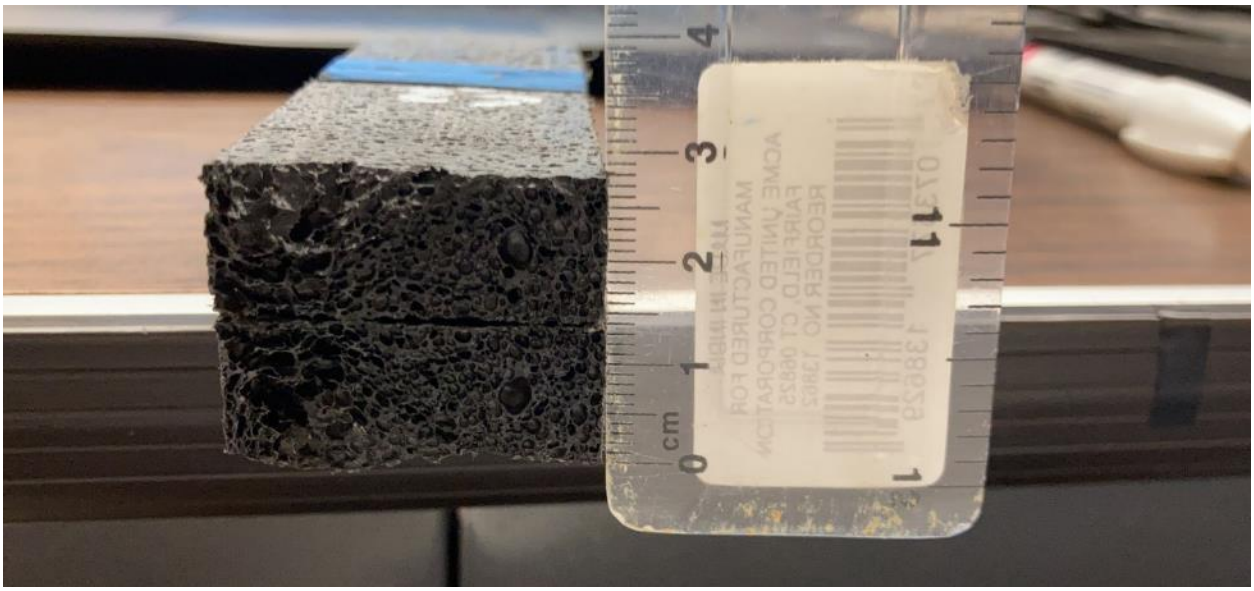

Figure 82. Detailed View of Damaged Area of Sample C2_2

Sample C3_2

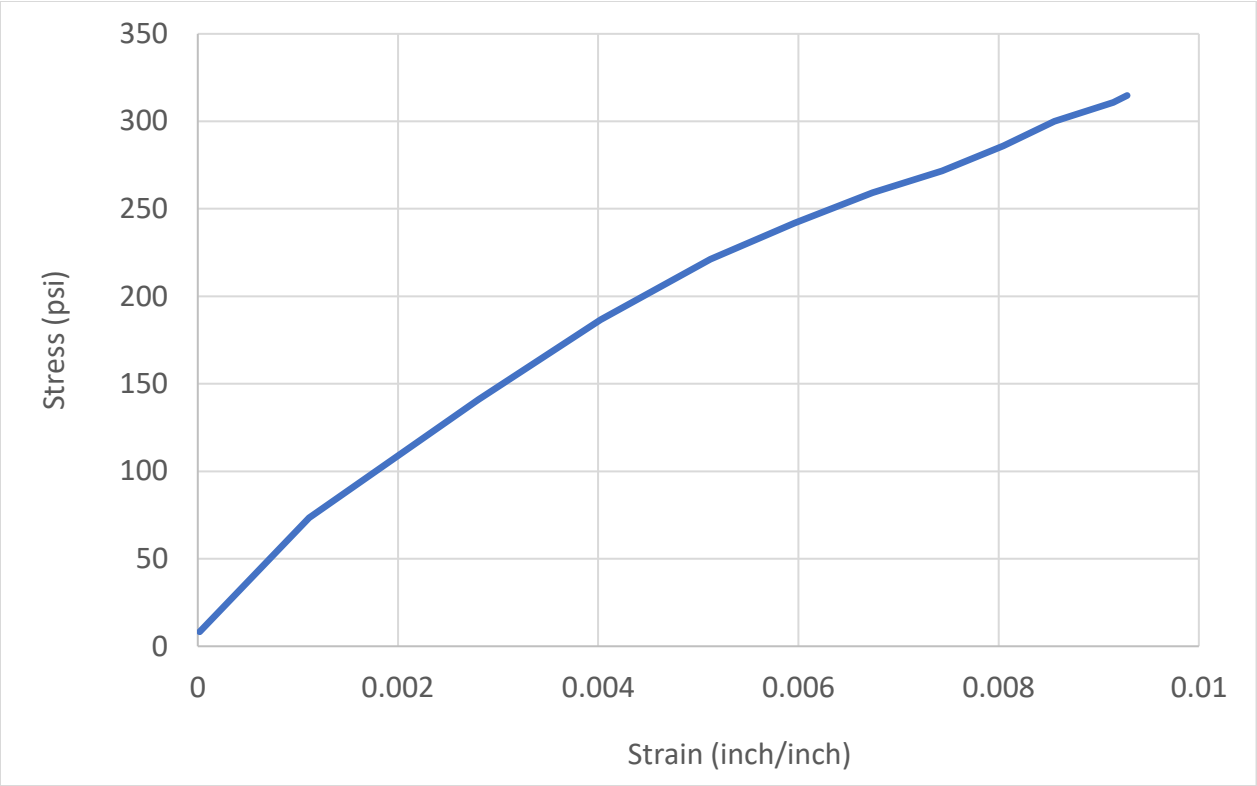

Figure 83. Stress-Strain Curve of Sample C3_2

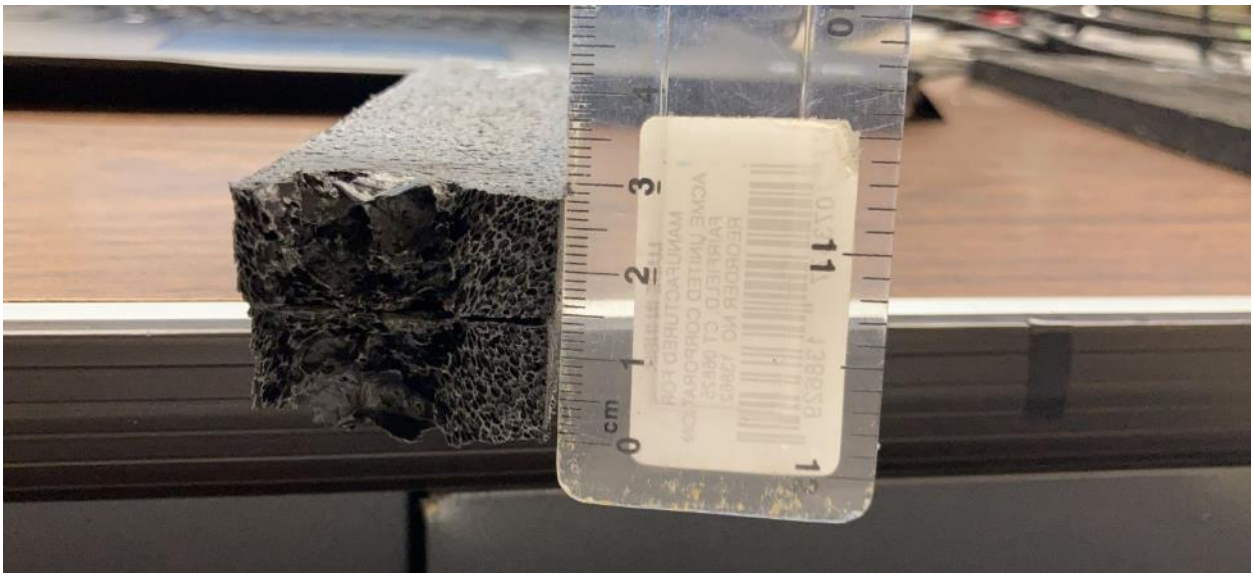

Figure 84. Detailed View of Damaged Area of Sample C3_2

Sample C4_2

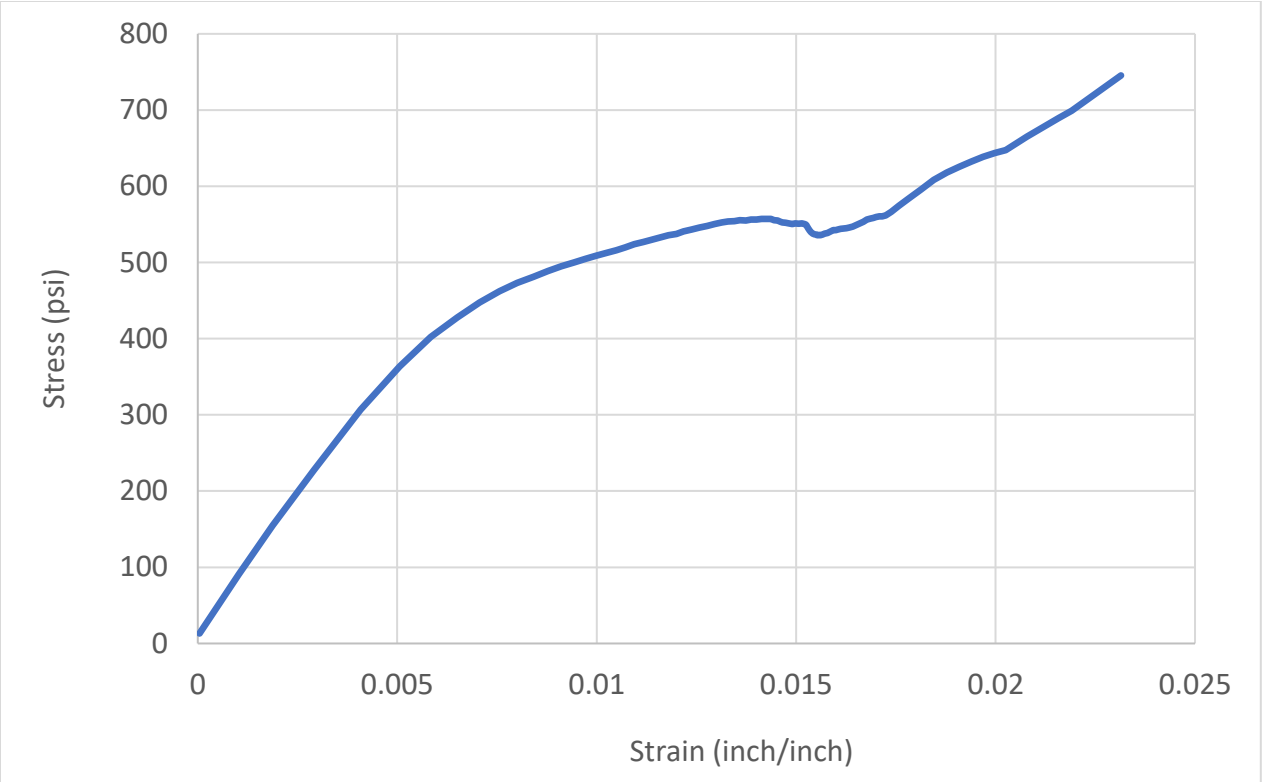

Figure 85. Stress-Strain Curve of Sample C4_2

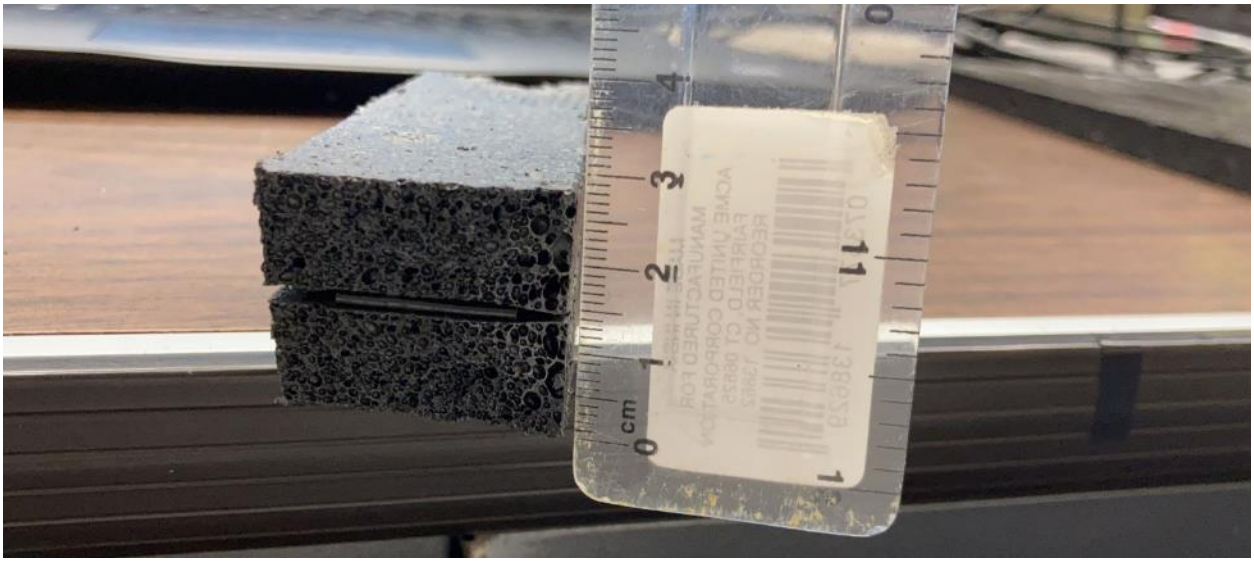

Figure 86. Detailed View of Damaged Area of Sample C4_2

Sample C5_2

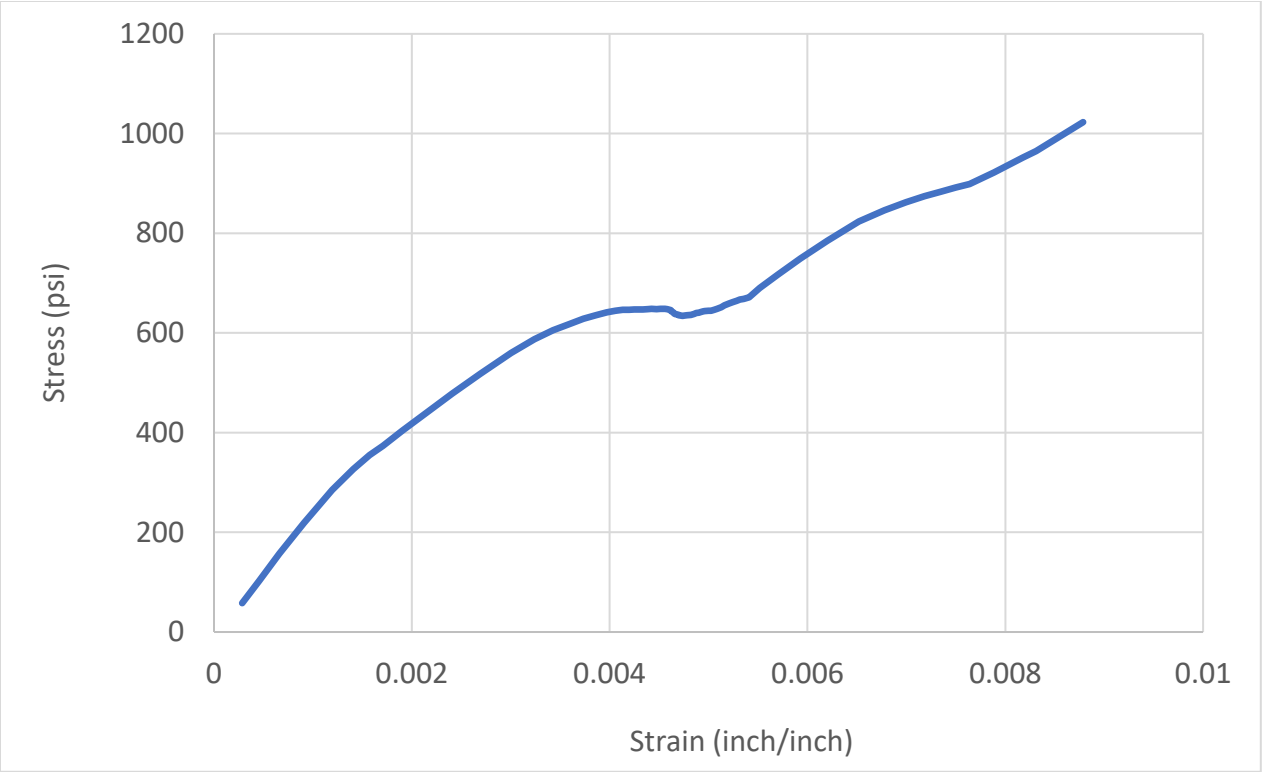

Figure 87. Stress-Strain Curve of Sample C5_2

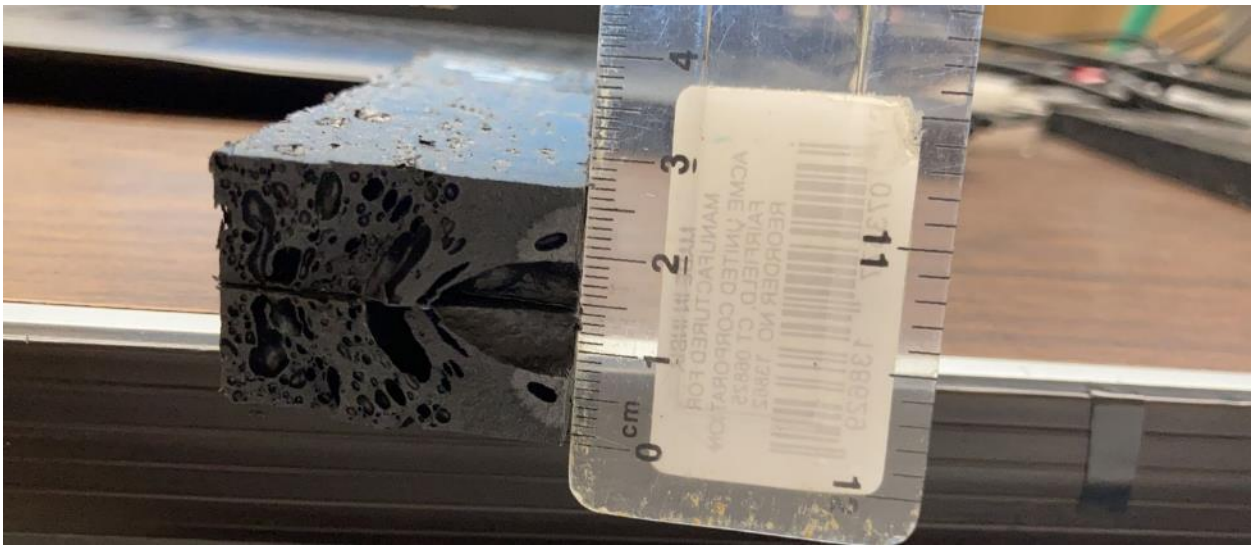

Figure 88. Detailed View of Damaged Area of Sample C5_2

Sample D1_2

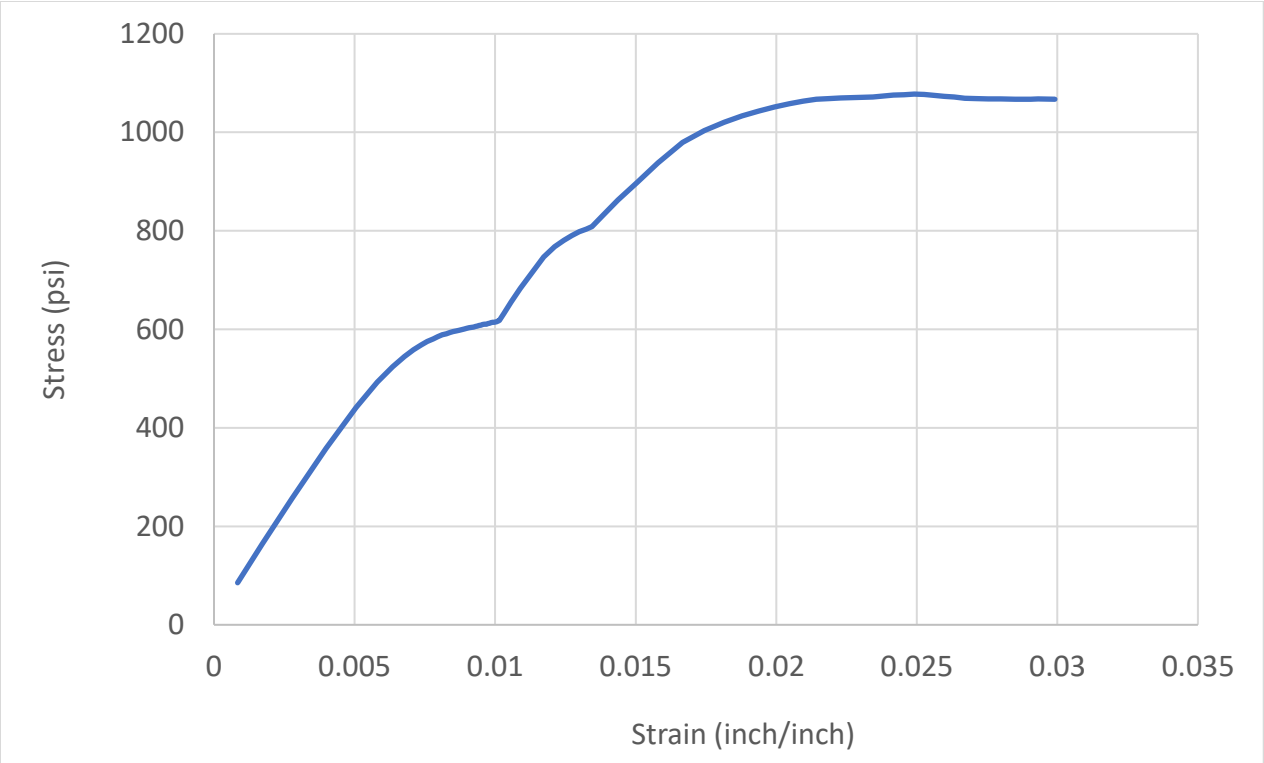

Figure 89. Stress-Strain Curve of Sample D1_2

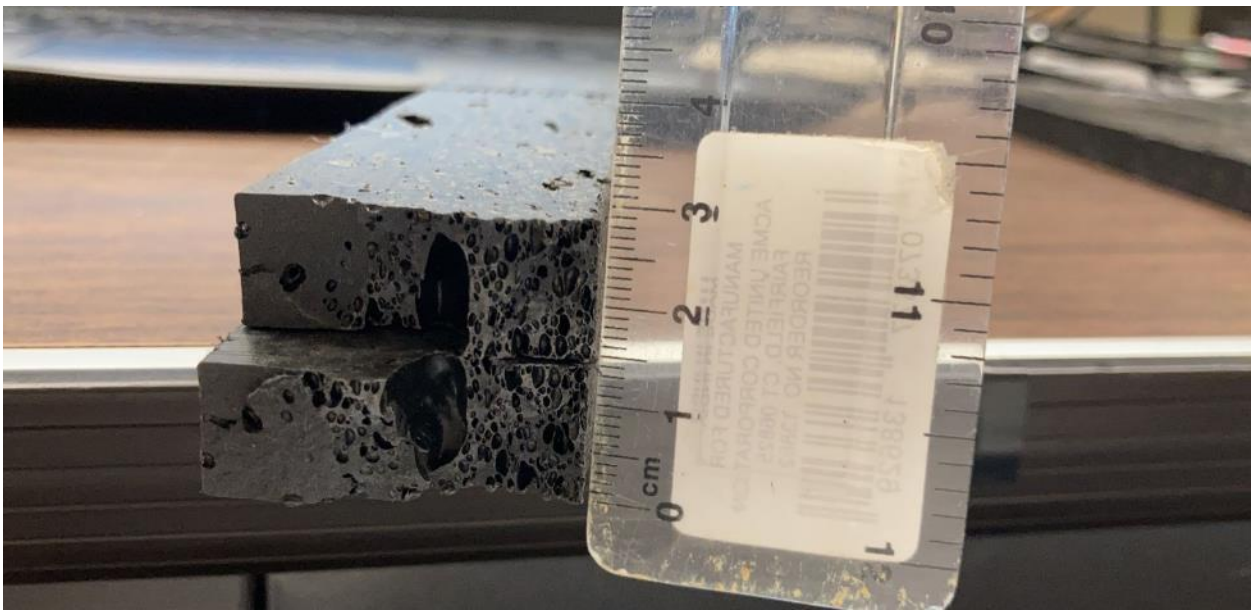

Figure 90. Detailed View of Damaged Area of Sample D1_2

Sample D2_2

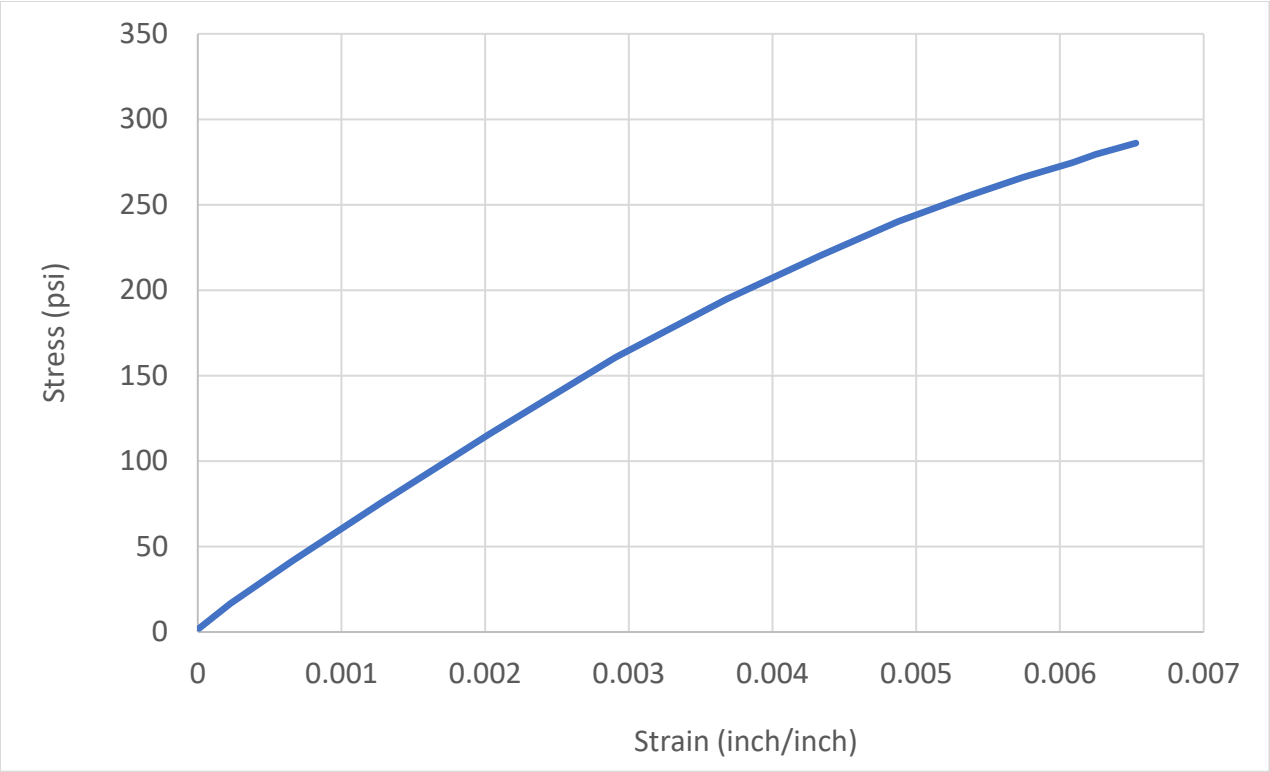

Figure 91. Stress-Strain Curve of Sample D2_2

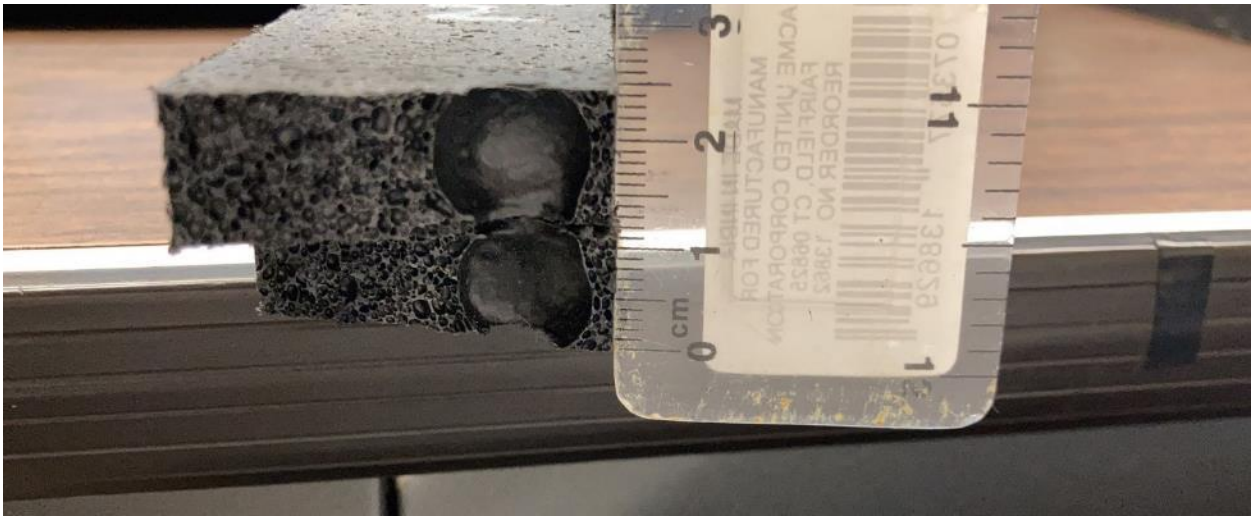

Figure 92. Detailed View of Damaged Area of Sample D2_2

Sample D3_2

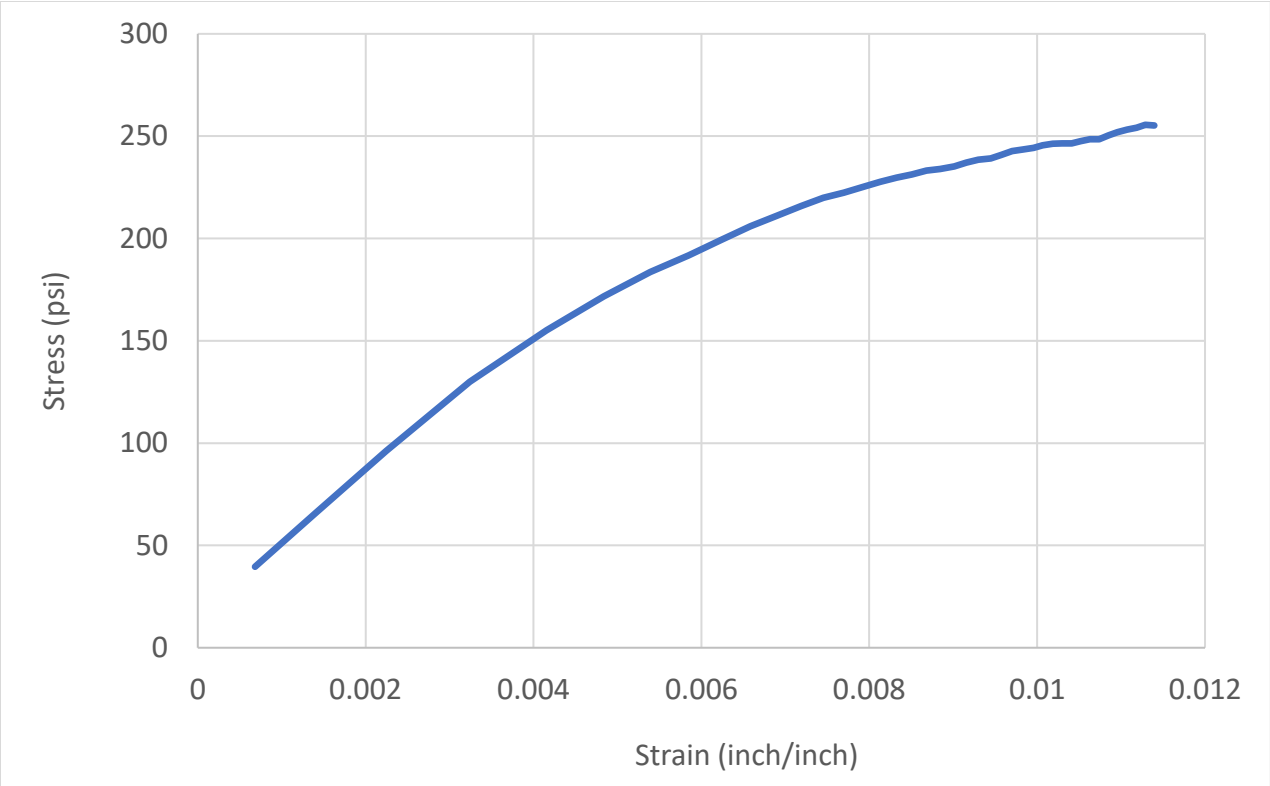

Figure 93. Stress-Strain Curve of Sample D3_2

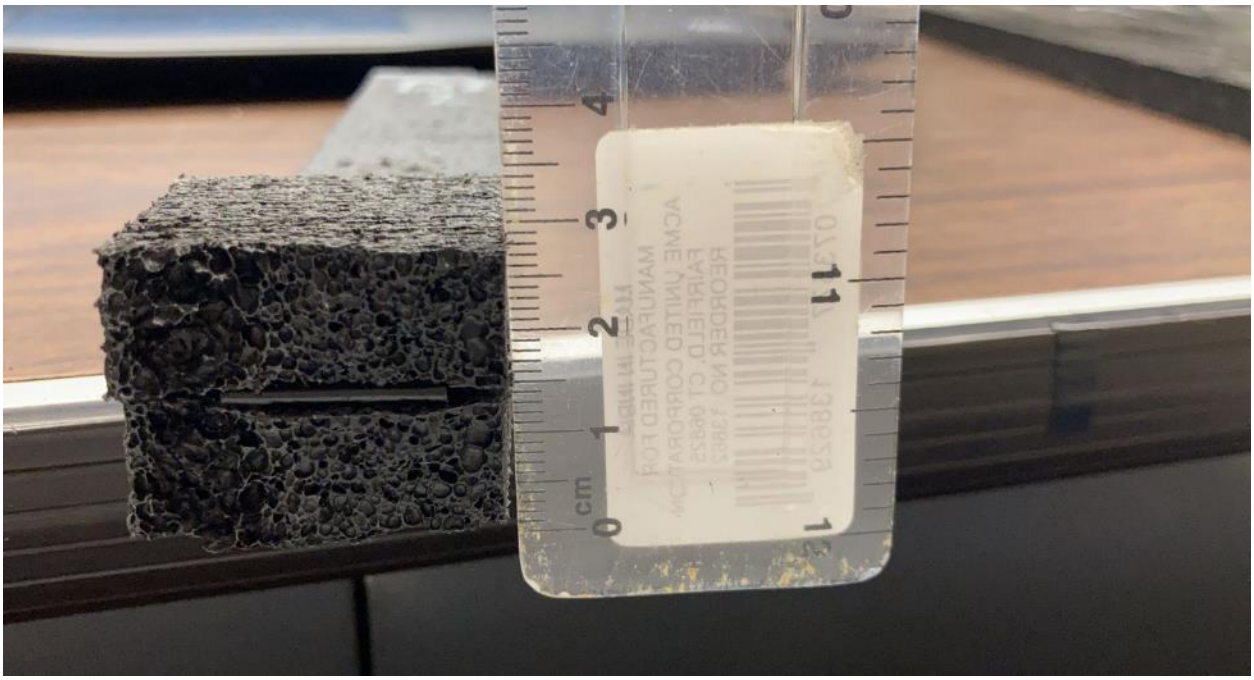

Figure 94. Detailed View of Damaged Area of Sample D3_2

Sample D4_2

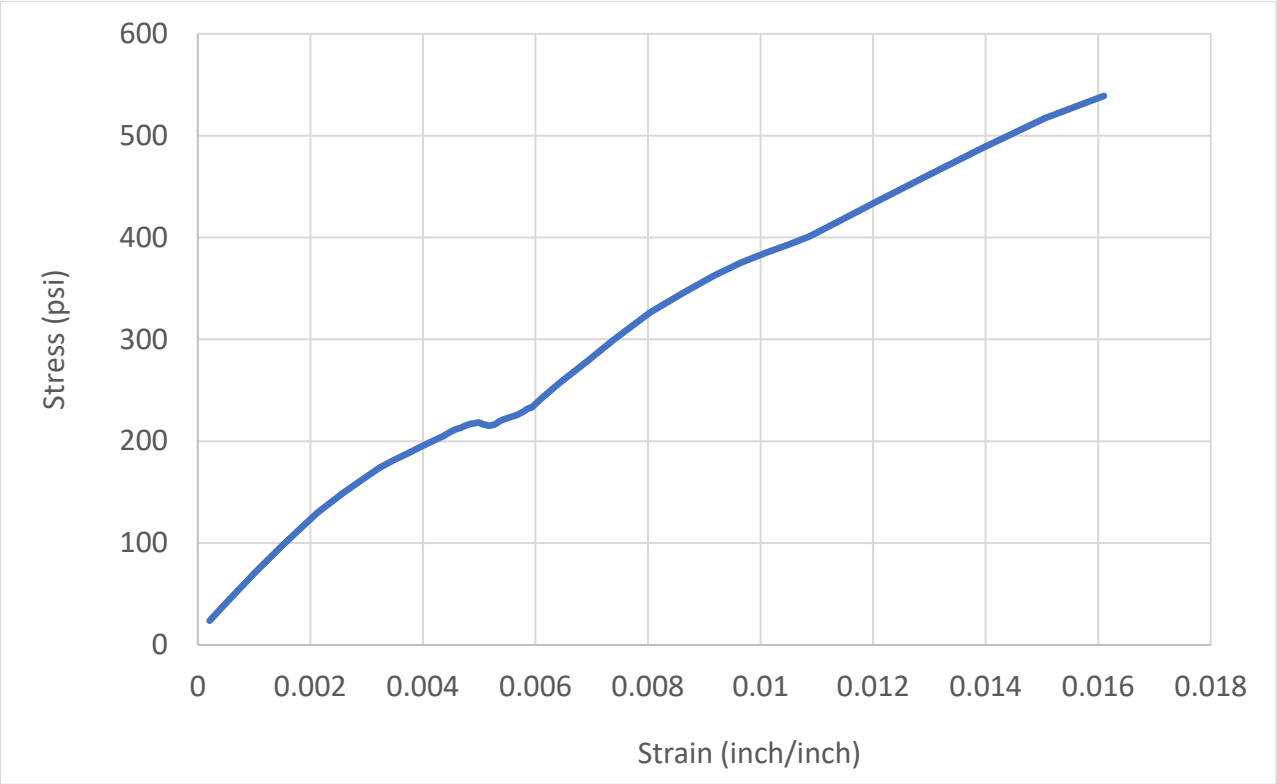

Figure 95. Stress-Strain Curve of Sample D4_2

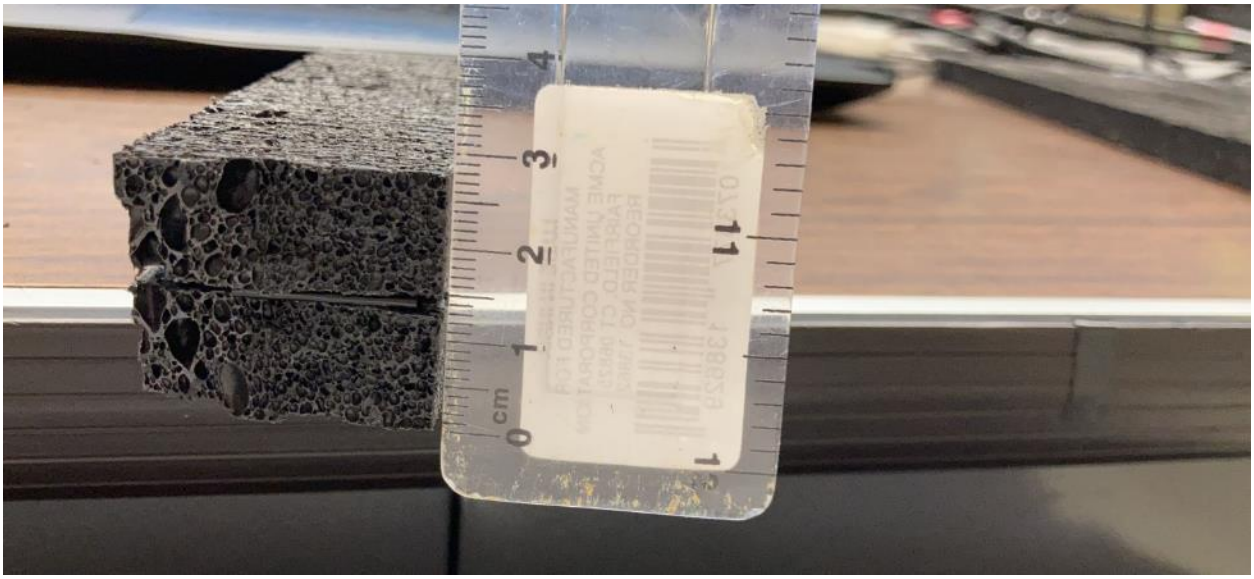

Figure 96. Detailed View of Damaged Area of Sample D4_2

Sample D5_2

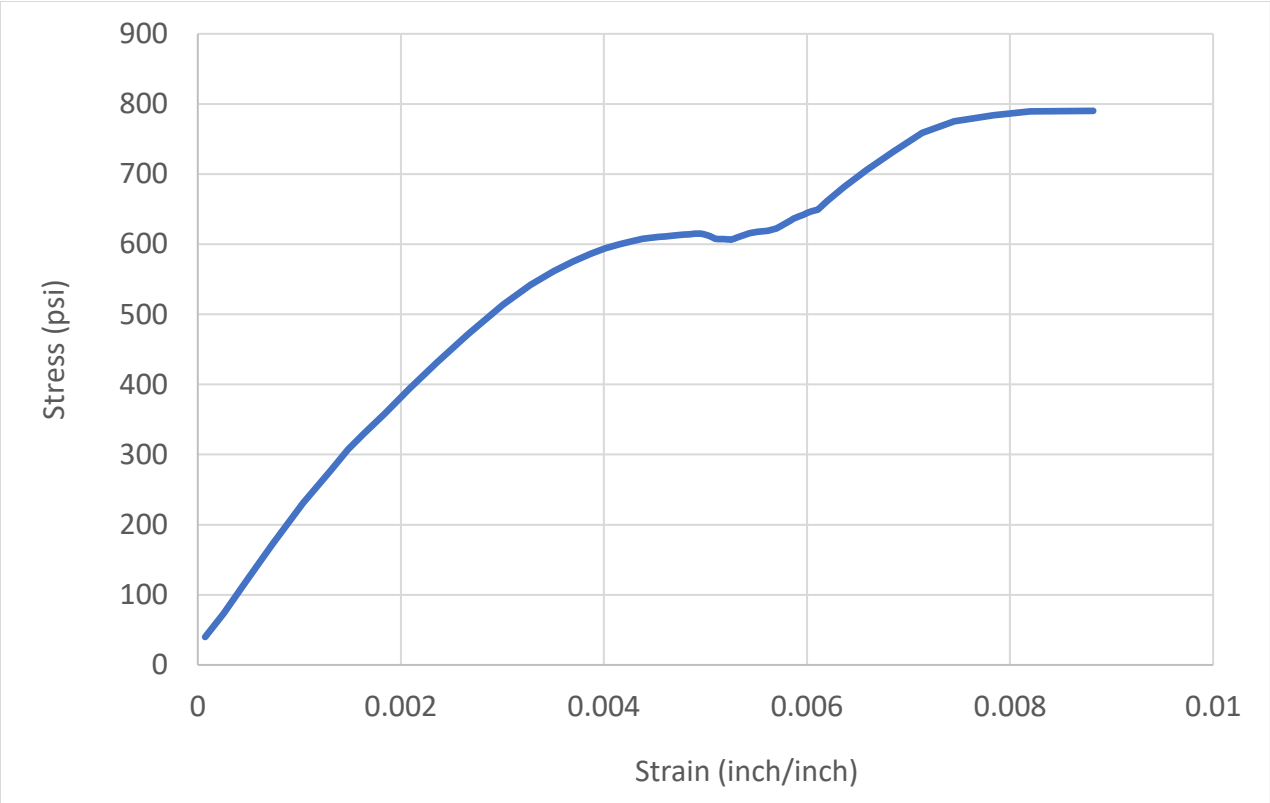

Figure 97. Stress-Strain Curve of Sample D5_2

Figure 98. Detailed View of Damaged Area of Sample D5_2

Sample A1_1

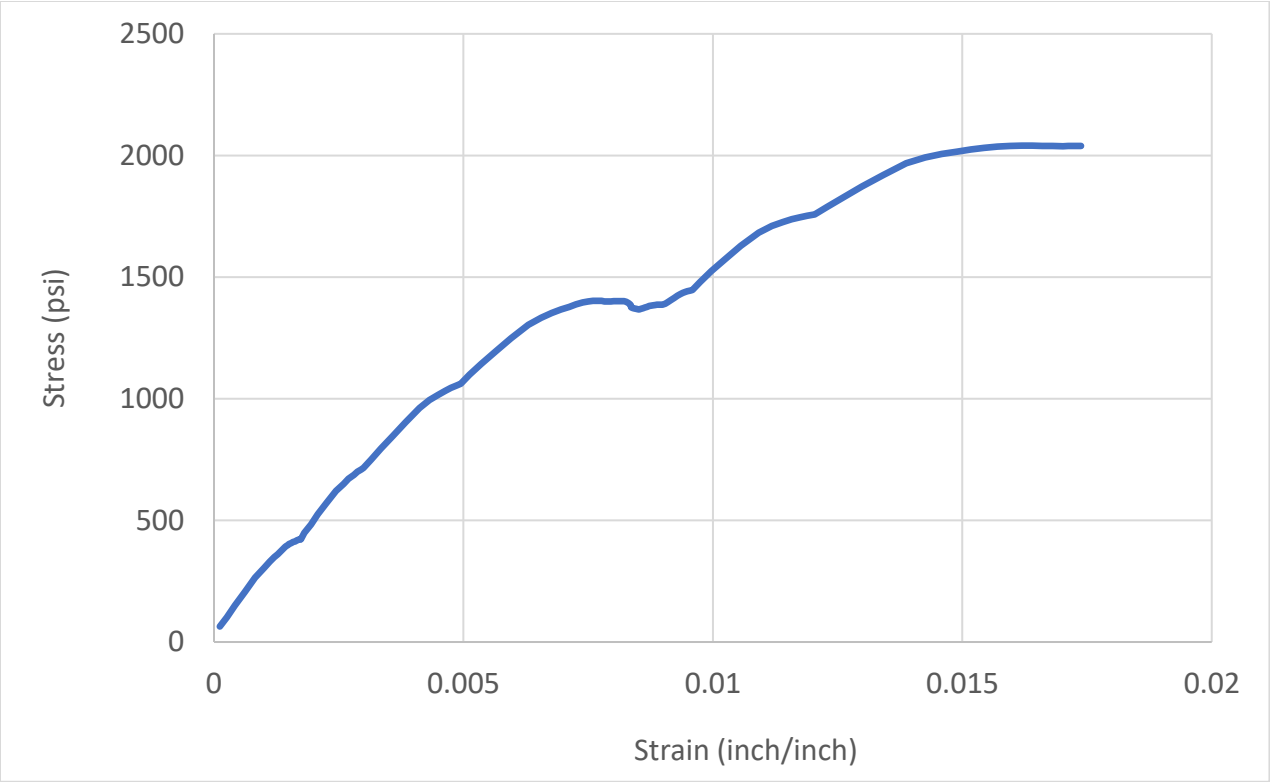

Figure 99. Stress-Strain Curve of Sample A1_1

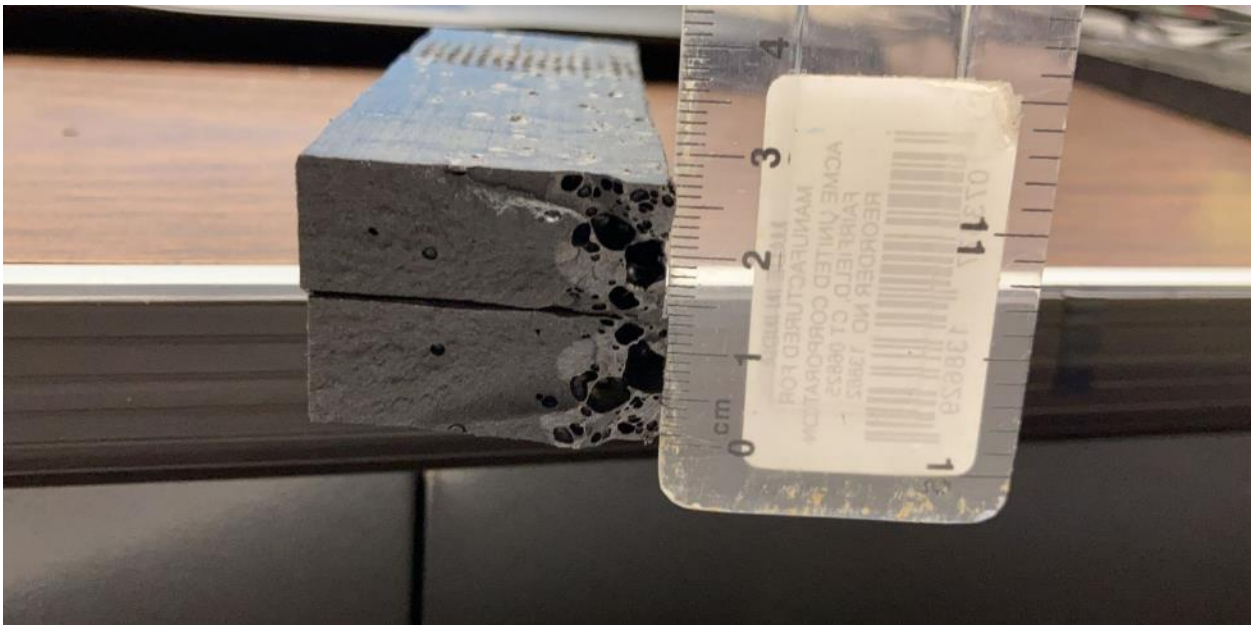

Figure 100. Detailed View of Damaged Area of Sample A1_1

Sample A2_1

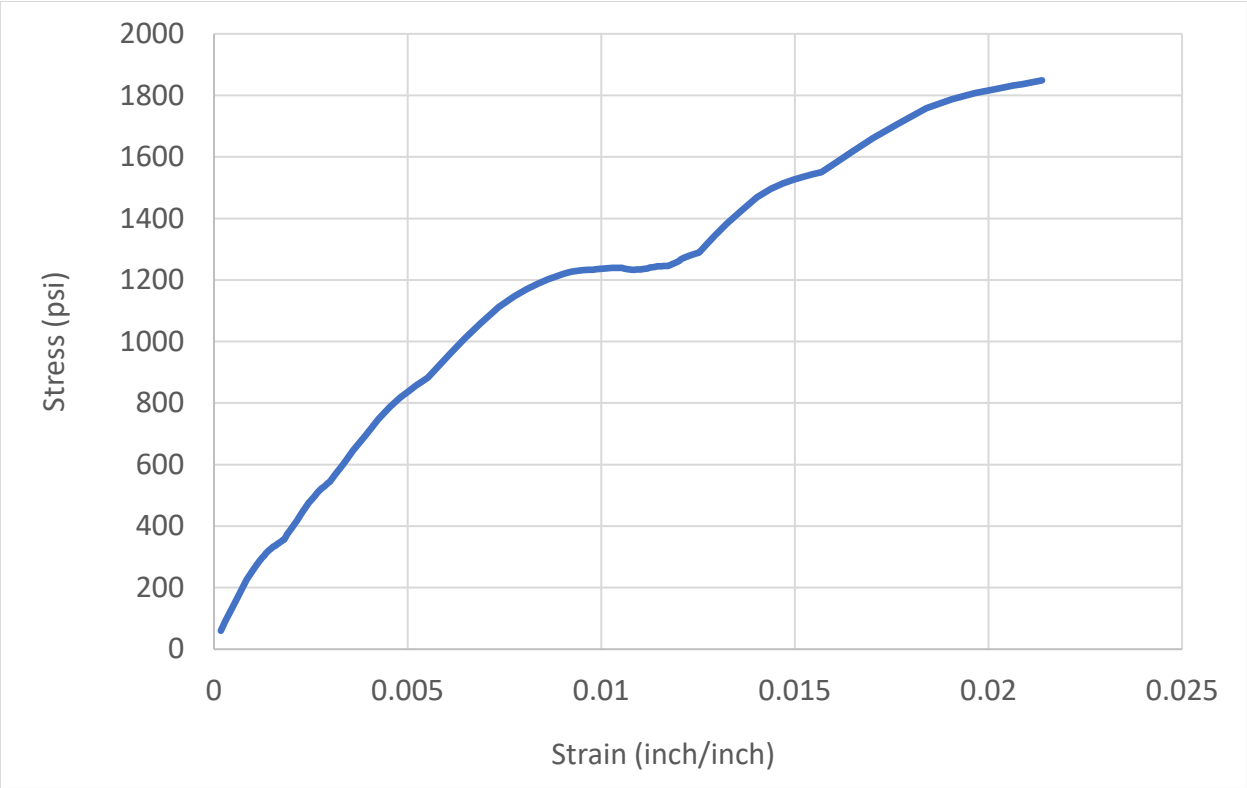

Figure 101. Stress-Strain Curve of Sample A2_1

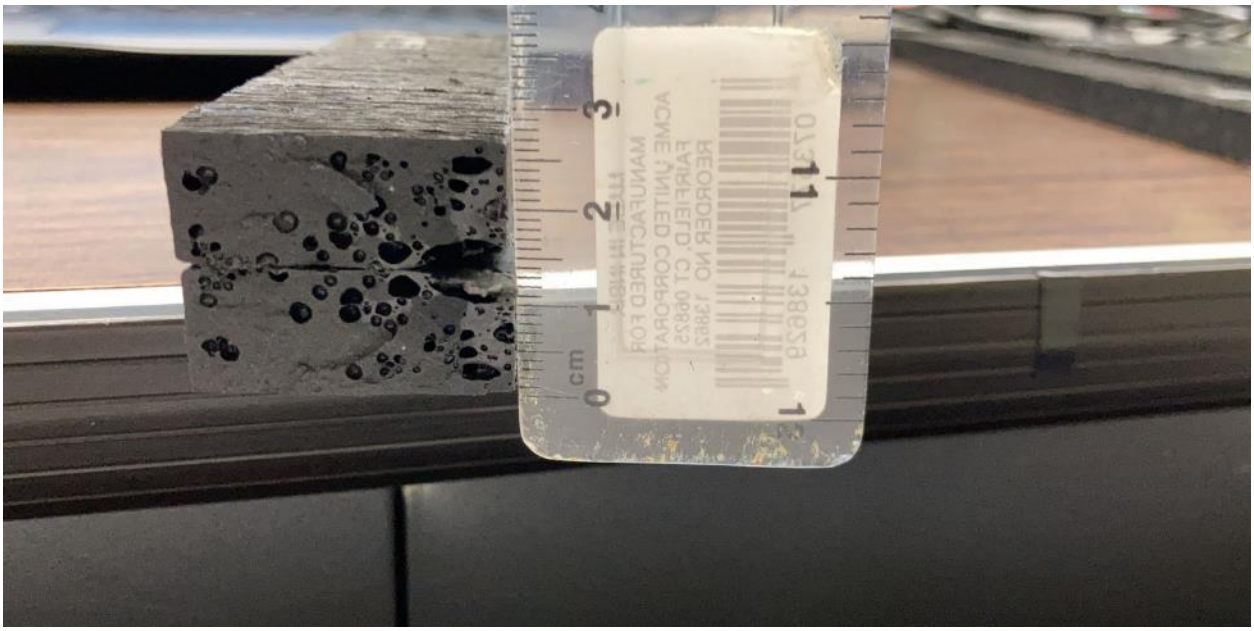

Figure 102. Detailed View of Damaged Area of Sample A2_1

Sample A3_1

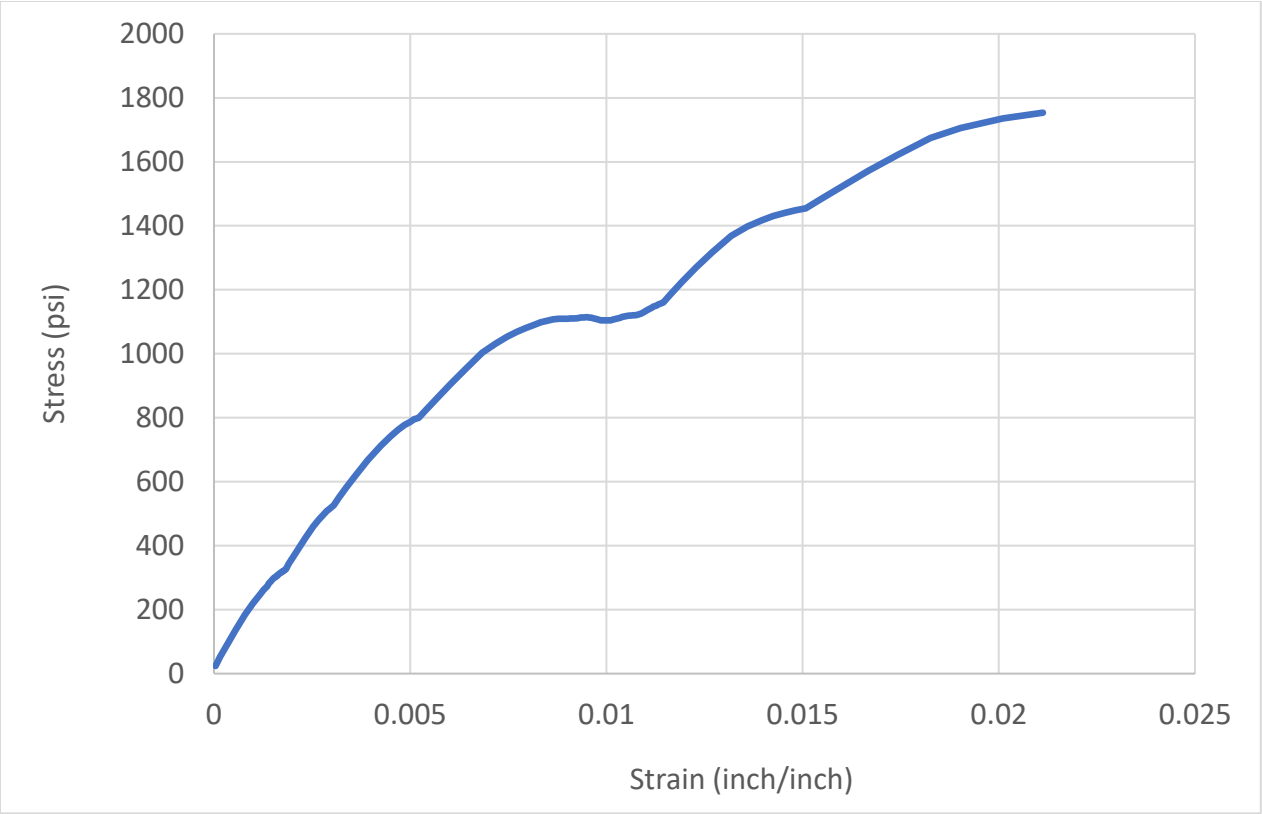

Figure 103. Stress-Strain Curve of Sample A3_1

Figure 104. Detailed View of Damaged Area of Sample A3_1

Sample A4_1

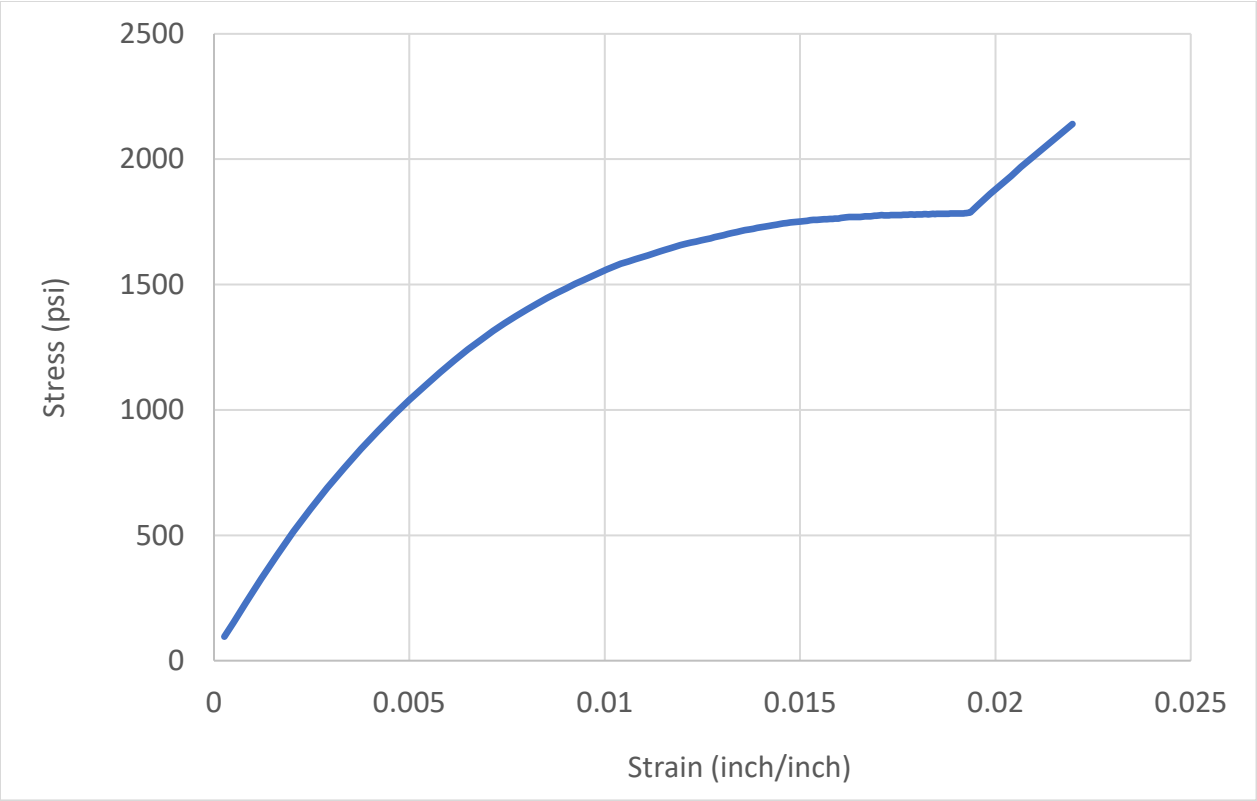

Figure 105. Stress-Strain Curve of Sample A4_1

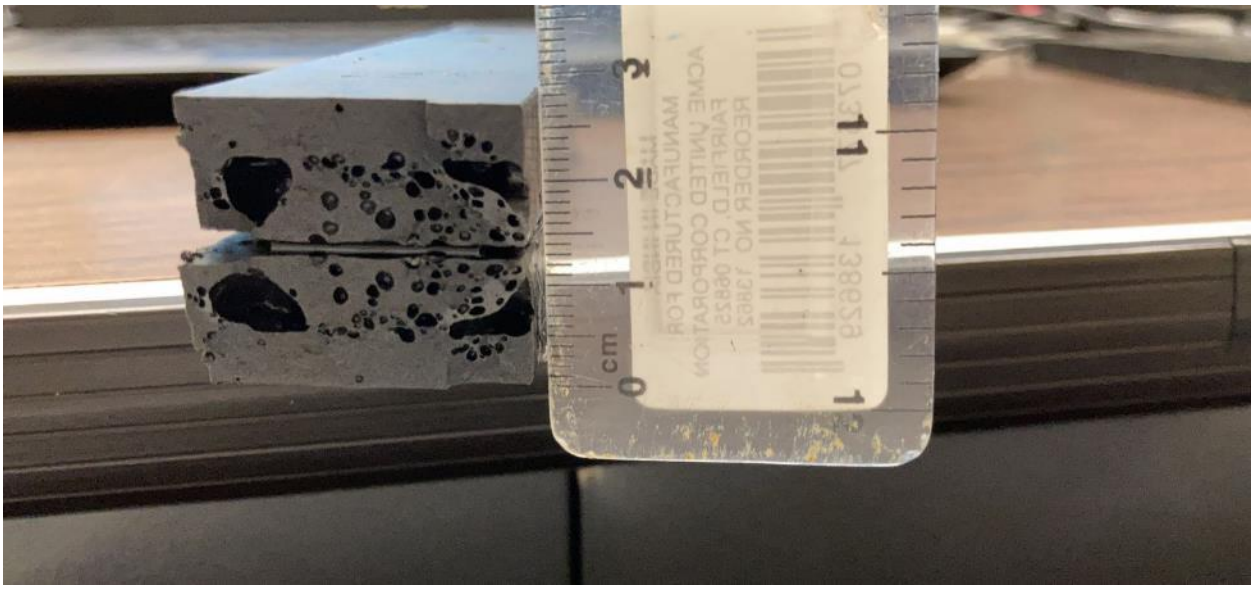

Figure 106. Detailed View of Damaged Area of Sample A4_1

Sample A5_1

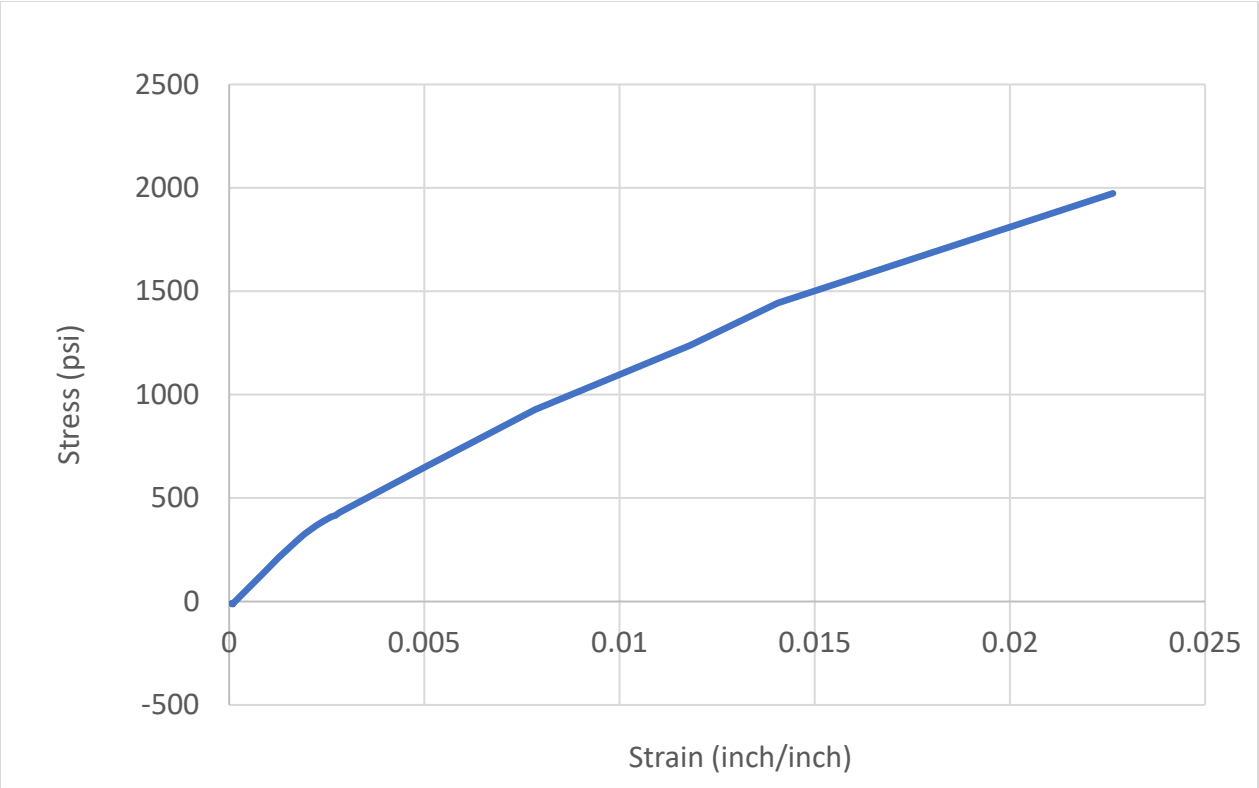

Figure 107. Stress-Strain Curve of Sample A5_1

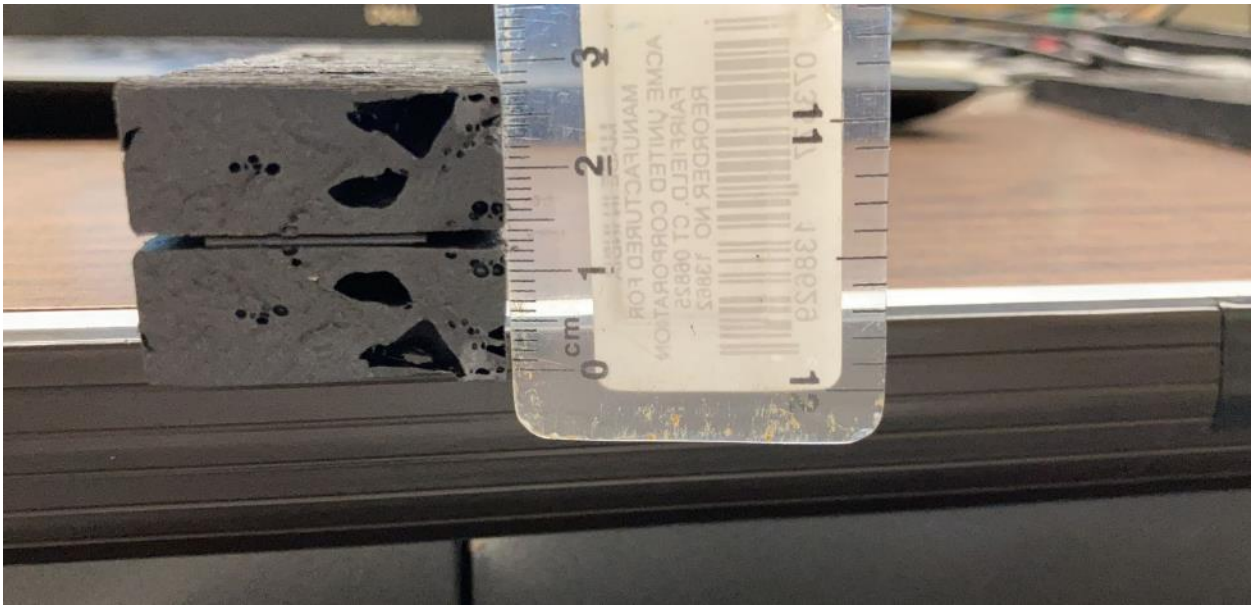

Figure 108. Detailed View of Damaged Area of Sample A5_1

Sample B1_1

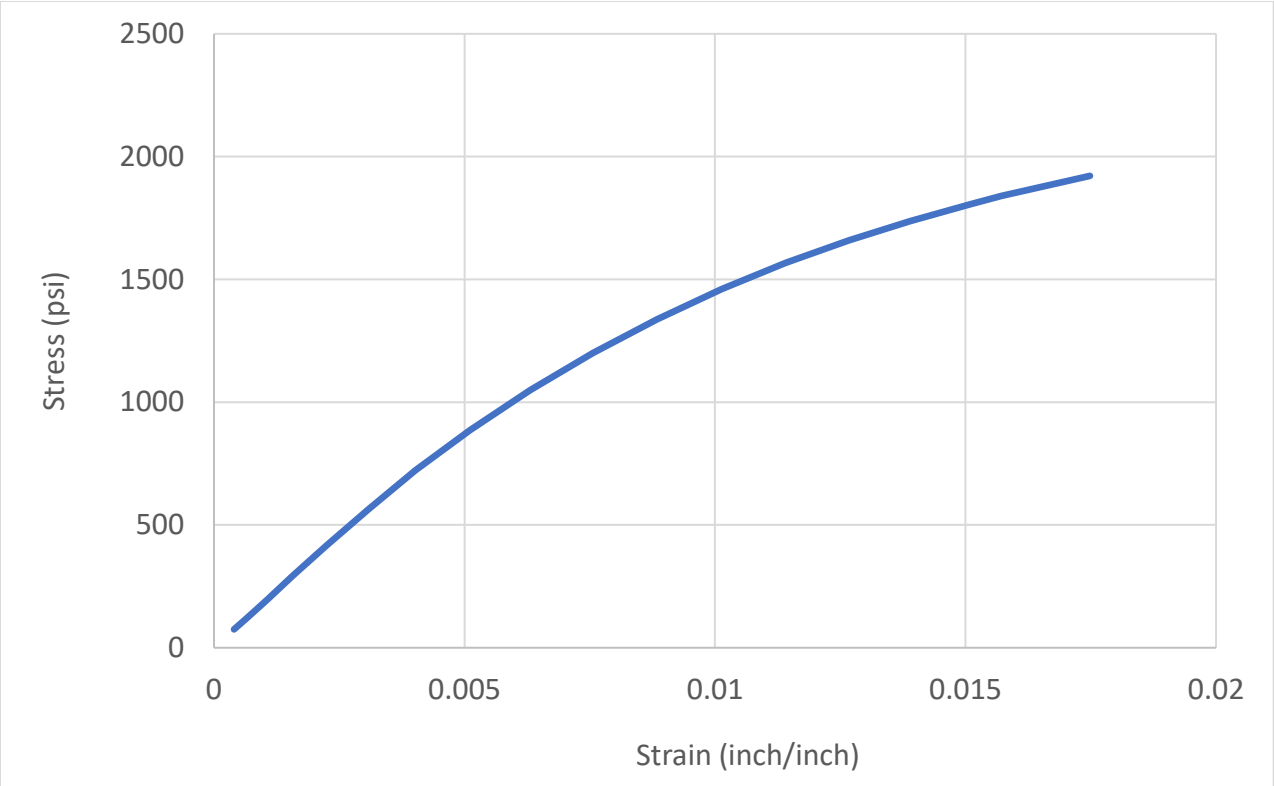

Figure 109. Stress-Strain Curve of Sample B1_1

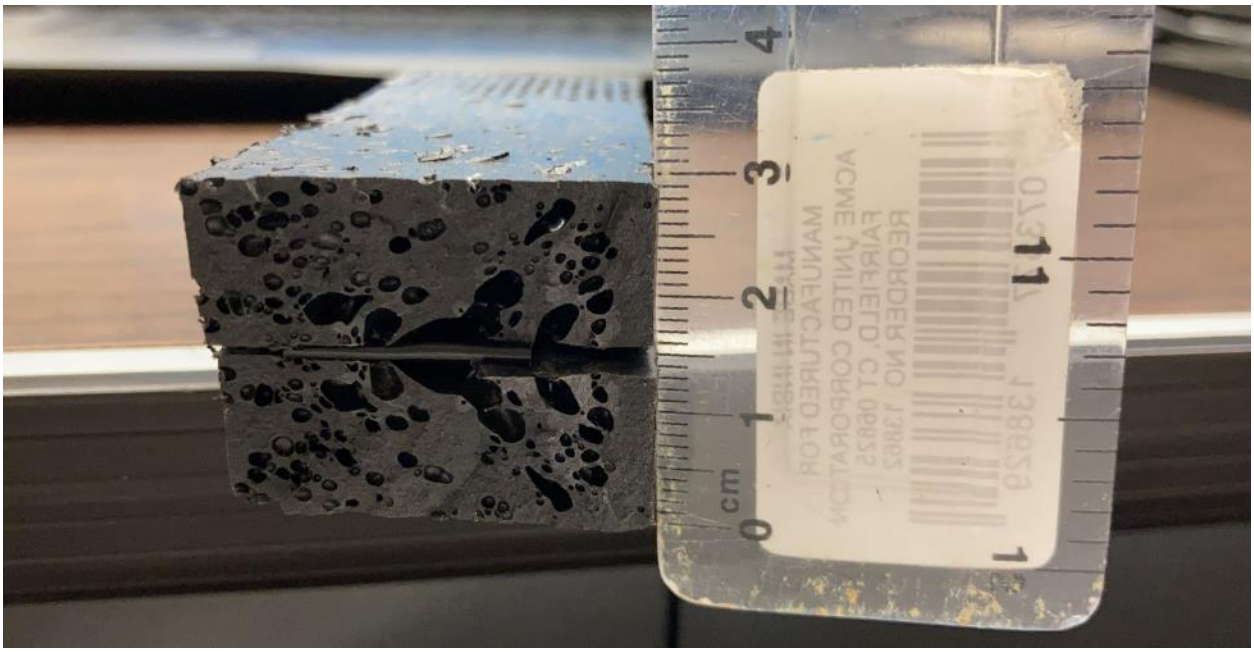

Figure 110. Detailed View of Damaged Area of Sample B1_1

Sample B2_1

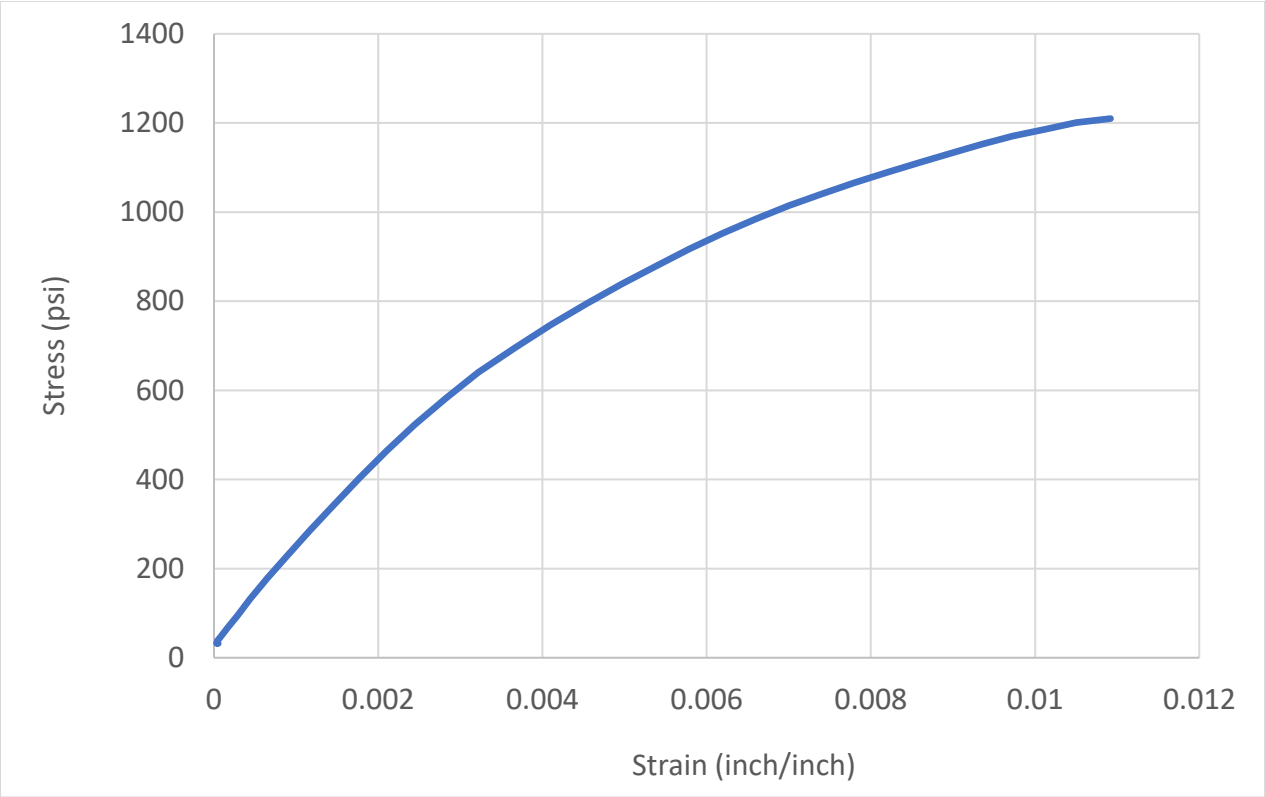

Figure 111. Stress-Strain Curve of Sample B2_1

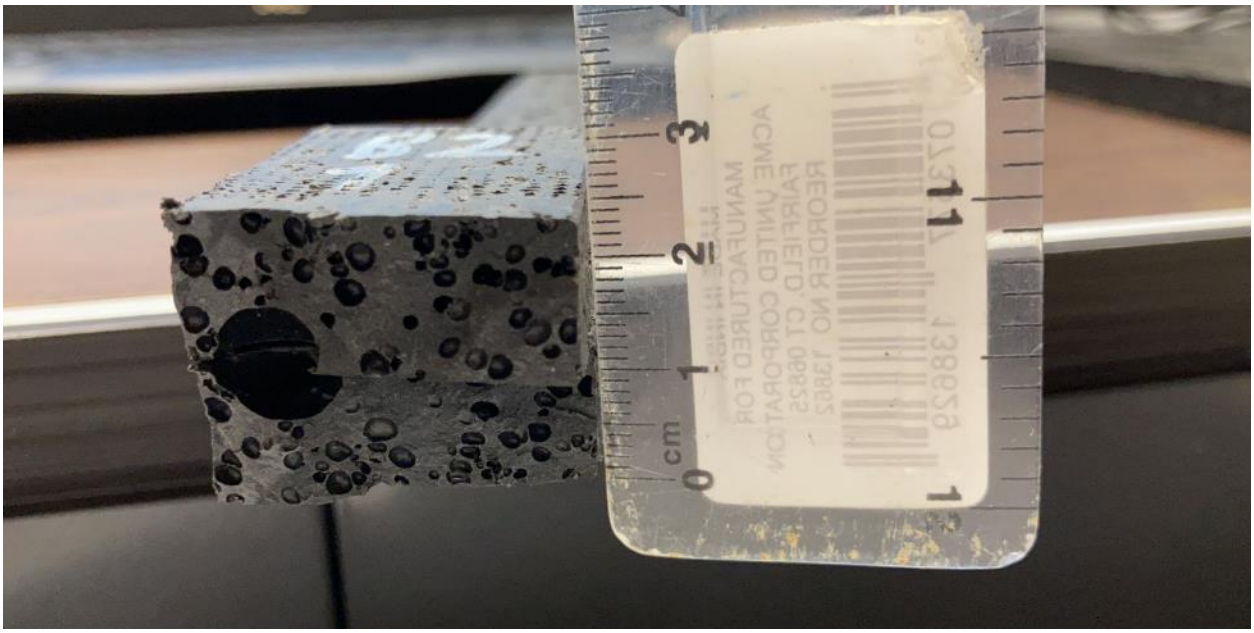

Figure 112. Detailed View of Damaged Area of Sample B2_1

Sample B3_1

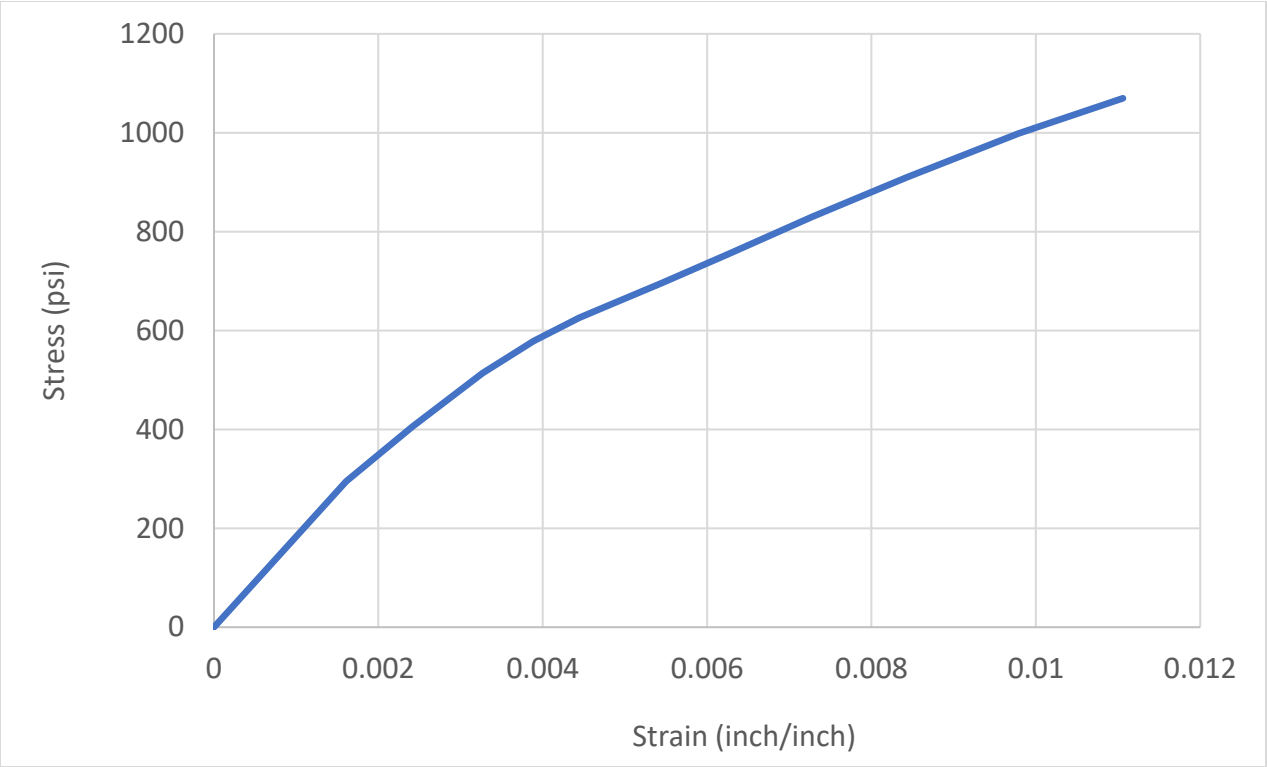

Figure 113. Stress-Strain Curve of Sample B3_1

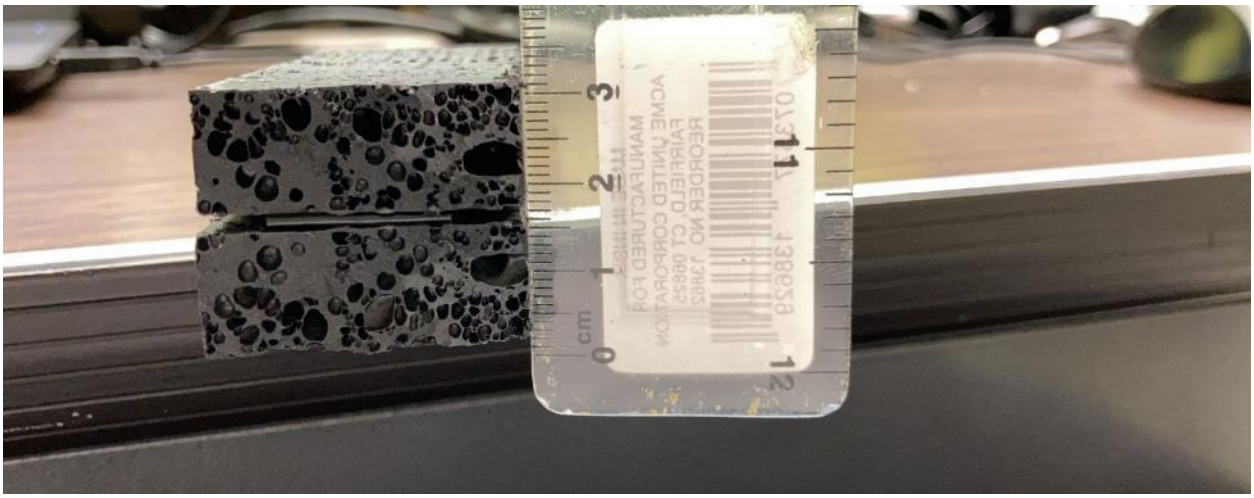

Figure 114. Detailed View of Damaged Area of Sample B3_1

Sample B4_1

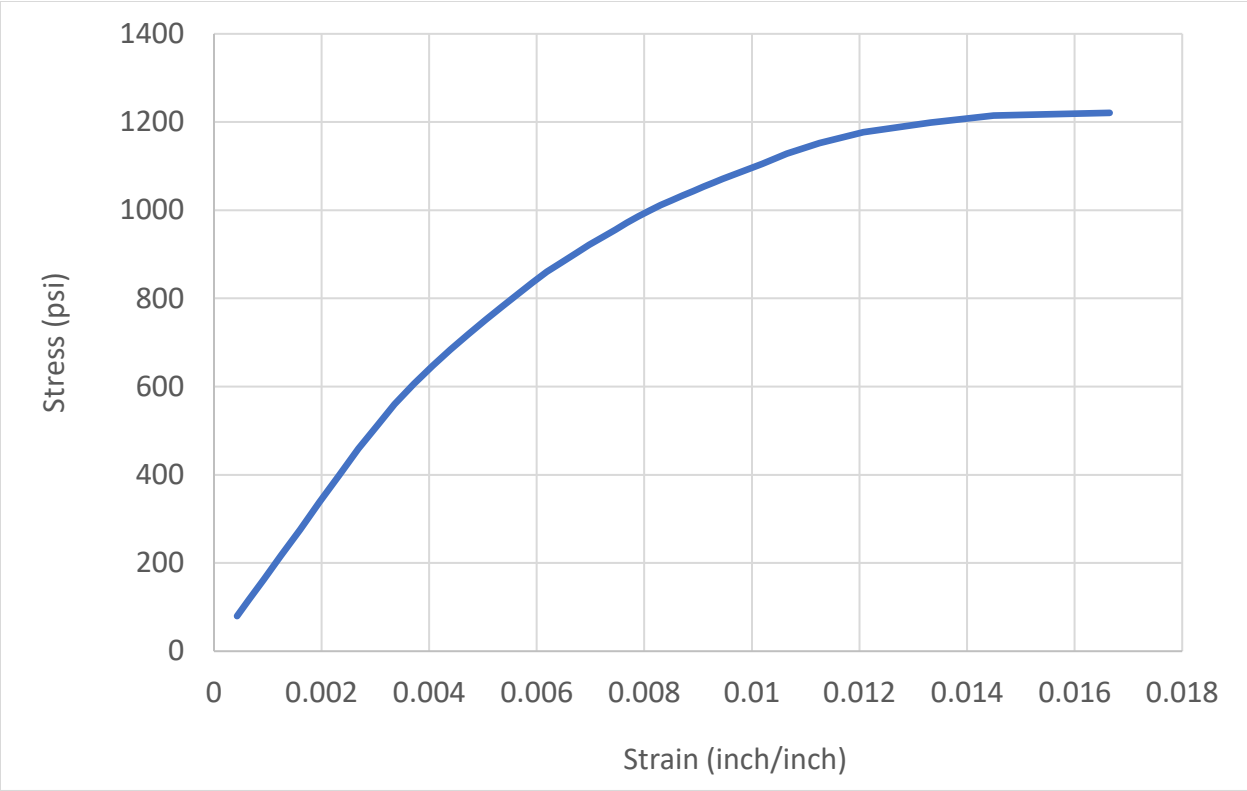

Figure 115. Stress-Strain Curve of Sample B4_1

Figure 116. Detailed View of Damaged Area of Sample B4_1

Sample C2_1

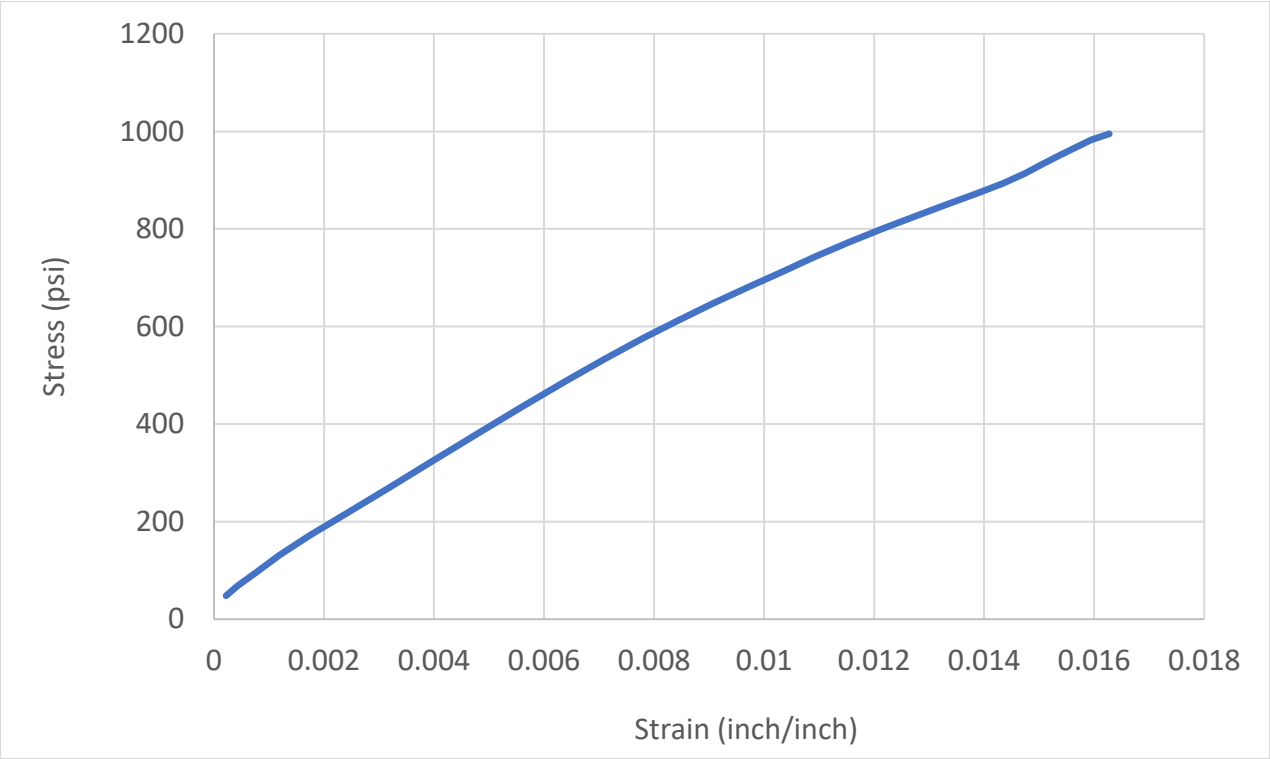

Figure 117. Stress-Strain Curve of Sample C2_1

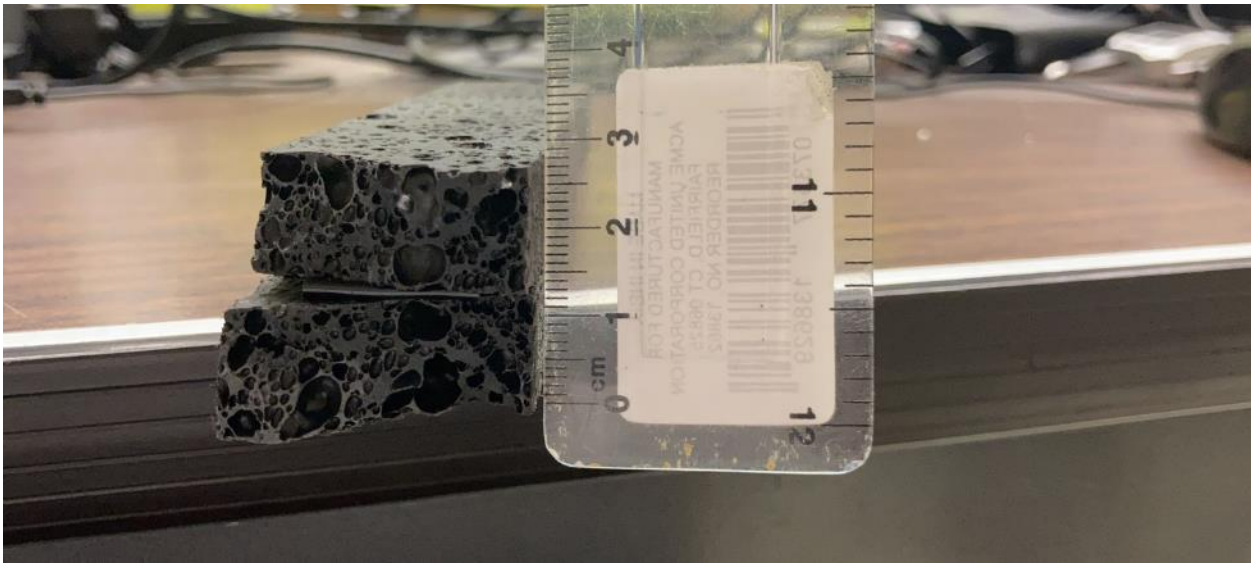

Figure 118. Detailed View of Damaged Area of Sample C2_1

Sample C3_1

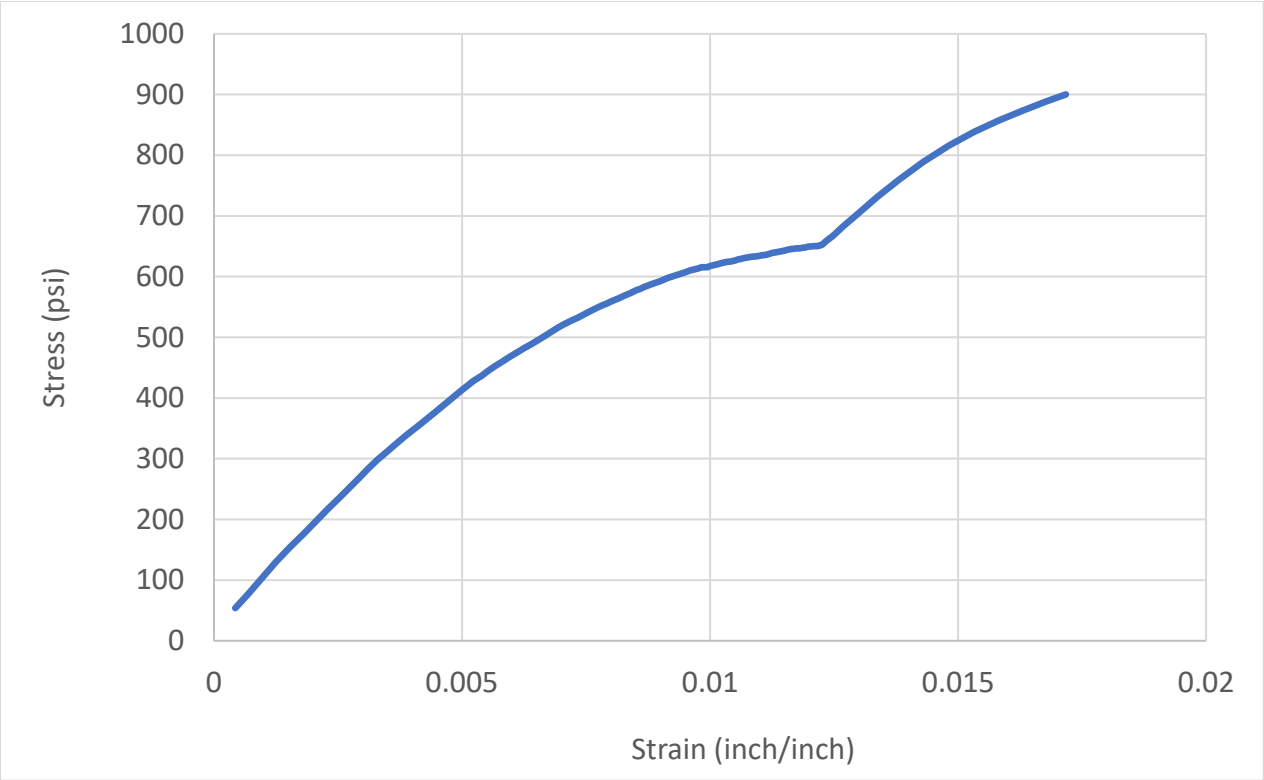

Figure 119. Stress-Strain Curve of Sample C3_1

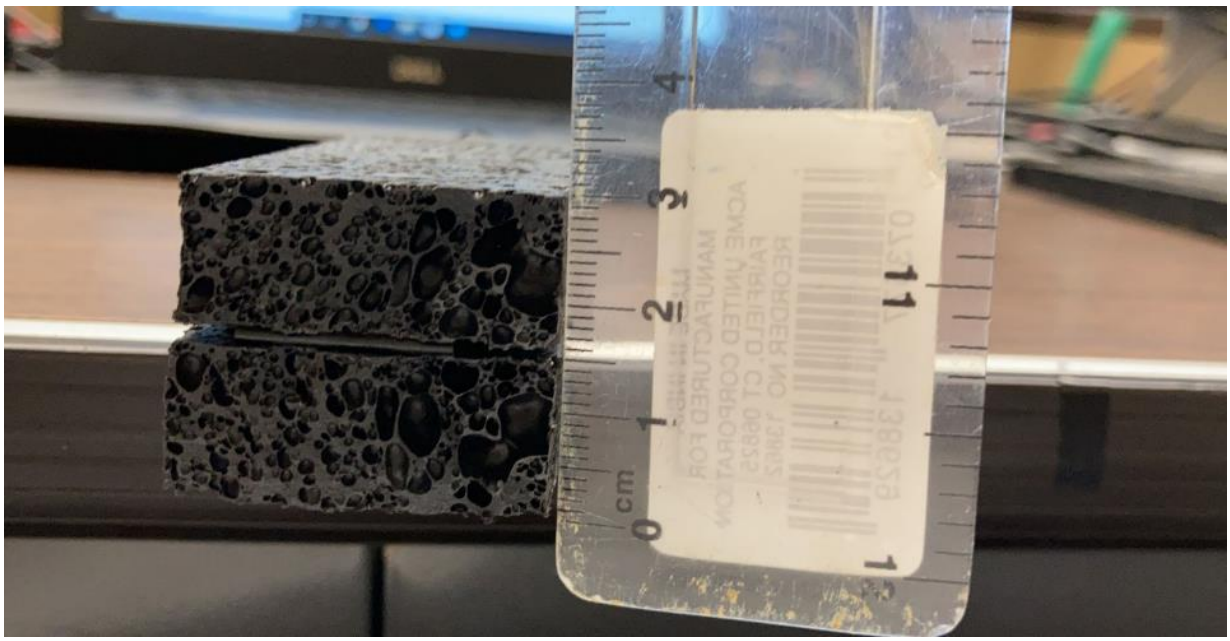

Figure 120. Detailed View of Damaged Area of Sample C3_1

Sample C4_1

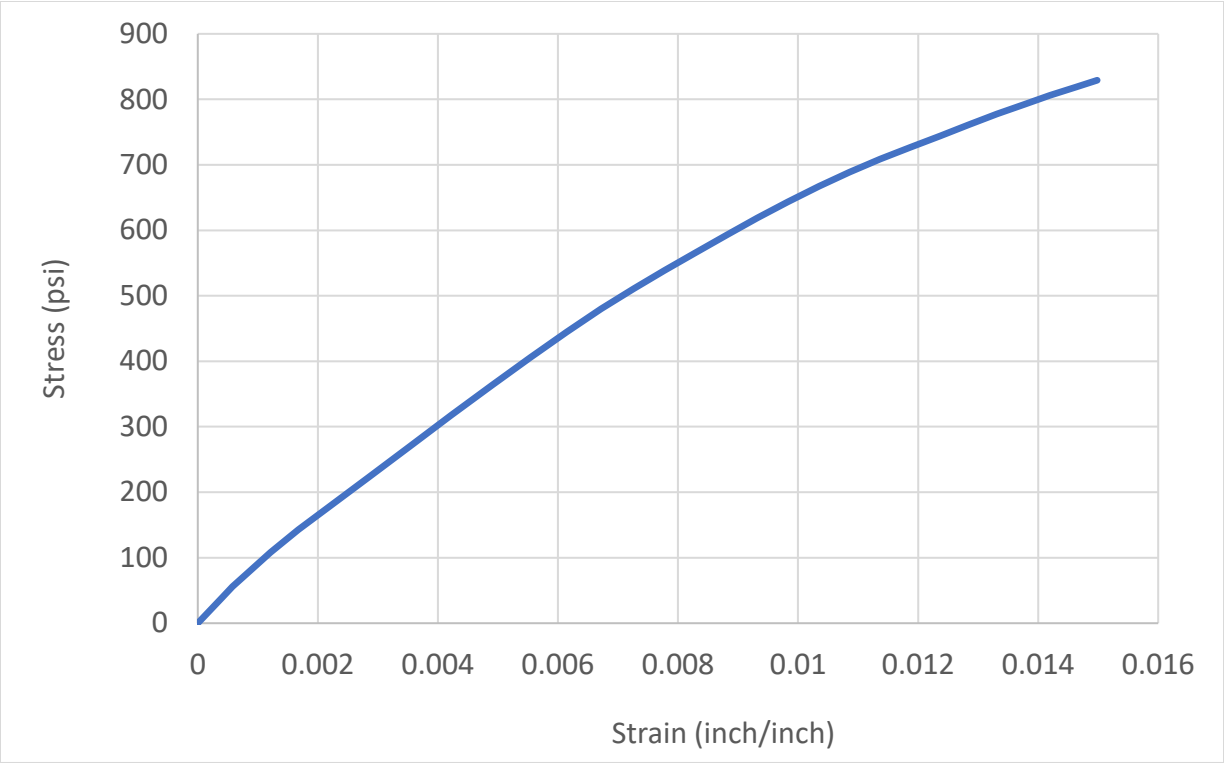

Figure 121. Stress-Strain Curve of Sample C4_1

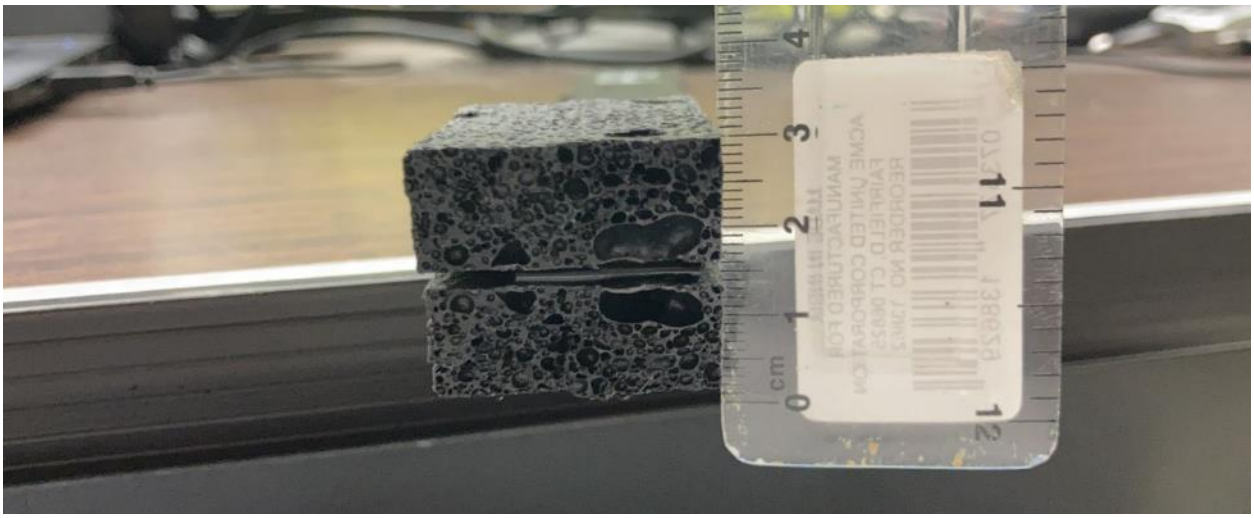

Figure 122. Detailed View of Damaged Area of Sample C4_1

Sample C5_1

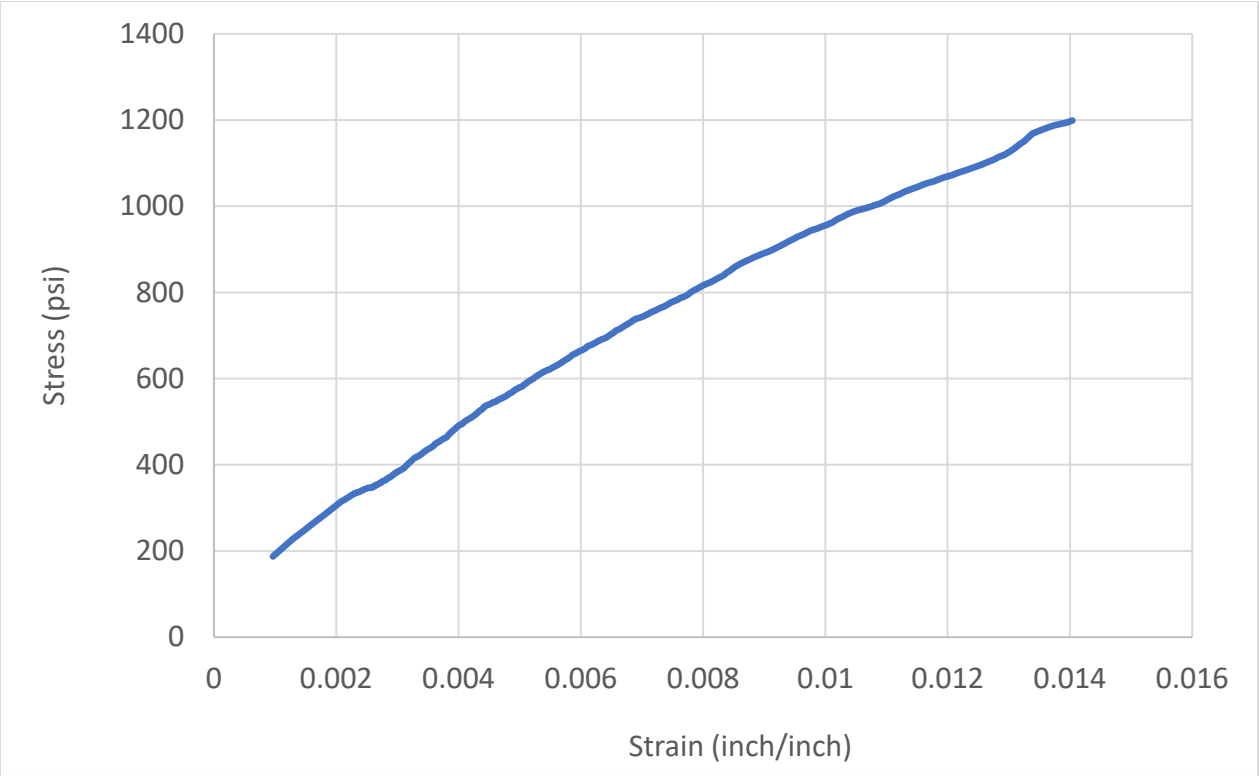

Figure 123. Stress-Strain Curve of Sample C5_1

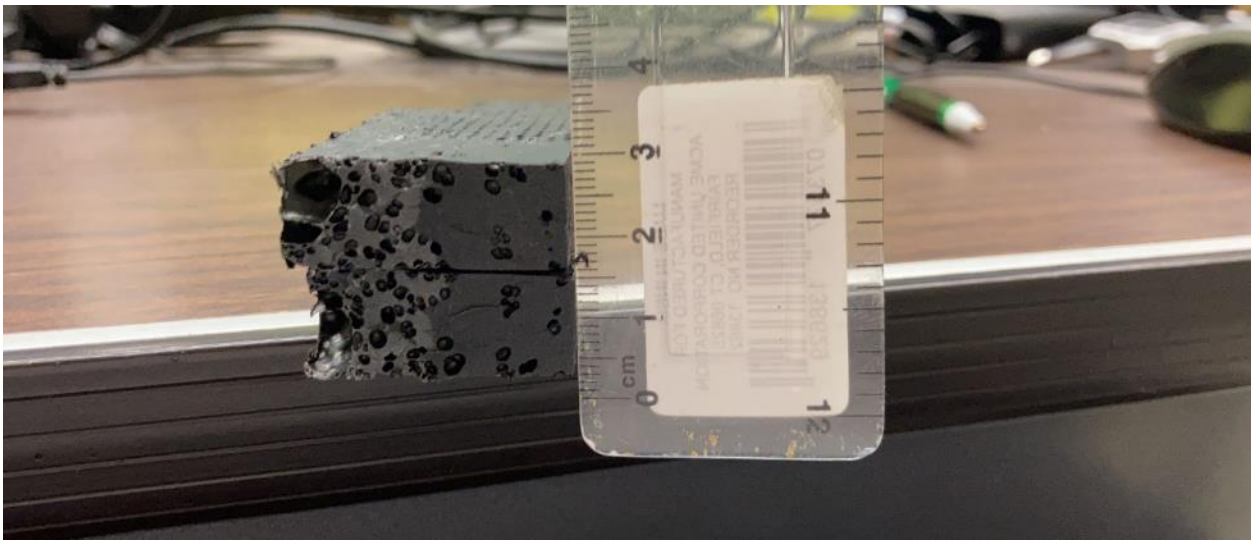

Figure 124. Detailed View of Damaged Area of Sample C5_1

Sample D4_1

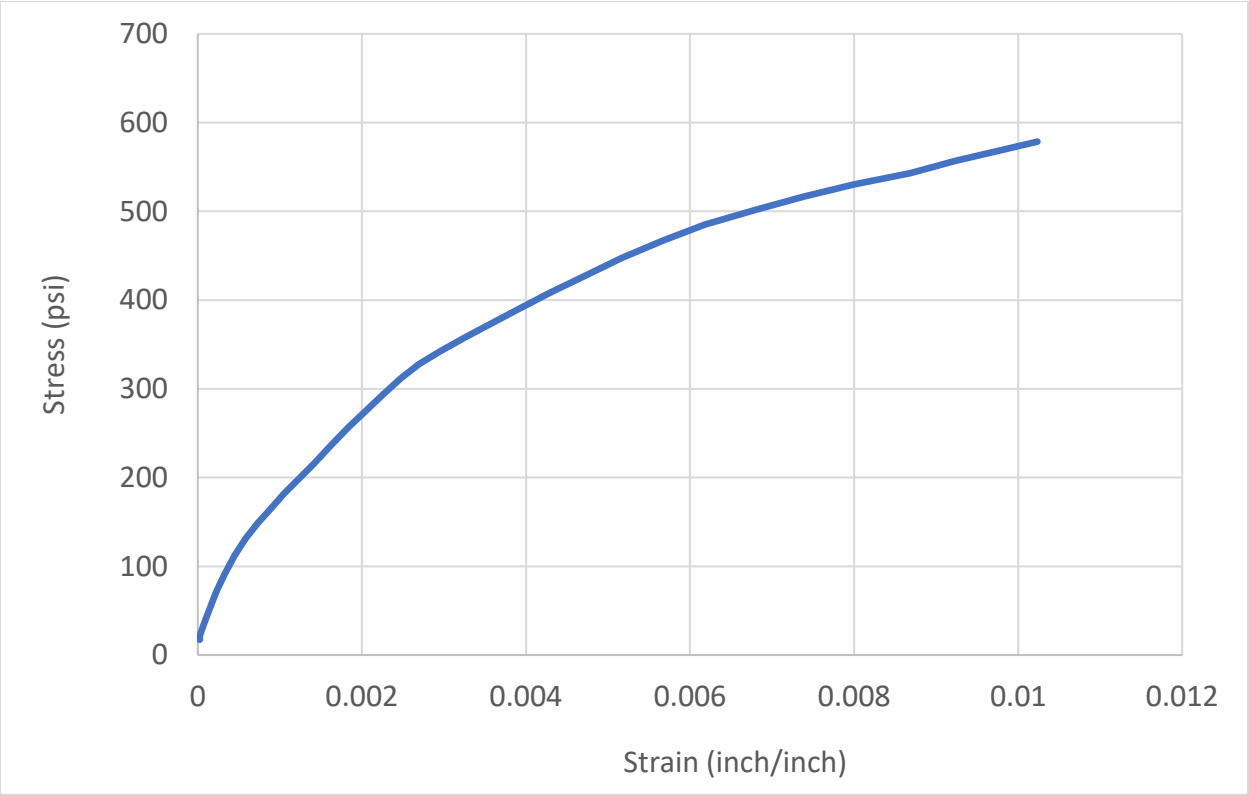

Figure 125. Stress-Strain Curve of Sample D4_1

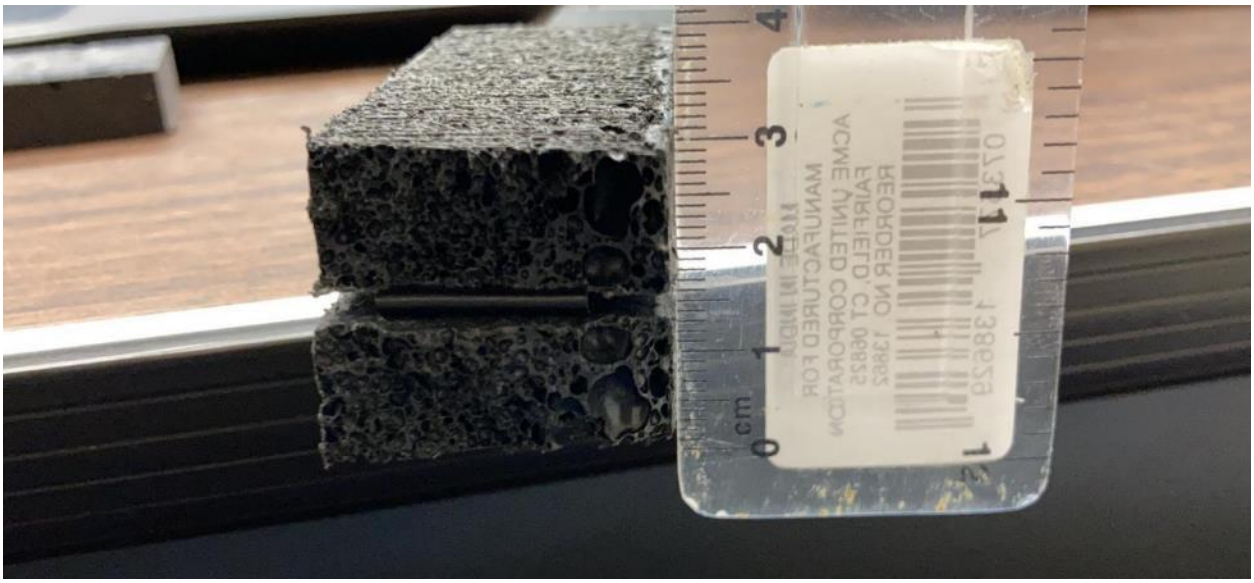

Figure 126. Detailed View of Damaged Area of Sample D4_1

Sample D5_1

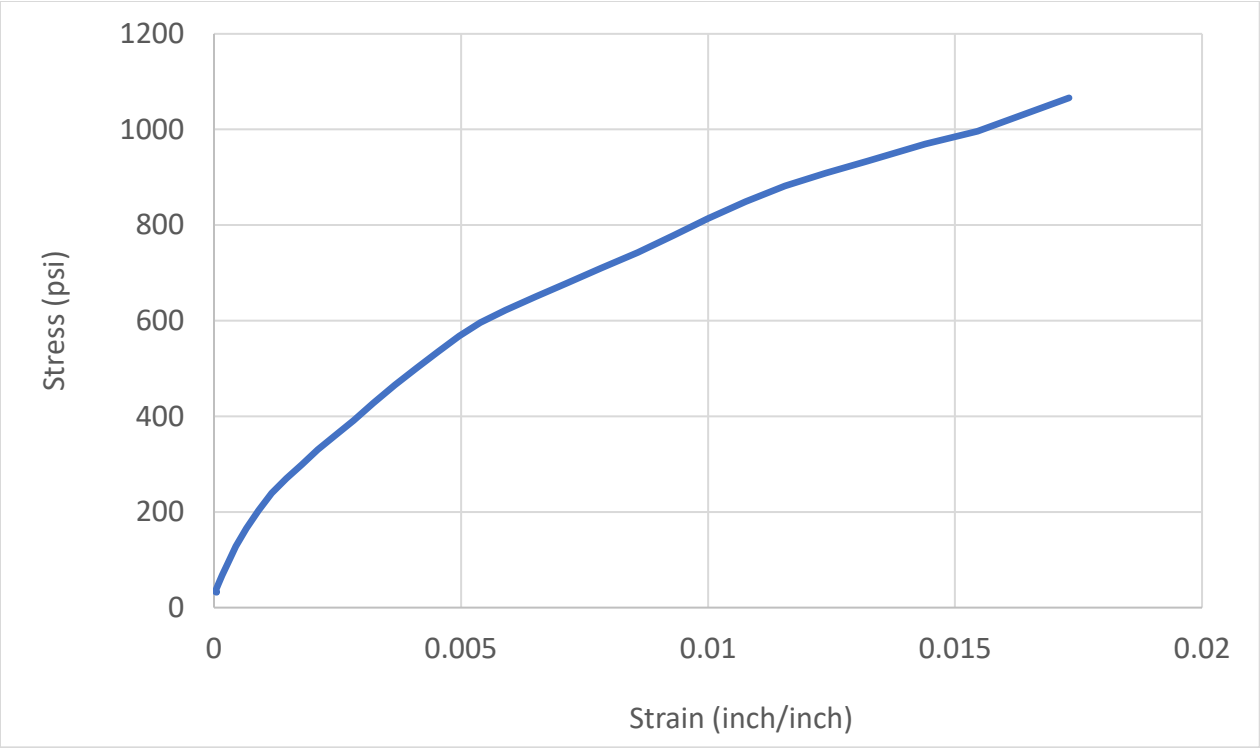

Figure 127. Stress-Strain Curve of Sample D5_1

Figure 128. Detailed View of Damaged Area of Sample D5_1

APPENDIX B

DISCUSSION OF INVALID TESTS

The following provides a close inspection of the tests considered invalid. Following testing, because of the randomness of both the size and distribution of void population, some test results were determined to be non-representative of the behavior of the material.

Deformations occurred in areas with voids due to the decrease in local cross-sectional area and local increase in stress values according to equation (10). For this reason, the ultimate strain values measured can be called as minimum.

$$\sigma_{local} = \frac{P}{A_{local}} \qquad (10)$$

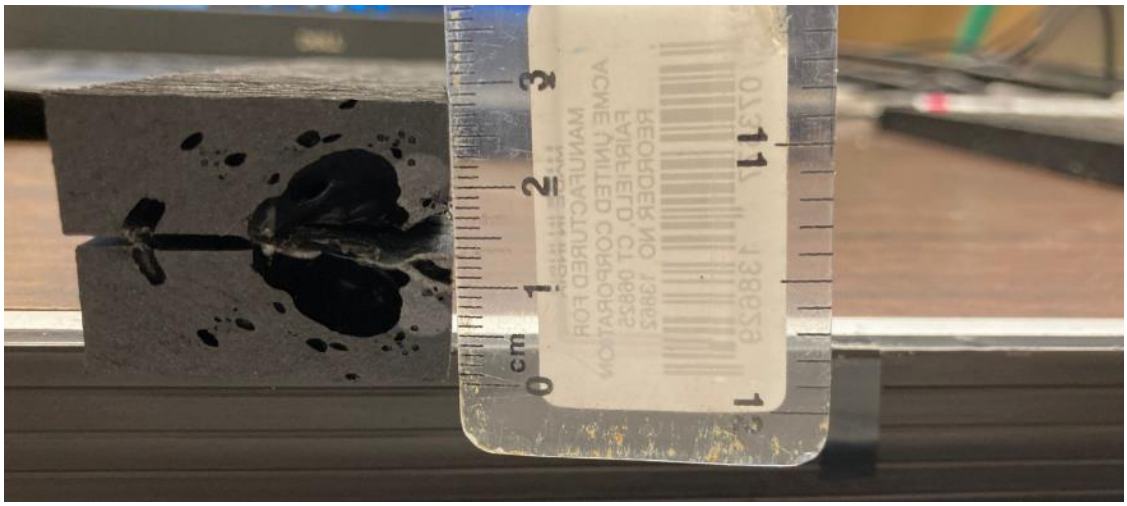

Figure 129. Deformation Occurring Around a Large Void

The fact that the deformation occurred away from the gauge length or around a large void caused the ultimate strain values to be different than expected in some samples. In cases where the large void was on the side where the extensometer is attached, high strain values were obtained due to the local bending in the sample. If the void was opposite the side to which the extensometer was attached, low strain values were obtained.

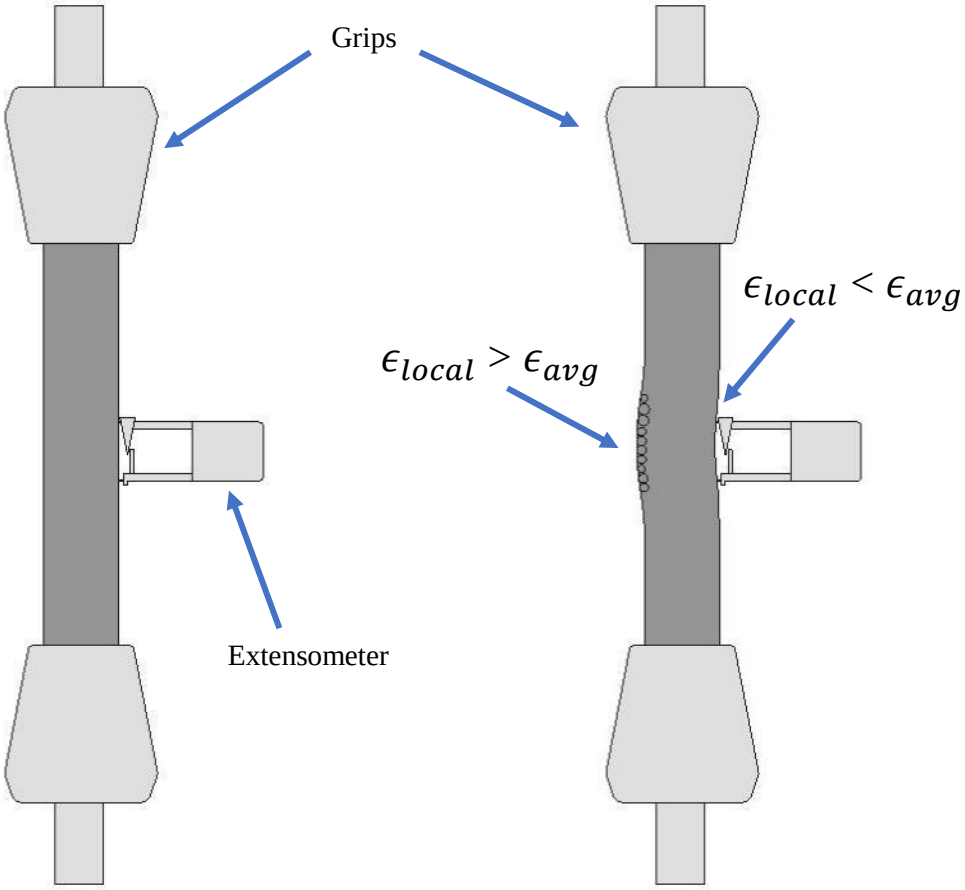

Figure 130. Bending Samples Because of the Large Voids

Samples in which the ultimate strain values are too high or low due to large voids are classified as "invalid tests". A total of 9 tests (Tests B2_1, B3_2, B4_2, B5_2, C4_2, C5_2, D1_2, D3_2 and D4_2) were defined as "invalid test" because the strain values were too high or low. In addition, the large void in the middle of the sample in test A3_2 caused both stress and strain values to be lower than expected and the sample was classified as an invalid test as seen in Figure 131.

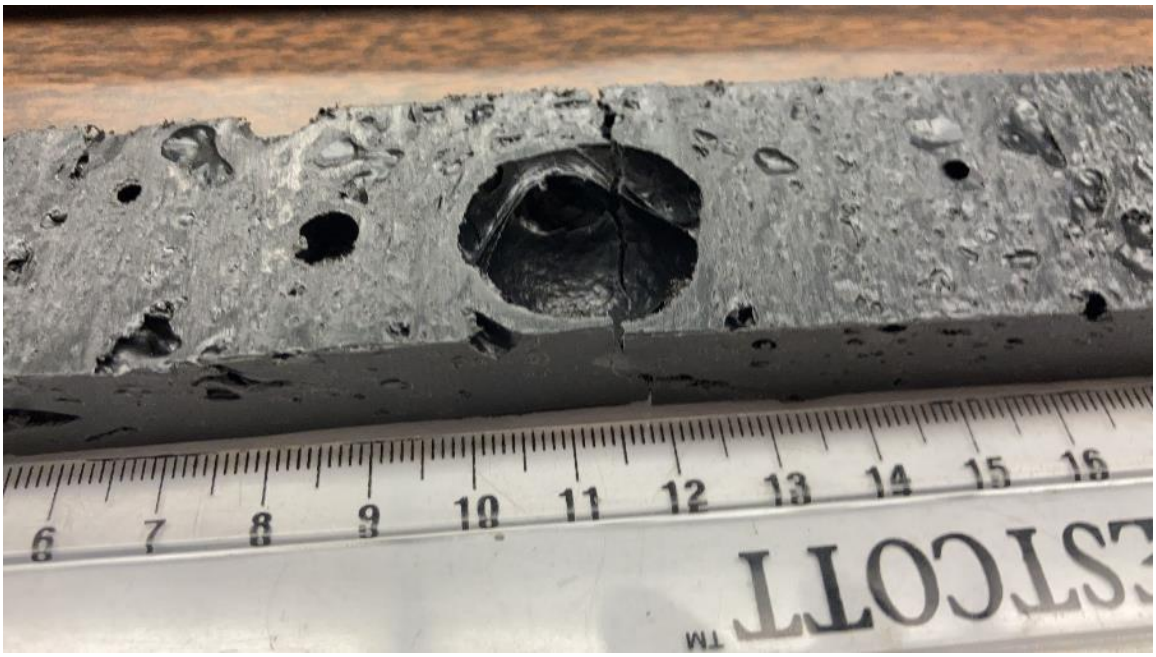

Figure 131. Large Void on Sample A3_2

Sample B2_1 has a large void with 13 mm diameter in the damage area. The measured ultimate strain value is low because the damage occurred away from the gauge length of the extensometer and the extensometer was located opposite the side where the damage occurred. (Figure 132)

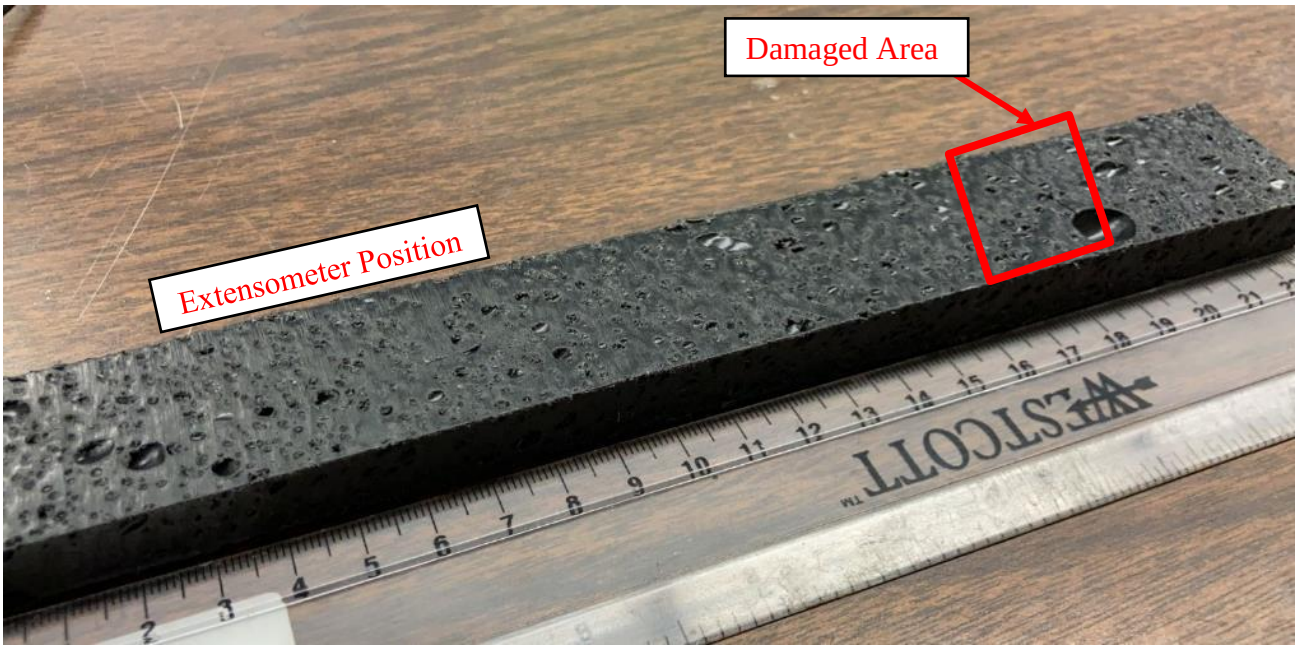

Figure 132. Detailed Photo of Sample B2_1

Sample B3_2 has a void of approximately 11 mm in diameter in the deformation zone as seen in Figure 133. Since the deformation occurs on the side where the extensometer is attached, the strain value is high than expected.

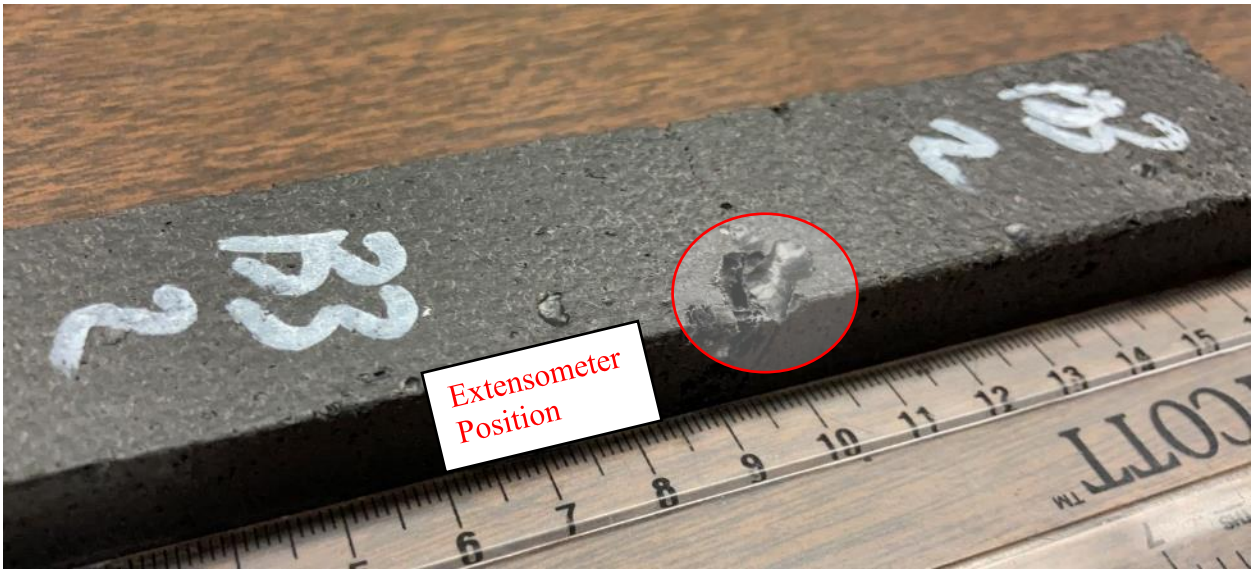

Figure 133. Detailed Photo of Sample B3_2

Sample B4_2 has a very large void (30 mm length and 12 mm width) in the damage area as seen in Figure 134. Also, since the extensometer was attached on the side where the damage occurs, the ultimate strain value seems high due to local bending.

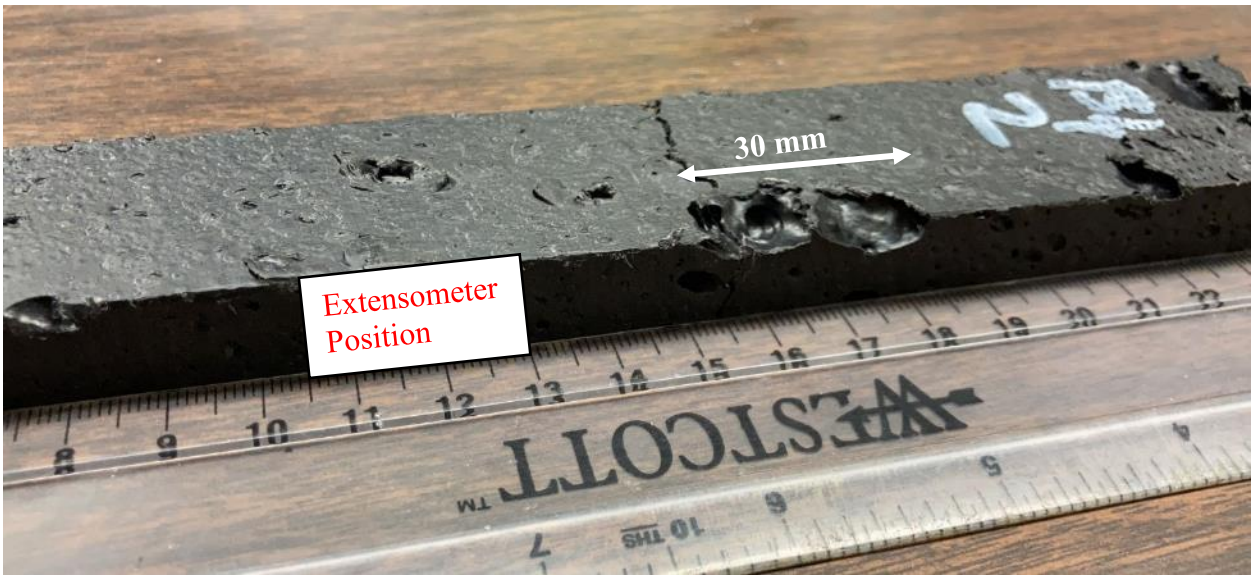

Figure 134. Detailed Photo of Sample B4_2

Sample B5_2 has a large void with approximately 13 mm diameter in the damage area as seen in Figure 135. Because the extensometer was attached against the side where the damage occurs, the ultimate strain value is low due to local bending.

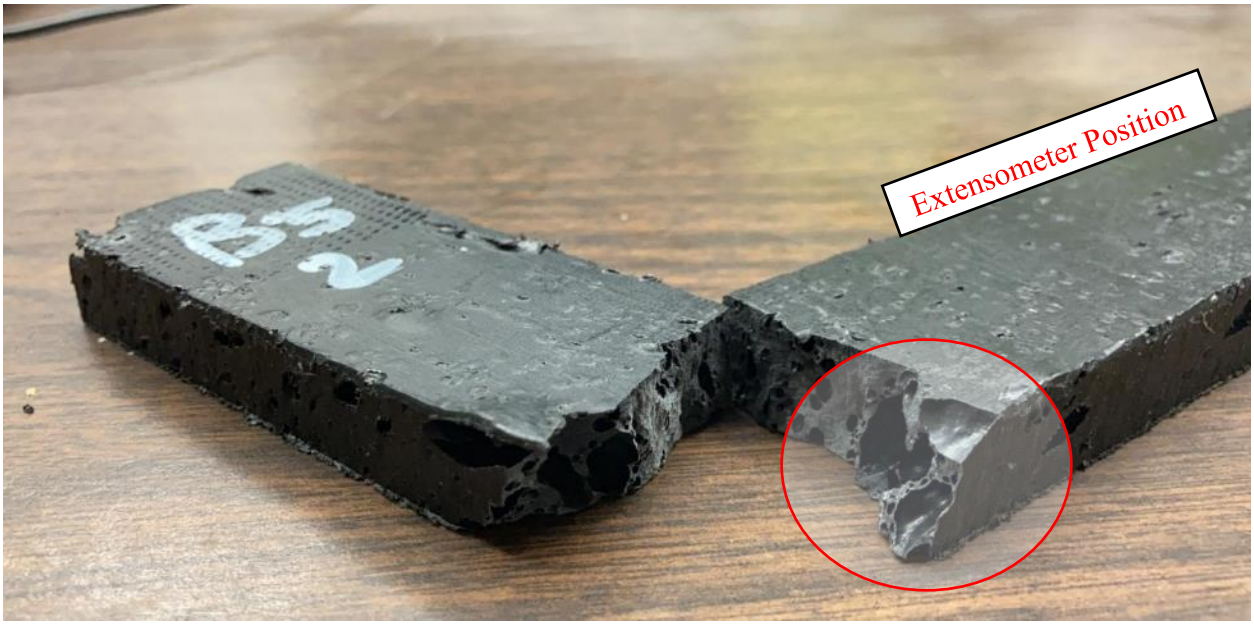

Figure 135. Detailed Photo of Sample B5_2

In Sample C4_2, the V_{VF} changes in the width direction of the sample. Since the extensometer was located to the side where the VVF is high, the measured ultimate strain was higher than expected. (Figure 136)

Figure 136. Detailed Photo of Sample C4_2

Sample C5_2 has a large void (19 mm length and 9 mm width) in the damage area as seen in Figure 137. Since the extensometer was positioned against the side where the damage occurs, the ultimate strain value was found low due to local bending.

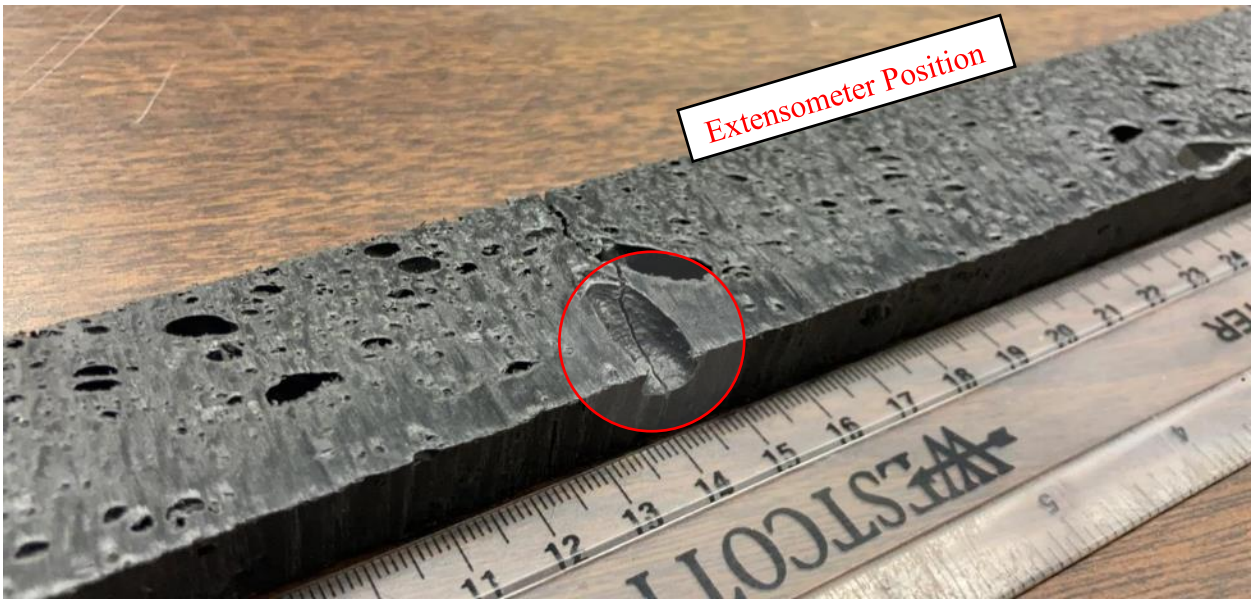

Figure 137. Detailed Photo of Sample C5_2

Sample D1_2 is a sample with changing V_{VF} as seen in the Figure 138. The right side of the sample has a more solid structure, while the left side has larger void content. Since the extensometer was attached on the bigger V_{VF} side, the ultimate strain value obtained is larger than expected.

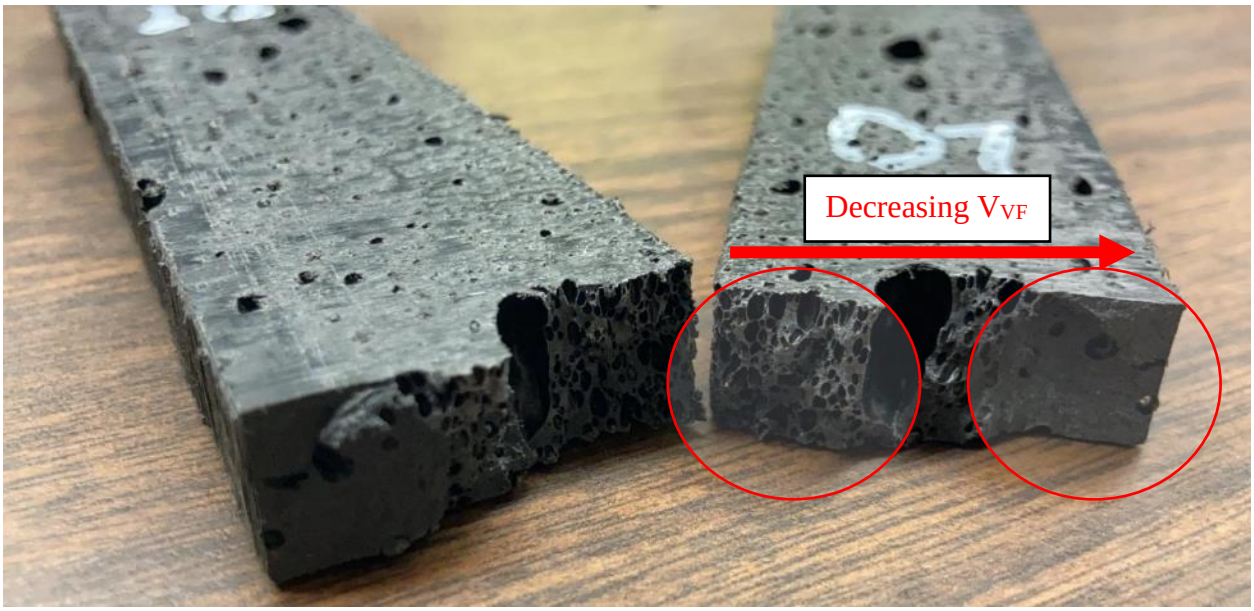

Figure 138. Detailed Photo of Sample D1_2

Sample D3_2 has varying void density in the damaged area. The ultimate strain value is high because the extensometer was located on the side where the void density is high. (Figure 139)

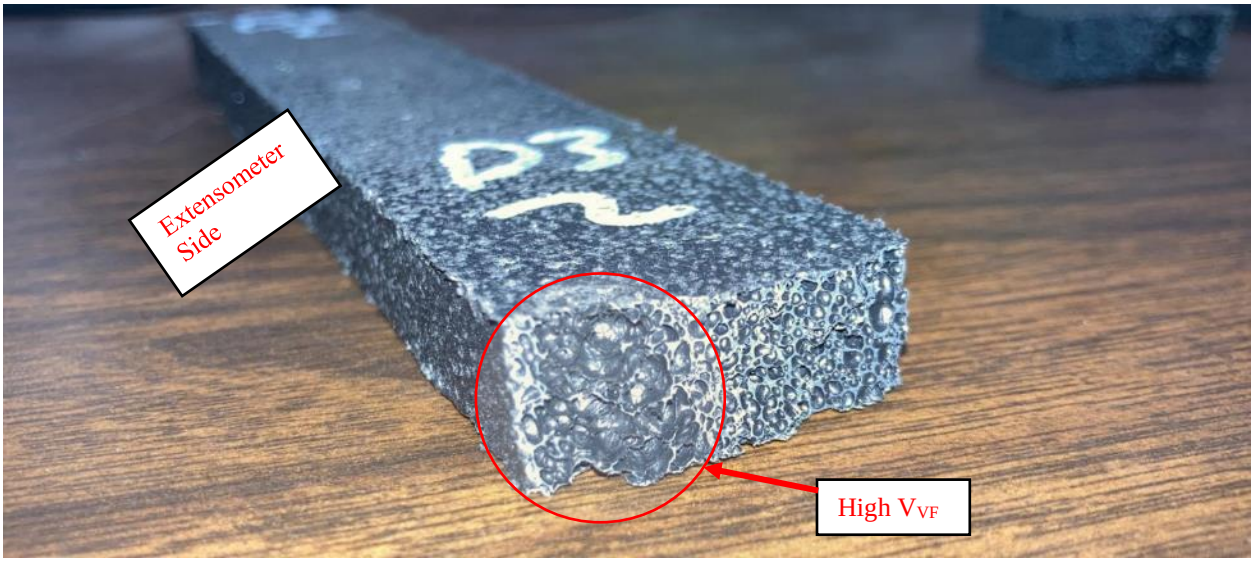

Figure 139. Detailed Photo of Sample D3_2

Sample D4_2 has four separate large voids in the damaged area with diameters of 7 mm, 6.5 mm, 6 mm, and 4 mm. In addition, voids in the cross-sectional area have high depth. The ultimate strain

value measured high due to local bending because the extensometer was attached on the side where the damage occurred. (Figure 140)

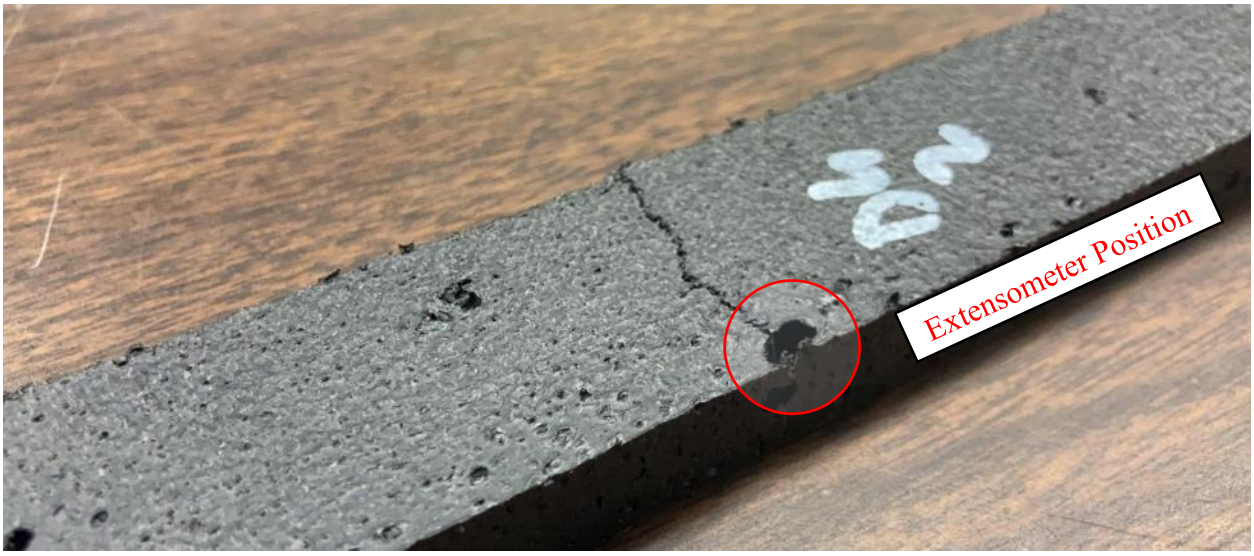

Figure 140. Detailed Photo of Sample D4_2